A blinded determination of H_0 from low-redshift Type Ia supernovae, calibrated by Cepheid variables

Bonnie R. Zhang,[1,2]★ Michael J. Childress,[3] Tamara M. Davis,[2,4] Natallia V. Karpenka,[3] Chris Lidman,[2,5] Brian P. Schmidt[1,2] and Mathew Smith[3]

[1]*Research School of Astronomy and Astrophysics, Australian National University, Canberra, ACT 2611, Australia*
[2]*ARC Centre of Excellence for All-sky Astrophysics (CAASTRO), University of Sydney, 2006, Australia*
[3]*School of Physics and Astronomy, University of Southampton, Southampton, SO17 1BJ, UK*
[4]*School of Mathematics and Physics, University of Queensland, QLD 4072, Australia*
[5]*Australian Astronomical Observatory, P.O. Box 915, North Ryde, NSW 1670, Australia*

ABSTRACT

Presently, a $>3\sigma$ tension exists between values of the Hubble constant H_0 derived from analysis of fluctuations in the cosmic microwave background by *Planck*, and local measurements of the expansion using calibrators of Type Ia supernovae (SNe Ia). We perform a blinded re-analysis of Riess et al. (2011) to measure H_0 from low-redshift SNe Ia, calibrated by Cepheid variables and geometric distances including to NGC 4258. This paper is a demonstration of techniques to be applied to the Riess et al. (2016) data. Our end-to-end analysis starts from available Harvard -Smithsonian Center for Astrophysics (CfA3) and Lick Observatory Supernova Search (LOSS) photometries, providing an independent validation of Riess et al. (2011). We obscure the value of H_0 throughout our analysis and the first stage of the referee process, because calibration of SNe Ia requires a series of often subtle choices, and the potential for results to be affected by human bias is significant. Our analysis departs from that of Riess et al. (2011) by incorporating the covariance matrix method adopted in Supernova Legacy Survey and Joint Lightcurve Analysis to quantify SN Ia systematics, and by including a simultaneous fit of all SN Ia and Cepheid data. We find $H_0 = 72.5 \pm 3.1(\text{stat}) \pm 0.77(\text{sys})$ km s^{-1} Mpc^{-1} with a three-galaxy (NGC 4258+LMC+MW) anchor. The relative uncertainties are 4.3 per cent statistical, 1.1 per cent systematic, and 4.4 per cent total, larger than in Riess et al. (2011) (3.3 per cent total) and the Efstathiou (2014) re-analysis (3.4 per cent total). Our error budget for H_0 is dominated by statistical errors due to the small size of the SN sample, whilst the systematic contribution is dominated by variation in the Cepheid fits, and for the SNe Ia, uncertainties in the host galaxy mass dependence and Malmquist bias.

Key words: supernovae: general – stars: variables: Cepheids – cosmological parameters – distance scale – cosmology: observations.

1 INTRODUCTION

The Hubble constant H_0 has proven difficult to measure since the discovery of the Universe's expansion almost a century ago (Hubble 1929), following the prediction of the latter in Friedmann's equations (Friedmann 1922). As given in the Hubble law $v = H_0 D$ (first derived by Lemaître 1927), H_0 sets the cosmic distance scale via the present expansion rate of the local Universe. The quest to make precise measurements of H_0 has been a continual challenge in observational cosmology, due to the difficulty of making accurate distance measurements.

Recently, discrepant values obtained from local and global measurements have propelled the Hubble constant back into the spotlight. Observations of cosmic microwave background (CMB) anisotropies with the *Planck* satellite found $H_0 = 67.3 \pm 1.2$ km s^{-1} Mpc^{-1} (Planck Collaboration XVI 2014), assuming a standard Λ cold dark matter (ΛCDM) cosmology. This value is $\sim 2.7\sigma$ lower than in Riess et al. (2011, hereafter R11), who measure $H_0 = 73.8 \pm 2.4$ km s^{-1} Mpc^{-1} from observations of Type Ia supernovae (SNe Ia) in the more local Universe. While the *Planck* measurement is dependent on an underlying cosmological model, the SN Ia-based measurement is model independent. The precision of these values highlights the importance of the tension between the two modes of measurements, which has increased to over 3σ significance in the updated analyses in Riess et al. (2016, hereafter R16, finding $H_0 = 73.0 \pm 1.8$ km s^{-1} Mpc^{-1}), and Planck Collaboration XIII (2016, finding $H_0 = 67.8 \pm 0.9$ km s^{-1} Mpc^{-1}).

Numerous re-analyses of the SN Ia-based measurement have followed, many of which have focused on the methods for the

★ E-mail: bonnie.zhang@anu.edu.au

rejection of Cepheid outliers. Efstathiou (2014, hereafter E14) questions and revises the outlier rejection algorithm in R11, concluding $H_0 = 72.5 \pm 2.5$ km s^{-1} Mpc^{-1} assuming a null metallicity dependence of the Leavitt law. Recently, Cardona, Kunz & Pettorino (2017) use Bayesian hyperparameters to downweight portions of the Cepheid data for both R11 and R16 data sets, finding $H_0 = 73.75 \pm 2.11$ km s^{-1} Mpc^{-1} for the R16 data. Moreover, the dependence of the intrinsic magnitude of SNe Ia on host galaxy properties has been explored in recent years (e.g. Sullivan et al. 2010). Rigault et al. (2013, 2015) find a relationship between peak brightness and star formation rate, and infer an overestimate of ~ 3 km s^{-1} Mpc^{-1} in the R11 value of H_0 arising from the fact that the calibration set of SNe Ia exist in galaxies which necessarily contain Cepheids, hence are likely to be late-type galaxies. However, Jones, Riess & Scolnic (2015) repeat the same analysis, with an increased sample size and the R11 selection criteria applied, and find no significant difference in the brightness of SNe Ia in star-forming and passive environments.

The CMB data in *Planck* has been re-analysed in Spergel, Flauger & Hložek (2015), who find a similar value to Planck Collaboration XVI (2014), of $H_0 = 68.0 \pm 1.1$ km s^{-1} Mpc^{-1}. Bennett et al. (2014) provide a CMB-based measurement which is independent of *Planck*, by combining data from *Wilkinson Microwave Anisotropy Probe 9*, the South Pole Telescope and Atacama Cosmology Telescope, and baryon acoustic oscillation (BAO) measurements from the Baryon Oscillation Spectroscopic Survey in the Sloan Digital Sky Survey III (SDSS-III), finding a value of $H_0 = 69.3 \pm 0.7$ km s^{-1} Mpc^{-1} (with a slight increase to $H_0 = 69.7 \pm 0.7$ km s^{-1} Mpc^{-1} if SN Ia data from R11 are included), which is slightly less discrepant with SN Ia-based values. Strong lensing provides an independent but model-dependent local measurement of H_0: the Suyu et al. (2017, H0LiCOW) program studies time delays between multiple images of quasars in strong gravitational lens systems, and find $H_0 = 71.9^{+2.4}_{-3.0}$ km s^{-1} Mpc^{-1} (Bonvin et al. 2017) in flat ΛCDM. It is noteworthy that the H0LiCOW analysis was performed blind to derived cosmological parameters (e.g. Bonvin et al. 2017, section 4.4); we discuss the importance of blinding in our analysis in Section 2.4.

One of the biggest open questions in cosmology today is whether the tension in H_0 signifies new physics – where inconsistencies between results from SNe and the CMB arise from the model-dependence of the measurement, and disappear when the correct model is used – or is the result of some systematic error in one or both measurements that has yet to be accounted for. Possible theoretical modifications to standard ΛCDM to reconcile the tension in H_0 include an increased neutrino effective number (the existence of dark radiation), and/or a more negative dark energy equation-of-state parameter w at late times. Di Valentino, Melchiorri & Silk (2016) explore these scenarios in a higher dimensional parameter space, with their findings supporting phantom dark energy with $w \sim -1.3$, while Wyman et al. (2014), Dvorkin et al. (2014), and Leistedt, Peiris & Verde (2014) focus on the implications of an additional massive sterile neutrino species. Meanwhile, Bernal, Verde & Riess (2016) examine the model dependence of the Universe's distance scale (anchored by H_0 and by the scale r_S of the sound horizon at radiation drag, at late and early times, respectively) by reconstructing its expansion history with minimal cosmological assumptions.[1] They conclude that the tension in H_0 translates to a mismatch in the normalizations provided by H_0 and r_s at two opposite ends of the distance ladder.

A genuine inconsistency in the value of the Hubble constant at low and high redshifts would have profound consequences. Therefore, it is imperative to fully understand uncertainties in the measured values of H_0, and to preclude possible human biases on the result. The most effective way of achieving the latter is to blind the value of H_0 throughout the analysis.

The use of data from R11 is for a proof of concept, necessary for our blind analysis technique, and to be followed shortly with the same analysis applied to R16 data. Numerous improvements over R11 have been made in R16, in the analysis as well as the size and quality of data. Changes to the outlier rejection and the Cepheid metallicity calculations have addressed some of the concerns raised in E14. However, our analysis involves both a simultaneous fit to all data sets, and the accepted methodology of recent SN cosmology analyses (Conley et al. 2011; Betoule et al. 2014) for considering SN Ia systematics. Both of these points carry significant differences from the R11 and R16 analysis chains, and have yet to be included in a re-analysis. Nor have the SN data been revisited in its entirety, starting from the available photometry. Thus, we are motivated by the desire to provide such a validation of the SN data, and by the current relevance and importance of the Hubble constant, to produce in this work an independent, blinded, end-to-end re-analysis of the R11 data to determine H_0 and its uncertainty.

In summary, we combine the framework for calibrating an SN Ia Hubble diagram with Cepheid variables, with the best estimates of SN systematics via covariance matrices. We determine H_0 using the magnitude–redshift relation (i.e. a Hubble diagram) of low-redshift SNe Ia, with their zero-point set by Cepheid variables in host galaxies of eight nearby SNe Ia, which are in turn calibrated by very long baseline interferometry (VLBI) observations of megamasers in NGC 4258, and other geometric distances to the Large Magellanic Cloud (LMC) and Cepheids in our Galaxy.

This paper is structured as follows. First, we present an overview of our methods in Section 2, followed by the distinct sets of data with the equations relating them in Section 3. In Section 4, we focus on the Cepheid variables and perform a fit to the Cepheid data only, comparable to the E14 re-analysis of R11. Next in Section 5, we discuss SNe Ia, including details of fitting SNe Ia on a Hubble diagram and results of a preliminary SN-only fit. This fit relies on computations of individual SN systematic terms in the form of covariance matrices, which are examined in depth in Appendix C. Finally, Section 6 ties together the Cepheid and SN Ia information into a combined and simultaneous fit of all data; we conclude with a discussion of these results in Section 7.

2 METHODS

In this section, we paint a broad picture of our approach to measuring H_0, postponing specific details of and equations relating to the data to Section 3. We begin with the theory and mathematics of finding H_0 in the cosmology analysis, followed by the astronomy that enables this: distance measurements with SNe Ia and Cepheid variables as standard candles. Equally important are the Bayesian statistics that underpin the analysis, and the method for blinding the result.

2.1 Theory of extracting H_0

In its traditional formulation, Hubble's law states that the recession velocity of objects is proportional to their distance:

$$v(z) = H_0 D(z) \tag{1}$$

---

[1] This is possible as the combination of SNe Ia and BAO as probes constrains the product $r_S H_0$ in a model-independent way.

where the constant of proportionality H_0 represents the present expansion rate of the Universe, scaled by its size (i.e. $H_0 = \frac{\dot{a}}{a}$, where a is the scalefactor and overdot indicates differentiation with respect to time, t). Methods of determining H_0 typically involve taking the ratio of the two sides of equation (1). We expand on the subtleties of this below.

The distance in Hubble's law is related to the luminosity distance by

$$D(z) = \frac{1}{1+z} D_{\rm L}(z), \tag{2}$$

assuming a flat universe.[2]

The luminosity distance $D_{\rm L}(z)$ can be determined observationally (i.e. with no knowledge of cosmological parameters) using standard candles. These have known absolute magnitudes M, so taking the difference between M and the apparent magnitude m gives the distance modulus $\mu \equiv m - M$ and hence the luminosity distance $D_{\rm L} \equiv 10^{\frac{\mu-25}{5}}$ Mpc. In practice, the process of measuring distances is far from straightforward, and is outlined in Section 2.2.

On the left-hand side, $v(z)$ is the predicted velocity due to expansion for a galaxy at redshift z.[3] The exact expression for $v(z)$ is given by integrating the Universe's expansion up to redshift z:

$$v(z) = c \int_0^z \frac{{\rm d}z'}{E(z')}, \tag{3}$$

where $E(z) \equiv H(z)/H_0$ is a function of cosmological parameters, as defined in Peebles (1993),[4] and $v(z)$ is independent of H_0.[5]

---

[2] To include curvature, note that the present distance to an object at redshift z is given by $D(z) = R_0 \chi$, with χ being the comoving coordinate and R_0 the scalefactor at the present day with dimensions of distance (in the equation for H_0 above $a(t) \equiv R(t)/R_0$). Then, luminosity distance is defined as

$$D_{\rm L}(z) \equiv (1+z)R_0 S_k(\chi), \tag{4}$$

with $R_0 \equiv c/(H_0\sqrt{|\Omega_k|})$ and

$$S_k(x) = \begin{cases} \sin x & k = 1, \\ x & k = 0, \\ \sinh x & k = -1, \end{cases} \tag{5}$$

so $D(z) = \frac{1}{1+z} \frac{\chi}{S_k(\chi)} D_{\rm L}(z)$.

[3] For simplicity, we do not distinguish here between redshifts in different reference frames, and only use one redshift z. We distinguish between different redshifts, particularly in equation (2), in Appendix B4.

[4] In Friedmann–Lemaître–Robertson–Walker cosmologies, $E(z)$ is given by (e.g. Carroll, Press & Turner 1992)

$$E(z) = \sqrt{\Omega_{\rm M}(1+z)^3 + \Omega_k(1+z)^2 + \Omega_\Lambda} \tag{6}$$

where $\Omega_{\rm M}$ and Ω_Λ are, respectively, the densities of normal matter and the cosmological constant (relative to the critical density), k is the curvature, and $\Omega_k \equiv 1 - \Omega_{\rm M} - \Omega_\Lambda$ (zero in a flat universe). If dark energy is something other than a cosmological constant, with a generic equation of state w, replace Ω_Λ with $\Omega_{\rm de}(1+z)^{3(1+w)}$.

[5] It is interesting to note that $v(z)$ is independent of H_0; it depends only on redshift and cosmological parameters such as $\Omega_{\rm M}$ and Ω_Λ. That may seem unintuitive, but it is velocity as a function of distance $v(D)$ that is function of H_0 (things that are moving faster have gone further). Velocity as a function of redshift $v(z)$ works differently since redshift is not proportional to distance. A galaxy's redshift is determined by how much the Universe has expanded since the light was emitted. That depends on the travel time, which does depend on the densities that cause the Universe to accelerate or decelerate (and thus for the light to take longer or shorter times to reach us), but not on H_0.

At low redshifts, the cosmological dependence of $v(z)$ is very weak and it is a good approximation to use a second-order Taylor expansion in terms of the deceleration and jerk parameters q_0 and j_0.[6] Thus, we follow R11 and use,

$$v(z) = \frac{cz}{1+z} \left[1 + \frac{1}{2}(1 - q_0)z - \frac{1}{6}\left(1 - q_0 - 3q_0^2 + j_0\right)z^2 \right]. \tag{7}$$

At low-redshift equations (3) and (7), both reduce to the familiar $v(z) \approx cz$. At moderate redshifts ($z < 0.1$), equation (7) closely approximates most observationally reasonable cosmological models. We explored the uncertainty associated with assuming equation (7) and the cosmology stated in (see footnote 6), finding the impact to be small: varying either $\Omega_{\rm M}$ or w by 0.1 changes H_0 by $0.015 \, {\rm km \, s^{-1} \, Mpc^{-1}}$ or $0.1 \, {\rm km \, s^{-1} \, Mpc^{-1}}$, respectively, in the sense that an increase in $\Omega_{\rm M}$ or w causes an increase in H_0. The maximal difference in $\mathcal{M}$ induced by varying q_0, j_0 within values allowed by 1σ contours in Betoule et al. (2014) is an order of magnitude smaller than its statistical uncertainty.

Rearranging equations (1), (2), and (7) gives us the equation for H_0 as a function of observables, z and $D_{\rm L}$,[7]

$$\begin{aligned} H_0 &= \frac{v(z)(1+z)}{D_{\rm L}(z)} \\ &= \frac{cz}{D_{\rm L}(z)} \left[1 + \frac{1}{2}(1 - q_0)z - \frac{1}{6}(1 - q_0 - 3q_0^2 + j_0)z^2 \right]. \end{aligned} \tag{8}$$

Thus, determining H_0 amounts to comparing the velocity in equation (7) – derived from the measured redshift – to the observed luminosity distance, measured with standard candles. The equations encapsulating this process are detailed in Section 3.

2.2 Measuring distance

Astronomical distances can be measured using standard candles: standardizable objects with known absolute magnitude which, combined with an apparent magnitude, give the distance modulus. These distances are often relative rather than absolute. Since each mode of measurement is useful only over a limited range of distances, multiple standard candles are tied together to form a so-called distance ladder. At the bottom of the ladder are absolute distances determined from geometric methods (i.e. trigonometric parallax), only accurate at relatively small distances. Then, nearby standard candles (i.e. Cepheid variables) give distances relative to this geometric scale; similarly, each rung of the ladder is calibrated on the previous.

Standard candles (a distance scale) provide one approach to measuring cosmological parameters including H_0. Alternatively, standard rods (a length-scale) in the form of BAO (e.g. Eisenstein et al. 2005) provide complementary (and for some parameters, orthogonal) constraints, most recently in Planck Collaboration XIII (2016). Weinberg et al. (2013) provide a review of cosmological probes; we refer the interested reader to its section 4 for a review of BAO.

In our determination of H_0, we rely on two standard candles: SNe Ia and Cepheid variables. These together prescribe a relative

---

[6] We assume a standard ΛCDM cosmology with $\Omega_M \sim 0.3$, $\Omega_\Lambda \sim 0.7$, fixing $q_0 = -0.55$ and $j_0 = 1$.

[7] For non-zero curvature, equation (8) becomes

$$H_0 = \frac{v(z)(1+z)}{D_{\rm L}(z)} \frac{S_k(\chi)}{\chi}. \tag{9}$$

distance scale for the low-*z* SNe Ia. The absolute calibration is given by the geometric maser distance of NGC 4258 from Humphreys et al. (2013). The Cepheid variables lie in this galaxy and eight other galaxies containing nearby SNe Ia, calibrating the SNe. The absolute distances and measured redshifts of the low-*z* SNe are combined to determine H_0 as described in Section 2.1, through equations detailed in Section 3. Next we briefly describe each standard candle.

Cepheid variables are pulsating supergiants with periods of days to hundreds of days, well characterized by their luminosity via the empirical Leavitt law (Leavitt 1908; Leavitt & Pickering 1912) – also commonly known as the period–luminosity relation. The brightness and regular pulsation of Cepheid variables as well as their ease of discovery and classification make Cepheids reliable distance indicators in the nearby Universe, and the basis of the cosmic distance ladder (Freedman & Madore 2010). Some difficulties and systematics include crowding and confusion (which necessitate outlier rejection), metallicity, and extinction; these are discussed further in Section 4.2.

SNe Ia are thought to be thermonuclear explosions of accreting white dwarfs, with two qualities which recommend them as excellent distance indicators up to high redshift: they are intrinsically very bright, and highly standardizable in terms of their apparent peak brightness, light-curve shape, and colour (Phillips 1993; Hamuy et al. 1996; Riess, Press & Kirshner 1996) – see Section 3.2.2 for more details. Indeed SNe Ia have played a pivotal role in recent observational cosmology, particularly in the discovery of the accelerating Universe (Riess et al. 1998; Schmidt et al. 1998; Perlmutter et al. 1999). In the past decade, SN Ia samples have greatly expanded, reducing statistical uncertainty. However, observations of SN Ia are still subject to numerous systematics, which can be significant and correlated between SNe. These systematics include: calibration uncertainties, dust, and corrections for peculiar velocities, and host galaxy mass, and will be discussed in Appendix C.

2.3 Bayesian statistical methods

We estimate the fit parameters Θ (given in Section 3) in a Bayesian framework, relying on the principle of sampling the likelihood $\mathcal{L}(\Theta)$ over the parameter space to determine the posterior distribution function (PDF). The generalized likelihood is determined from the χ^2 statistic, a function of Θ:

$$\mathcal{L}(\Theta) = \exp\left(-\frac{\chi^2(\Theta)}{2}\right) \quad (10)$$

$$\chi^2(\Theta) = (\hat{\boldsymbol{m}} - \boldsymbol{m}_{\mathbf{mod}})\mathbf{C}^{-1}(\hat{\boldsymbol{m}} - \boldsymbol{m}_{\mathbf{mod}})^{\mathbf{T}}. \quad (11)$$

Here, $\hat{\boldsymbol{m}}$ and $\boldsymbol{m}_{\mathbf{mod}}$ are the observed and theoretical magnitude vectors (over all data) respectively,[8] and $\mathbf{C}$ is the covariance matrix of uncertainties in $\hat{\boldsymbol{m}}$. The model $\boldsymbol{m}_{\mathbf{mod}}$ is implicitly a function of Θ. In each fit outlined in Section 3.4, an expression for χ^2 will be given explicitly, i.e. equations (20), (22), and (23). When uncertainties are uncorrelated (i.e. $\mathbf{C}$ is diagonal) equation (11) reduces to the more familiar

$$\chi^2(\Theta) = \sum_i \frac{(\hat{m}_i - m_{\mathrm{mod}i})^2}{\sigma_i^2}. \quad (12)$$

2.3.1 PDF estimation

In higher dimensional parameter spaces, the computational expense of calculating and integrating the likelihood necessitates Monte Carlo techniques to statistically sample the parameter space, the most common being Markov Chain Monte Carlo (MCMC). These techniques are useful for parameter estimation or model selection (see e.g. Davis & Parkinson 2016). Nested sampling (Skilling 2004) is another such technique, in which the likelihood is evaluated at sample 'live' points drawn from an iteratively replaced distribution until convergence, where the posterior is recovered. The MultiNest algorithm (Feroz & Hobson 2008; Feroz, Hobson & Bridges 2009; Feroz et al. 2013) is a robust nested sampling tool for retrieving posterior samples from distributions which may have multiple peaks or 'modes'. We use the implementation PYMULTINEST described in Buchner et al. (2014) for most fits (details in Section 3.4). For some lower dimensional fits (Section 5.4), we use emcee (Foreman-Mackey et al. 2013), a PYTHON implementation of MCMC.

Each algorithm takes as inputs the data, a prior distribution within the parameter space (which live points are drawn from), and the likelihood as a function of the data and parameters. In addition, we select the sampling efficiency for parameter estimation and the number of live points (walkers). MultiNest outputs include the best-fitting (maximal likelihood) parameters and the marginalized posterior distribution for each parameter. In our fits, the marginalized PDFs appear symmetrical and Gaussian (e.g. Figs 3 and 4), so we take our best estimates of values and uncertainties of each parameter from the mean and standard deviation of the marginalized PDF.

2.4 Blind analysis

To perform a blind analysis is to obscure the principal aspects of the result until the analysis is complete. The overarching motivation for blinding is to eliminate the impact of human biases on the result, including confirmation bias. Pre-conceptions about the 'correct' value for a result are irrelevant to the validity of the analysis and can only reduce the value of the findings. Conversely, a blind analysis has all the more bearing for having reached its conclusion blind. Croft & Dailey (2011) find evidence of confirmation bias in recent measurements of cosmological parameters and recommend blinding; similarly Maccoun & Perlmutter (2015) argue for its necessity. In recent years, the practice of blind analysis has become standard in particle physics, and is increasingly adopted in cosmology.

Our priority is to hide the value of H_0 so as to not influence its result, so we blind the parameter $\mathcal{H}$ which contains equivalent information.[9] We also blind the SN Ia magnitude zero-point M_B which has the most interaction with $\mathcal{H}$, and is the best constrained in the literature, relative to other parameters in Θ. We implement these blinds in the analysis and data, respectively. For any likelihood function containing $\mathcal{H}$ (i.e. involving the low-*z* SNe), we make the shift $\mathcal{H} \mapsto \mathcal{H} + \mathfrak{o}_H$ for an offset $\mathfrak{o}_H$. Meanwhile, we effectively shift M_B by adding another offset $\mathfrak{o}_M$ to all SN magnitudes m_B. Both offsets $\mathfrak{o}_H$ and $\mathfrak{o}_M$ are unknown real numbers, randomly drawn from normal distributions and never printed. These are seeded by distinct known numbers to ensure that the offsets are constant and can be retrieved. Our method allows the recovery of the true unblinded values by simply subtracting the offsets once the blind is lifted.

---

[8] We retain this convention where it is necessary to explicitly distinguish the data from the model.

[9] We fit for the parameter $\mathcal{H} := 5\log_{10} H_0 - 25$, which is linear in magnitude (equation 19), instead of H_0.

Table 1. Recent nearby SNe Ia and their host galaxies used in R11, along with observations of Cepheids in these galaxies.

Galaxy	SN Ia	N_{Cepheids}
NGC 4536	SN 1981B	69
NGC 4639	SN 1990N	32
NGC 3370	SN 1994ae	79
NGC 3982	SN 1998aq	29
NGC 3021	SN 1995al	26
NGC 1309	SN 2002fk	36
NGC 5584	SN 2007af	95
NGC 4038	SN 2007sr	39
NGC 4258	–	165
Total		570

We choose to not blind the other parameters which appear in the preliminary Cepheid- or SN-only fits, primarily because these parameters do not have strong enough priors from the literature to introduce human bias. Moreover, the variation we observe in the preliminary values of the nuisance parameters $\{b_W, Z_W, \alpha, \beta\}$ is useful for informing which preliminary fits to carry forward to the global fits. Knowing the preliminary nuisance parameters will not bias our results because 'best' versions of the preliminary fits are not chosen; instead we select a representative sample of these fits and use the scatter to quantify the systematic uncertainties.

3 DATA AND ANALYSIS TECHNIQUES

This section describes our Cepheid and SN Ia data, using equations for the apparent magnitude of each data set to demonstrate the relationships between them. These are followed by an outline of the steps of the fit.

3.1 Data samples

Our analysis uses three sets of data:

(i) *Cepheid variables:* 570 spread between nine nearby galaxies (see Table 1), namely:

(a) 165 in the distance anchor NGC 4258, and
(b) 405 in eight galaxies that host recent nearby SNe Ia.

(ii) *Anchor ('nearby') SNe:* eight recent SNe Ia in the nearby galaxies (also in Table 1).

(iii) *Low-z SNe Ia:* 280 low-redshift ($z < 0.06$) SNe Ia from the Harvard-Smithsonian Center for Astrophysics (CfA3; Hicken et al. 2009a) and Lick Observatory Supernova Search (LOSS; Ganeshalingam et al. 2010) samples.

Together these three data sets allow us to calibrate our distance ladder. The galaxy NGC 4258 hosts the water masers that give us a precise absolute local distant measurement (Humphreys et al. 2013), and allows us to calibrate the Cepheids. As in R11, we also use the LMC and Milky Way (MW) as distance anchors in combination with NGC 4258, relying on independent distances measured from detached eclipsing binaries (Pietrzyński et al. 2013) to Cepheids in the LMC, and *Hipparcos* and *Hubble Space Telescope* (*HST*) parallax measurements of Cepheids in our Galaxy (van Leeuwen et al. 2007). The Cepheids in turn enable us to calibrate the absolute magnitudes of the eight SNe that occurred in nearby galaxies with quality Cepheid measurements. These then allow us to calibrate the whole SN sample, which ultimately gives most of the constraining power for our H_0 measurement. In practice, we perform a global fit

to all of these samples together. In the next section, we outline the equations needed to relate all of these standard candles and extract a measurement of H_0 following the theory in Section 2.1.

Since the purpose of this paper is to provide an independent analysis of the data in R11, we adopt an identical sample in order to make a faithful comparison. Our aim is to use the same framework to analyse newer data sets including SNe Ia in the CfA4 survey (Hicken et al. 2012) and Cepheids in R16 at a later stage.

3.2 Equations for apparent magnitude

3.2.1 Cepheids

Our first data set, the Cepheid variables, allow us to infer distances to the nearby galaxies via the Leavitt law (also commonly known as the period–luminosity relation):

$$m_W = b_W(\log_{10} P - 1) + Z_W \Delta \log_{10}[\text{O/H}]_{ij} + M_W + \mu. \quad (13)$$

Equation (13) relates the apparent 'extinction-free' (Wesenheit) magnitude m_W,[10] period (P; in days), and metallicity of a Cepheid at distance modulus μ. The slopes b_W and Z_W represent the dependence of the magnitude on period and metallicity; the zero-point M_W physically represents the Wesenheit magnitude of a Cepheid in our Galaxy (at a distance of 10 pc), with a period of 10 d. We use relative values of the metallicity ($\Delta \log_{10}[\text{O/H}]_{ij} := \log_{10}[\text{O/H}] - 8.9$) and period to pivot the fit near the data.

3.2.2 Type Ia supernovae

SNe Ia comprise our remaining data. A spectroscopically normal SN Ia has a light curve parametrized by its brightness (hence distance), observed colour and decline rate. These measures are represented by different quantities in various SN Ia frameworks; in SALT2 (Spectral Adaptive Lightcurve Template; Guy et al. 2007), these are the apparent magnitude m_B at time of B-band maximum, 'stretch' X_1 and colour C (roughly corresponding to $B - V$ at maximum), related by:

$$m_B = M_B - \alpha X_1 + \beta C + \mu \quad (14)$$

where M_B is the canonical SN Ia absolute magnitude, and α and β are SALT2 nuisance parameters for the stretch and colour dependences.

SNe Ia in more massive galaxies are brighter after these standard corrections for colour and stretch, as discussed in Appendix B3. To account for this, we replace M_B in equation (14) with the corrected absolute magnitude M_B^*, which can take two discrete values depending on the host galaxy mass: M_B or $M_B + \Delta M_B$. We will fix ΔM_B (see Appendix B3) and fit for the three global parameters $\{\alpha, \beta, M_B\}$.

Our second data set contains the eight 'nearby' SNe Ia in Table 1, with apparent magnitudes given by equation (14) (with M_B^* instead of M_B). The SN Ia and Cepheid in the same galaxy have common distance modulus μ in equations (14) and (13); thus, the Cepheids calibrate the nearby SNe, which in turn determine the SN Ia magnitude zero-point M_B.

The much larger sample of 280 SNe Ia makes up our third data set. These 'low-z' SNe originate from CfA3 and LOSS, with details to follow in Section 5.1. Once we have calibrated their

---

[10] We use the quantity $M_W \equiv V - R_V(V - I)$ constructed in Madore (1982) from the Wesenheit function (van den Bergh 1975), from V- and I-band absolute magnitudes. Assuming constant ratio R_V of total to selective absorption, M_W is independent of extinction. We fix $R_V = A_V/E(V - I) = 3.1$ as in R11.

absolute magnitudes using the eight 'nearby' SNe, we can use the theory derived in Section 2.1 to relate their measured magnitudes to the value of H_0. Assuming equation (8) and writing $f(z) \equiv 1 + \frac{(1-q_0)z}{2} - \frac{(1-q_0-3q_0^2+j_0)z^2}{6}$, we have in place of equation (14)

$$m_{\mathrm{B}} = M_{\mathrm{B}}^* - \alpha X_1 + \beta C + 5 \log_{10} \left(\frac{czf(z)}{H_0} \right) + 25. \tag{15}$$

3.3 Global fit

We will fit equations (13)–(15) simultaneously for a combined fit to all Cepheid and SN Ia data. We rewrite these equations, making explicit the indexing: i varies over the eight nearby galaxies (and the SNe Ia they contain), j varies over Cepheids in these galaxies and NGC 4258, k varies over the low-z SNe.

$$m_{\mathrm{W}ij} = b_{\mathrm{W}}(\log_{10} P_{ij} - 1) + Z_{\mathrm{W}}\Delta \log_{10}[\mathrm{O/H}]_{ij}$$
$$+ M_{\mathrm{W}} + \mu_{4258} + \Delta\mu_i \tag{16}$$

$$m_{\mathrm{B}i} = M_{\mathrm{B}}^* - \alpha X_{1i} + \beta C_i + \mu_{4258} + \Delta\mu_i \tag{17}$$

$$m_{\mathrm{B}k} = M_{\mathrm{B}}^* - \alpha X_{1k} + \beta C_k + 5\log_{10}(cz_k f(z_k)) - \mathcal{H}. \tag{18}$$

In equation (18), we separate the intercept of equation (15) into parameters M_{B}^* (also appearing in equation (17)) and a constant term $\mathcal{H}$, which contains the same information as H_0:

$$\mathcal{H} := 5\log_{10} H_0 - 25. \tag{19}$$

We fit for all 16 parameters appearing in equations (16)–(18); explicitly these are $\Theta = \{\alpha, \beta, \mathcal{H}, M_{\mathrm{B}}, b_{\mathrm{W}}, Z_{\mathrm{W}}, M_{\mathrm{W}}, \mu_{4258}, \Delta\mu_i\}$ where i varies over the eight nearby galaxies. Note that we fit for M_{B} instead of M_{B}^* as the latter is not a constant. The distance moduli in equations (16) and (17) are expressed as offsets $\Delta\mu_i \equiv \mu_i - \mu_{4258}$, relative to NGC 4258.

Equations (16)–(18) assume a distance anchor of NGC 4258. The use of the LMC and MW as alternate or additional anchors is explored, and discussed in Appendix A2. We impose a strong Gaussian prior $\mu_{4258} = 29.404 \pm 0.066$ on the distance, measured from VLBI observations of megamasers in Humphreys et al. (2013)[11], whenever NGC 4258 is used as an anchor, and similarly $\mu_{\mathrm{LMC}} = 18.494 \pm 0.049$ if the LMC is included.

3.4 Steps in fitting process

We break the process of fitting all data to equations (16)–(18) into three steps to streamline the process: the data and parameters are separated into spheres of influence so that results from the Cepheid- and SN-only fits – in particular their dependencies on factors such as rejection, cuts, and distance anchors – can be isolated, inspected, and selectively carried forward to the global fit.

The three steps are as follows. First, we fit all Cepheid data simultaneously for parameters $\{b_{\mathrm{W}}, Z_{\mathrm{W}}, M_{\mathrm{W}}, \{\mu_i\}\}$ to equation (16). Separately, we fit only the low-z SNe Ia to equation (18). The parameters M_{B} and $\mathcal{H}$ are degenerate when constrained by only the low-z data, so we fit for their difference $\mathcal{M} := M_{\mathrm{B}} - \mathcal{H}$, as well as SN Ia parameters α and β. Finally, a global fit is performed (independent of the first two steps) of both data sets *and* the nearby

SNe Ia to equations (16)–(18) simultaneously. This step is similar to the Cepheid-only fit but also includes $\mathcal{H}$ and the SN parameters $\{\alpha, \beta, M_{\mathrm{B}}\}$. Final values for all parameters including H_0 are extracted from this global fit. Each preliminary fit is described in detail in Sections 4.3 and 5.4, and the global fit in Section 6.1.

The Bayesian methods for parameter estimation (MultiNest for the high-dimensional Cepheid-only and global fits, and MCMC for the SN-only fit – described in Section 2.3) require priors, which may be uniform, on each parameter in Θ. While some other parameters are predominantly influenced by a subset of the data (namely the nuisance parameters b_{W} and Z_{W} which only appear in the Cepheid-only fit, and α and β which are predominantly determined by low-z SNe), it would be statistically invalid to place Gaussian priors on these parameters in the global fit based on results of either preliminary fit. However, non-uniform priors based on external data are allowed; our priors on μ_{4258} (and μ_{LMC}) are Gaussian if these galaxies are included as calibrators, and we constrain b_{W} with a Gaussian prior informed by the LMC Cepheids in fits which are not anchored on the LMC (discussed in Appendix A4). For the remaining parameters in Θ, we set uniform priors over generous intervals.

Our approach differs from the R11 and E14 analyses, which both perform two independent steps: (i) using only the low-z SN data, determine and fix a_{V} (the intercept of the SN Ia m–z relation equivalent to $0.2\mathcal{M}$ in our analysis) and (ii) from the Cepheids only, determine the Leavitt law parameters b_{W}, Z_{W}, and zp_{4258} (a zero-point comparable to our M_{W}). The Cepheid parameters are combined with the nearby SNe Ia light curves to find the quantity $m_{v,4258}^0$ which signifies the fiducial peak apparent magnitude of an SN Ia in NGC 4258; this quantity is then combined with a_{V} and μ_{4258} to give H_0 (R11, equation 4). We emphasize that, in contrast, our final global fit is truly simultaneous in that it allows each parameter in Θ to be influenced by all Cepheid and SN data in the nearby galaxies and low-z sample. Consequently, we allow the data sets to interact freely with each other, enabling us to capture covariances between parameters.
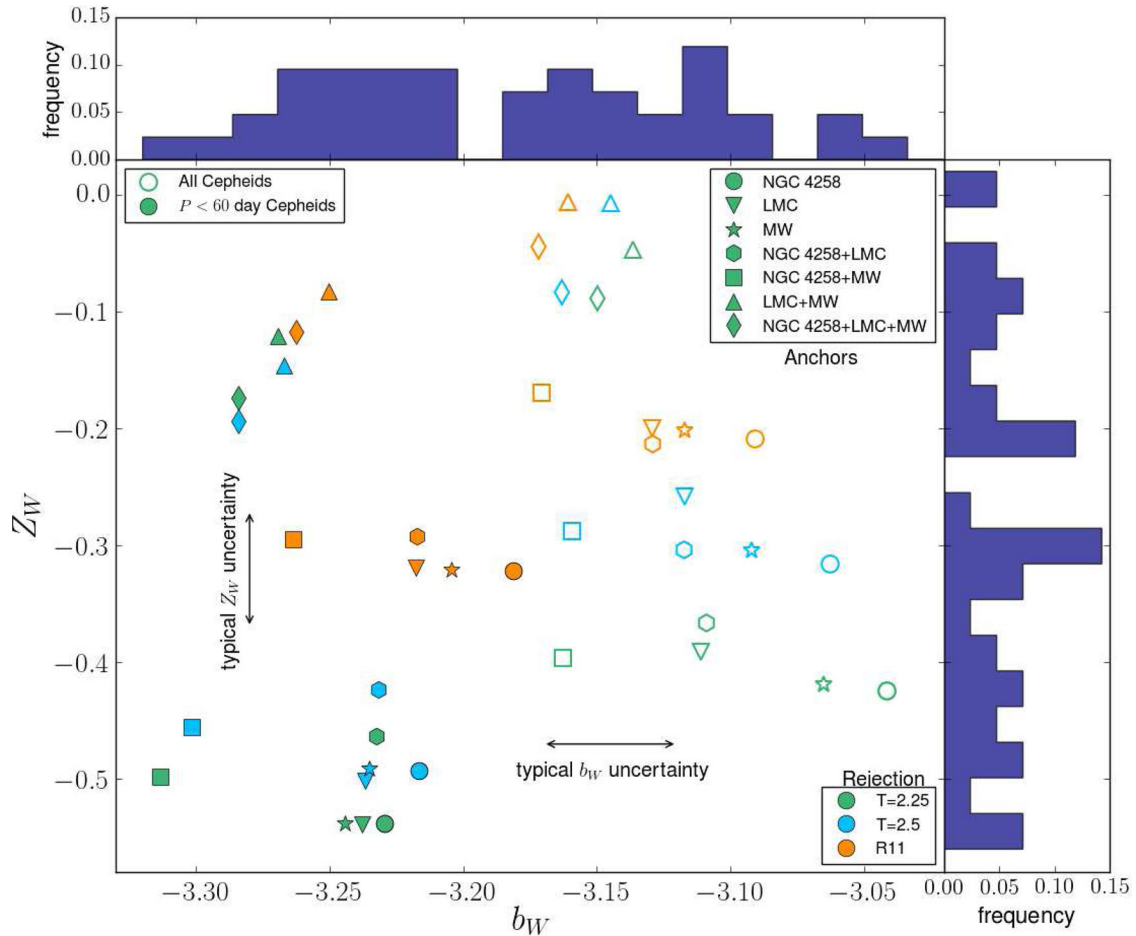
4 CEPHEID LEAVITT LAW FIT

Here, we describe an initial simultaneous fit of the Cepheids in all nine galaxies to the Leavitt law (equation 16). This has two purposes: to estimate the parameters $\{b_{\mathrm{W}}, Z_{\mathrm{W}}, M_{\mathrm{W}}, \{\mu_i\}\}$ for each fit (which uniquely define a Cepheid data set), and to examine the dependence of these parameters (particularly the period and metallicity coefficients b_{W} and Z_{W}) on factors explored in R11 and E14 – namely the rejection algorithm and threshold, distance anchor, and inclusion of longer period Cepheids, discussed in Appendices A1–A3. Some of these fits, with associated Cepheid data sets, are selected to be carried forward to the global fit.

We emphasize that the process of choosing these fits is motivated by the desire to capture and quantify variation that arises in results when different (but also valid) choices are made in the fitting process, rather than by the aim of choosing a 'best' fit; this will become clear in Fig. 1 and its discussion. Thus, we do not blind this part of the analysis (the Cepheid-only fit), because the results are not final, and also because they do not directly reveal or affect the value of H_0.

4.1 Observations

The Cepheids in the nine galaxies in Table 1 were discovered or re-observed in the Supernovae and H_0 for the Equation of

---

[11] This distance is slightly higher than the older value $\mu_{4258} = 29.31$ assumed in Riess et al. (2012); this increase acts to decrease H_0 relatively.

Figure 1. The best-fitting values for b_W, Z_W from all Cepheid-only fits to the Leavitt law (equation 16), assuming various distance anchors and rejection algorithms, with and without a cut on the period. The different markers represent these properties as indicated in the legends, with the colour representing the outlier rejection algorithm, shape representing the distance anchor, and solidness reflecting the period cut. We consider all seven combinations of distance anchor galaxies NGC 4258, LMC, and MW (Appendix A2), and all three rejection algorithms (Appendix A1). This figure shows: (i) including the longer period Cepheids increases both b_W and Z_W (empty markers lie up and to the right of solid markers). (ii) Systematic variation in parameters with distance anchor (e.g. for each choice of period cut, the NGC 4258 + MW anchor gives the lowest b_W and the NGC 4258-only anchor gives the highest); meanwhile fits with both the LMC and MW as anchors (diamonds and upward triangles, with and without NGC 4258, respectively) are clustered tightly, indicating that these two galaxies together provide a strong constraint on both parameters. (iii) The R11 rejection results in less negative Z_W and to a lesser extent b_W (reflected in orange markers concentrated in the upper right portion of the figure), while the E14 algorithm with rejection threshold $T = 2.5$ (turquoise) results in higher Z_W compared to $T = 2.25$ (green) for fits other than those with both the LMC and MW anchors. The typical uncertainties, indicated by the arrows, are ∼0.05 for b_W and ∼0.1 for Z_W for most fits, but can be larger for some anchors or rejection algorithms. Evidently the scatter arising from varying the distance anchor, cut on period, and rejection far exceeds the statistical uncertainty. The histograms in the margins display distributions of b_W and Z_W values over all fits. The histogram for b_W shows that values are clustered around $b_W \sim -3.25$ for fits with a $P < 60$ d cut (reflective of the influence of the LMC Cepheids) and $b_W \sim -3.10$ for fits without. The histogram for Z_W shows a spread centred at $Z_W \sim -0.3$, dependent on distance anchor; fits with both the LMC and MW anchors lie with $-0.2 < Z_W < 0$.

State (SH0ES) project (Riess et al. 2009b) on the *HST*, from Cycle 15. Infrared (F160W) observations of the SN Ia host galaxies were made using the Wide Field Camera 3 (WFC3). We refer the reader to R11, Section 2 for descriptions of observations and data reduction. Our initial data set consists of 570 Cepheids from R11, table 2, excluding those marked 'low P'; this number is reduced to 488 if we adopt the $P < 60$ d cut on Cepheids, following E14.

We supplement the sample of 157 Cepheids in NGC 4258 with LMC and MW Cepheids, used as alternative anchors (discussed in Appendix A2). Persson et al. (2004) present near-infrared photometry of 92 Cepheids, of which 53 have optical measurements in Sebo et al. (2002), which we use for determining Wesenheit magnitudes. Two of these 53 Cepheids have period greater than 60 d, which

we exclude if we impose the period cut on the Cepheids in the SN host galaxies. We also make use of 13 Cepheids in the MW from van Leeuwen et al. (2007, table 2, excluding Polaris, an overtone pulsator), which have combined parallaxes from *Hipparcos* and *HST* data.

4.2 Cepheid systematics

Cepheid variables are powerful distance indicators to nearby galaxies, however they are subject to systematics. We briefly mention those that affect our method, and refer the reader to Freedman & Madore (2010, section 3.1) and references therein for further discussion of Cepheid systematics. In Appendices A1–A3, we test and report the dependence of the Leavitt law parameters on aspects of

the Cepheid fit, namely outlier rejection, distance anchor, and cut on Cepheid period.

Careful treatment of Cepheids starts with their discovery and identification, where crowding and confusion can lead to misidentification. Light from a Cepheid can be blended with nearby or background sources, and aliasing or sampling problems can cause the wrong period to be inferred. Thus, outliers from the Leavitt law fit must be identified and rejected. Moreover, the intrinsic scatter in the Leavitt law must be taken into account in assessing the goodness of fit; outliers that are rejected should lie well outside the so-called instability strip.

The secondary dependence of Cepheid luminosities on atmospheric metallicity is an ongoing area of research, and remains contentious. This effect arises from changes in the atmospheres and structure of Cepheids with their chemical composition, which impacts colours and magnitudes. There is evidence of a mild metallicity dependence at optical wavelengths (Kennicutt et al. 1998; Sakai et al. 2004; Macri et al. 2006; Scowcroft et al. 2009), which is weaker in the infrared. In the LMC, using spectroscopic [Fe/H] measurements, Freedman & Madore (2011) find that Z_H (the metallicity dependence in the H band) is close to zero. Efstathiou (2014, section 3.2) argues that these LMC observations, along with theoretical considerations, give cause to applying an external prior on the metallicity dependence centred at $Z_W \sim 0$. We discuss this prior, which we find is inconsistent with the R11 data, in Appendix A4.

Historically, the zero-point of the Leavitt law has proven difficult to measure, due to uncertainties in parallax measurements. To circumvent this, more accurate absolute distances have been pursued, including VLBI measurements of water megamasers in NGC 4258 (Humphreys et al. 2013). Multiple distance anchors are also tested and combined to reduce the impact of any single distance anchor. The effects of varying and combining anchors is explored in this analysis in Appendix A2, following R11 and E14.

4.3 Cepheid-only fit

Our fit to all Cepheid data is based on E14 with the difference that we do not assume the SN Ia zero-point (the quantity a_V in R11 and E14) or indeed any SNe data. This is because we intend to fit the Cepheids separately from the SN data, whereas E14 calculates values of H_0 from the Cepheid fits, assuming SN Ia data from R11. All Cepheid data are fit to the Leavitt law (equation 16) with MultiNest (Section 2.3.1). The 12 parameters of fit include the three nuisance parameters $\{b_W, Z_W, M_W\}$, the strongly constrained distance μ_{4258}, and the eight distance modulus offsets $\{\Delta\mu_i\}$. We set an external Gaussian prior on μ_{4258}, and by default place uniform priors for all other parameters over generous intervals. The χ^2 function for the Cepheid fit is a function of $\{b_W, Z_W, M_W, \mu_{4258}\}$, and $\{\Delta\mu_i\}$, and takes the form

$$\chi_c^2 = \sum_{ij} \frac{(\hat{m}_{Wij} - m_{Wij,\mathrm{mod}})^2}{\hat{m}_{Wij,\mathrm{err}}^2 + \sigma_{\mathrm{int,C}}^2}. \tag{20}$$

Here, $m_{Wij,\mathrm{mod}}(b_W, Z_W, M_W, \mu_{4258}, \{\Delta\mu_i\})$ is the model magnitude of the jth Cepheid in galaxy i (given by equation 16) and $\sigma_{\mathrm{int,C}}$ is the intrinsic scatter in Cepheid magnitude, from the width of the instability strip. For clarity, measured quantities are denoted with hats to distinguish them from model quantities. The logarithm of the likelihood $\mathcal{L} = e^{-\chi_c^2/2}$ and the priors on the fit parameters are

inputs for MultiNest. We use 1000 live points in MultiNest and confirm that the precision is sufficient.[12]

4.4 Results of Cepheid-only fit

The results of all Leavitt law fits, for all combinations of distance anchor, outlier rejection, and upper period limit, are presented in Table D1. The details of these choices are given in Appendices A1–A3, along with the effect they have on fit results. The variation in the fits is visualized in Fig. 1 in b_W, Z_W space. The choice of these two parameters is obvious as they characterize the Leavitt law and are solely influenced by the Cepheid sample – all other parameters in Θ are influenced by the SN data, even the zero-point M_W. Fig. 1 allows us to identify which of the Cepheid fits lie at the edges of the parameter space. The resultant scatter observed in Fig. 1 far exceeds the statistical uncertainties reported in Table D1. Therefore, it is paramount that the systematic associated with varying the choices made in Appendices A1–A3 is propagated carefully through the entire analysis process.

The choice of whether or not to apply the upper period limit of $P < 60$ d has the most effect on the parameters, especially b_W. Fig. 1 reveals clearly the impact of including the longer period Cepheids on parameters b_W and Z_W, most notably splitting Fig. 1 down the middle vertically, i.e. by Leavitt law slope. Both parameters are smaller in magnitude by ~0.1 when the longer period Cepheids are included, indicating a weaker dependence of Cepheid magnitude on both period and metallicity. For the slope b_W, this difference dominates the statistical uncertainty and any other variation in b_W, whereas for Z_W, the resultant change from changing the period cut is comparable in size to the dependence on rejection algorithm, and the statistical uncertainty.

When the longer period Cepheids are included, each of b_W and Z_W is better constrained by the distance anchor, and the rejection algorithm, respectively: this is reflected in the vertical lines of empty markers with the same shape, and near-horizontal lines of markers with the same colour. That is, when the $P < 60$ d cut is applied, the fit results are more sensitive to the choice of rejection algorithm and distance anchor. However, even without the cut, there remain strong dependencies of Z_W on rejection, and of b_W on distance anchor.

Within each choice of period cut, the slope b_W varies systematically with distance anchor: the NGC 4258 + MW and NGC 4258 anchors result in the lowest and highest b_W, respectively, with results from the other anchor combinations lying in between. The fits with both the LMC and MW in the anchors (upward triangles and diamonds) have the least spread in both parameters. With the exception of these fits, the data suggest a reasonably strong metallicity dependence with $-0.5 < Z_W < -0.2$. As noted above, the results are sensitive to rejection algorithm, with the R11 rejection resulting in less negative values for Z_W (and for b_W with the $P < 60$ d cut), followed by the E14 rejection with $T = 2.5$ to a smaller extent.

We observe (Table D1) that there is little difference in values for M_W between fits with and without the $P < 60$ d cut, with the difference decreasing to zero for fits anchored on both n4258 and the MW. However, we defer further comment on M_W (as well as $\{\Delta\mu_i\}$) to the discussion of global fit results. As M_W is a magnitude zero-point, and the $\Delta\mu_i$ are affected by the nearby SNe, the values

---

[12] For selected fits, we repeat the outlier rejection and fitting steps, and find that the scatter in final parameters within 10 runs is <1 per cent of the statistical uncertainty.

Table 2. Summary of selected Cepheid fits to carry forward to global fit (i.e. rejection, anchors, and period cut used). The positions of the best-fitting values for b_W and Z_W in the b_W, Z_W-plane (represented in Fig. 1) are also given, as well as the symbols for these fits in Fig. 1. The top half of the table (solid symbols) lists fits with the $P < 60$ d cut, whilst the bottom half (empty symbols) contains fits without.

	Rej (T)	Anchor[a]	Symbol
Top left	2.25	n4258+LMC+MW	Solid green diamond
Top left	2.5	n4258+LMC+MW	Solid turquoise diamond
Top left	R11	n4258+LMC+MW	Solid orange diamond
Top left	R11	LMC+MW	Solid orange Δ
Middle	2.5	n4258+LMC	Solid turquoise hexagon
Middle	R11	MW	Solid orange star
Lower left	2.25	n4258+MW	Solid green square
Lower	2.25	LMC	Solid green ∇
Lower	2.25	n4258	Solid green circle
Top	2.25	n4258+LMC+MW	Empty green diamond
Top	2.5	n4258+LMC+MW	Empty turquoise diamond
Top	R11	n4258+LMC+MW	Empty orange diamond
Top	R11	LMC+MW	Empty orange Δ
Top	2.25	LMC+MW	Empty green Δ
Middle	2.25	n4258+MW	Empty green square
Right	R11	n4258	Empty orange circle
Right	2.5	n4258	Empty turquoise circle
Lower right	2.25	n4258	Empty green circle

Note. [a]For typographic ease, we abbreviate 'NGC' to 'n'.

Table 3. Observations of nearby SNe Ia in Table 1, including sources of photometry, SALT2 instruments, magnitude systems (including filters) where available. Light curves of the two earliest SNe were given as standard photometry only.

SN Ia	Photometry source	Magnitude system and filters
SN 1981B	Buta & Turner (1983)	Standard *UBVR*
SN 1990N	Lira et al. (1998)	Standard *UBVRI*
SN 1994ae	Riess et al. (2005)	AndyCam[a] *BVRI*
SN 1998aq	Riess et al. (2005)	4Shooter/AndyCam *UBVRI*
SN 1995al	Riess et al. (2009a)	AndyCam *UBVRI*
SN 2002fk	CfA3[b]	4Shooter2 *UBVRI*
	LOSS[c]	KAIT3/NICKEL *BVRI*
SN 2007af	CfA3	Keplercam *BVri*
	LOSS	KAIT3/KAIT4 *BVRI*
SN 2007sr	CfA3	Keplercam *BVri*
	LOSS	KAIT3/4 *BVRI*

Notes. [a]A thin, back-illuminated CCD camera on the FLWO 1.2 m telescope (Jha et al. 2006).
[b]Hicken et al. (2009a).
[c]Ganeshalingam et al. (2010). Both CfA3 and LOSS photometries were available for the most recent three SNe Ia, so we used combined photometry from both sources as described in Appendix B1.1.

of these parameters have potential to be influenced by the SN Ia data, and are expected to change with their inclusion.

4.4.1 Comparison to *R11* and *E14*

We compare our fits in Table D1 to equivalent results in R11 and E14: our fits with R11 rejection and no period cut are compared to bolded fits in R11, table 2, and we compare our fits with the $P < 60$ d cut to the results in E14, tables 2– 4 without priors on b_W and Z_W. Relative to R11, our b_W values with LMC-only or MW-only anchors are slightly lower in magnitude (~ -3.12 instead of -3.19 in R11, a $\sim 1\sigma$ difference). Moreover our fits with LMC + MW anchors result

Table 4. Results of preliminary SN-only fits for various cuts.

SN cut	N_{SN}	α	β	$\mathcal{M}$
Default	171	0.164 (0.013)	3.07 (0.14)	−3.240 (0.036)
Higher χ^2	175	0.167 (0.013)	3.12 (0.13)	−3.244 (0.038)
Lower χ^2	163	0.158 (0.013)	3.04 (0.16)	−3.256 (0.038)
$z > 0.0233$	96	0.163 (0.016)	2.73 (0.17)	−3.252 (0.038)
Stricter C	160	0.158 (0.015)	2.93 (0.18)	−3.238 (0.037)
Str. σ_{X_1}, σ_C	164	0.171 (0.014)	3.10 (0.14)	−3.232 (0.038)
Str. σ_{X_1}	165	0.171 (0.013)	3.10 (0.15)	−3.245 (0.037)
Str. $E(B - V)$	166	0.167 (0.013)	3.06 (0.15)	−3.241 (0.036)
$t_{1st} < +10$d	187	0.165 (0.013)	3.11 (0.14)	−3.234 (0.035)

in a lesser metallicity dependence ($-0.2 < Z_W < -0.1$ instead of $Z_W \sim -0.3$ in E14) – however uncertainties in Z_W in these E14 fits exceed 0.1, and our Z_W values (without the period cut) are supported by R11. Aside from these differences, our results are in good agreement with R11 and E14, lying well within ranges allowed by statistical uncertainties. We retain 444 Cepheids when adopting the rejection flagged in R11, table 2 (close to the minimum of 448 reported in table 4 of R11) and only 379 with the $P < 60$ d restriction. Applying the E14 rejection algorithm, our fits consistently result in lower numbers of remaining Cepheids by 10–20, and consequently slightly lower $\sigma_{int, C}$. It is worth noting that our methodology differs from E14 (and R11) in that we do not involve any SNe in the fit (omitting the third term in equation 14 of E14), whilst E14 includes the SN fit results by assuming a value of a_V taken from R11. Presumably, the complex ways of probing the multidimensional parameter space are leading to differences, albeit slight, between this work, R11, and E14, that cannot be easily reconciled. We believe a solution for the future is for authors to provide code and data sets used for calculations as part of publication that can be used to better understand differences.

4.4.2 Selection for global fits

The choice of Cepheid fits to carry forward to the global fit is informed by their results, i.e. Leavitt law slope b_W and metallicity dependence Z_W, as these parameters are only influenced by the Cepheid sample and are very minimally affected by the SN data. We are interested in the effect the choice of Cepheid sample (through varying aspects of the fit such as distance anchor, rejection, and upper period limit) has on these parameters in the global fit. In particular, it is essential to quantify the systematic uncertainty in $\mathcal{H}$ with varying these choices.

We select 18 fits in total, summarized in Table 2. To span the full range of uncertainty induced by various Cepheid fits, we select fits at extremes of the parameter space (Fig. 1), with a selection of anchors and rejection algorithms. The combination of all three distance anchors has the most constraining power, so we include all of these fits to quantify the uncertainty within them.

Each fit has an associated set of best-fitting parameters with uncertainties, as well as (unless using the R11 rejection) the values of the intrinsic scatter and rejection threshold, which together uniquely define a set of Cepheids remaining after outlier rejection. These then make up the Cepheid data and priors for some parameters in Θ, going into the global fit (Section 6).

5 SUPERNOVA FIT

We now focus on the SNe Ia. First, we outline the data set and discuss systematics, then we describe various cuts on the SNe Ia and present

the preliminary SN-only fit. This section is supplemented by details provided in Appendices B1–B4 on the light-curve fitting method, and the corrections applied for Malmquist bias, host galaxy mass, and peculiar velocities respectively. Also central to the subject are the computations of SN systematics in covariance matrices, which are also relegated to Appendix C for detailed discussion.

5.1 Observations

Our SN data are identical to R11, consisting of eight 'nearby' SNe Ia in the galaxies hosting Cepheids (Table 1), and 280 unique 'low-z' SNe Ia from the 185 CfA3 (Hicken et al. 2009a) and 165 LOSS (Ganeshalingam et al. 2010) samples.[13] Details of sources of photometry for the nearby SNe are presented in Table 3. Natural photometry was not available for the oldest two, SN 1981B and SN 1990N. The most recent SNe are already in both CfA3 and LOSS, so we used combined photometry from both sources as described in Appendix B1.1. The remaining three (SN 1994e, SN 1995al, and SN 1998aq) were observed on the Fred Lawrence Whipple Observatory (FLWO) 1.2 m telescope with a variety of CCDs; we construct SALT2 instruments (including transmissions and zero-points) using data from Jha et al. (2006).

CfA3 ran from 2001 to 2008 on the 1.2 m telescope at FLWO almost entirely with the CfA3 4Shooter2 and Keplercam imagers (in *UBVri* and *UBVRI* filters, respectively), while LOSS took place on the NICKEL and KAIT telescopes from 1998 to 2008 (in *BVRI*). Unlike more recent magnitude-limited surveys, CfA3 and LOSS targeted known galaxies and include SNe discovered by other sources, resulting in a more complex selection function and generally resulting in higher host galaxy masses (Appendix B3). We refer the reader to the above works for further details of observations. Newer low-z SNe Ia samples have since been published, notably CfA4 (Hicken et al. 2012), Carnegie Supernova Project (Contreras et al. 2010), Pan-STARRS (Rest et al. 2014), Palomar Transient Factory (Law et al. 2009), and La Silla-QUEST Supernova Survey (Walker et al. 2015). However, we retain the older CfA3–LOSS sample for this analysis to more faithfully compare our results to R11 and E14.

Photometry for the low-z sample is sourced from Hicken et al. (2009b) and Ganeshalingam, Li & Filippenko (2013) in the natural systems of each filter set, with the exception of the CfA3 4Shooter2 and Keplercam *U* filters for which reliable measurements do not exist – we use photometry in the standard Johnson–Cousins *UBVRI* system as presented in Bessell (1990) for these passbands only, as well as the nearby SN 1981B and SN 1990N. We use SALT2 (Guy et al. 2007) to fit these SN Ia light curves for the quantities m_B, X_1, and C, which are used to derive distances via equation (14). Details of the light-curve fitting are given in Appendix B1.

One reason for our choice of SALT2 as a light-curve fitter is that our framework for assessing SN Ia systematic uncertainties with covariance matrices (Section 5.2 and Appendix C) follows that in the SNLS–SDSS Joint Lightcurve Analysis (hereafter JLA; Betoule et al. 2014), which relies on the SALT2 model. In addition, SALT2 is the most modern fitter and used ubiquitously in cosmology analyses; thus our use allows for easier comparison and greater consistency. While R11 test the effects of fitting light curves with both SALT2

and MLCS2k2 (Jha, Riess & Kirshner 2007)[14] light-curve fitters, we use SALT2 only. This is justified, as the latest version SALT2.4 (described in Betoule et al. 2014) was released in parallel with simulations in Mosher et al. (2014) which assess and quantify the uncertainty associated with the choice of light-curve fitter (and the light-curve model itself) in covariance matrices (Appendix C1). Hence, it is unnecessary to use of multiple fitters to assess the aforementioned systematic uncertainty.

5.2 Supernova systematics

As a statistical sample, SNe Ia are high fidelity standard candles. However, as astronomical objects, SNe Ia are diverse and subject to systematics, with their measurable quantities (absolute brightness, observed colour, and decline rate) dependent on factors which correlate with their progenitors and environments. Countless investigations into these correlations and their origins are partly motivated by the need to reduce residual scatter from these intrinsic SN Ia variations. Observations of SNe are also influenced by factors such as galactic extinction, misclassifications, and differing telescope magnitude systems. Most of these effects are not sufficiently well understood or accurately modelled to correct for them entirely. It is therefore essential to quantify the size of systematics; even when efforts have been made to apply corrections we still wish to estimate the uncertainty in the correction.

Our approach to accounting for SN Ia uncertainties follows methods in JLA, which are largely based on those in the Supernova Legacy Survey (hereafter SNLS; Conley et al. 2011). These use individual covariance matrices for each systematic, tracking correlated uncertainties between different SN quantities (i.e. m_B, X_1, and C), between different SNe. Advantages of the covariance matrix method over the more traditional method of adding systematics in quadrature are discussed in Conley et al. (2011, section 4); these include the ability to fully capture correlations in uncertainties, and the ease of including or reproducing uncertainties in further analyses. Details are our computations are provided in Appendix C.

5.3 Cuts on supernova sample

We make quality cuts on our SN Ia sample to eliminate potential biases from poorly constrained light curves and peculiar events, and to remain within the bounds of the SALT2 model. With the intent of replicating the sample in R11 as closely as possible, we broadly follow the cuts described in CfA3 (Hicken et al. 2009b) and LOSS (Ganeshalingam et al. 2013), also using cuts in SNLS and JLA – described in Guy et al. (2010, section 4.5), Conley et al. (2011, section 2.1), Betoule et al. (2014, section 4.5) – as guidance or as alternate cuts. In summary, our criteria are as follows:

(i) low MW extinction $E(B - V) < 0.2$;
(ii) exclude local SNe Ia not in the Hubble flow $z > 0.01$;
(iii) goodness of fit from SALT2 $\chi^2/\text{d.o.f.} < 8$;
(iv) first detection by $+5$ d, relative to *B*-band maximum;
(v) exclude stretch outliers $|X_1| < 3$;
(vi) exclude colour outliers $|C| < 0.5$;
(vii) well-constrained stretch $\sigma_{X_1} < 0.8$;
(viii) well-constrained colour $\sigma_C < 0.1$.

---

[13] There are 69 SNe in common between the samples; however SN 1998es was discarded because the light-curve quality was so poor that the SALT2 light-curve fit failed.

[14] SALT2 differs from MLCS2k2 substantially in its treatment of extinction: instead of prescribing a reddening parameters R_V, all of the colour information (including the SN's intrinsic colour and host extinction) is included in the single colour parameter *C*.

The above encompass cuts in CfA3 and LOSS, with stricter cuts on the date of first detection and light-curve goodness of fit (originally at $+10$ d and $\chi^2/\text{d.o.f.} = 15$ in CfA3, respectively), and with additional cuts on the uncertainties in X_1 and C to further exclude SNe which have large uncertainties in their stretch or colour. Our cuts are also informed by visual inspection of individual light curves and their SALT2 fits, particularly in placing boundaries for the light-curve goodness of fit, uncertainties in stretch and colour, and date of first detection. In summary, we exclude SNe at very low redshift (i.e. not yet in the Hubble flow), significantly extinguished by MW dust, detected too late, with poorly constrained stretch and colour. We also exclude SNe Ia with poor SALT2 fits, and SNe that are too blue or red or have very fast or slow decline to exclude peculiar objects and ensure our sample fit within the SALT2 model.

Furthermore we test some alternate cuts, including some suggested in JLA and original CfA3/LOSS cuts which we have changed above. We repeat the SN-only fit with these cuts to test the effect on the SN fit parameters, carrying some through to the global fit. In particular, we follow R11 in raising the low-redshift cut to $z = 0.0233$,[15] and test strengthening or relaxing the light-curve goodness-of-fit threshold to $\chi^2/\text{d.o.f.} < 5$ or $\chi^2/\text{d.o.f.} < 15$, and relaxing the date of first detection to $+10$ d. Following JLA, we examine the effects of imposing a stricter bound on the colour ($|C| < 0.3$), the uncertainty on the stretch ($\sigma_{X_1} < 0.5$), and MW extinction. These tests are important as the influence of these alternate cuts on the fit results is not straightforward or obvious; moreover no particular cut is necessarily more valid than the others. We discuss these results and their significance in Section 5.5. Histograms showing X_1 and C distributions for several cuts are included in Appendix B5.

5.4 SN-only fit

Analogous to the Cepheid-only fit in Section 4.3, we perform a preliminary fit of only the low-z SNe Ia to equation (18) using the MCMC routine emcee (Section 2.3.1), to identify the dependence of the SN parameters on the different cuts in Section 5.3. To clearly separate the data and model in equation (18), we define the quantity $m_{\text{B}}^{\dagger}$ for the apparent SN magnitude corrected for stretch and colour:

$$m_{\text{B}}^{\dagger} := m_{\text{B}} + \alpha X_1 - \beta C,$$
$$\text{with} \quad \hat{m}_{\text{Bmod}}^{\dagger} = 5 \log_{10}(czf(z)) + M_{\text{B}}^* - \mathcal{H}. \tag{21}$$

Explicitly the χ^2 function for the low-z SN fit is

$$\chi^2_{\text{SN}} = \left(\hat{\boldsymbol{m}}_{\text{B}}^{\dagger} - \boldsymbol{m}_{\text{Bmod}}^{\dagger} \right) \mathbf{C}_{\boldsymbol{m}_{\text{B}}^{\dagger}}^{-1} \left(\hat{\boldsymbol{m}}_{\text{B}}^{\dagger} - \boldsymbol{m}_{\text{Bmod}}^{\dagger} \right)^T \tag{22}$$

where the covariance matrix $\mathbf{C}_{\boldsymbol{m}_{\text{B}}^{\dagger}}$ is derived from covariances in all SN parameters $\{m_{\text{B}}, X_1, C\}$, as given in equation (C1) in Appendix C along with detailed explanations of statistical and systematic contributions.

It is evident from equations (18) and (21) that the SN-only fit is degenerate: we cannot constrain both M_{B} and $\mathcal{H}$ simultaneously; the nearby SNe are necessary to constrain M_{B}. Instead, we fit for the difference $\mathcal{M} := M_{\text{B}} - \mathcal{H}$, adopting the blinds for each M_{B} and $\mathcal{H}$ noted in Section 2.4 i.e. with the transformations $m_{\text{B}} \mapsto m_{\text{B}} + \mathfrak{o}_{M_{\text{B}}}$ in equations (17) and (18) and $\mathcal{H} \mapsto \mathcal{H} + \mathfrak{o}_{\mathcal{H}}$ in the likelihood incorporating equation (22) (a function of both M_{B} and $\mathcal{H}$ through

---

[15] This is to reduce possible bias from local coherent flows, or a possible local underdensity (a so-called Hubble bubble). The latter is discussed in R11 and Conley et al. (2011); however there is no conclusive evidence for its existence.
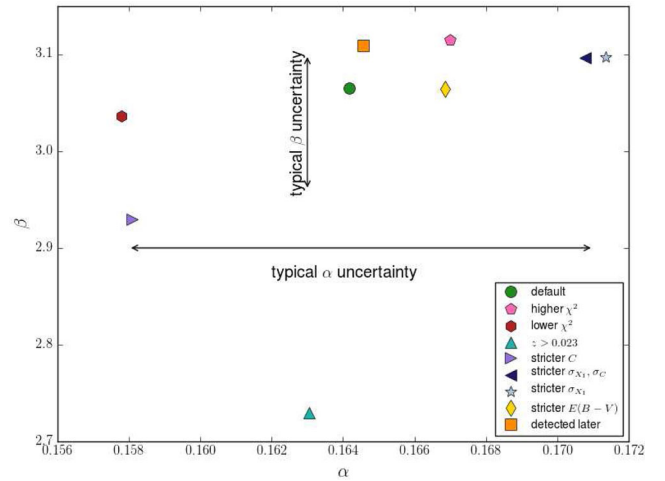
Figure 2. The best-fitting values for α, β from all SN-only fits to equation (18), assuming various cuts on the low-z SNe. The different markers represent the cuts described in Section 5.3. The typical statistical uncertainties are indicated by the arrows. The variation in α is comparable to the statistical uncertainty, and the same is true for β if we disregard the higher low-redshift cut.

equation 21). The marginalized posterior distributions (mean and 1σ width) for α and β are presented in Table 4 and plotted in Fig. 2; these results are dependent on the choice of quality cuts on the SN sample described in Section 5.3.

5.5 Results of SN-only fit

The results of the SN-only χ^2-minimizing fit are presented in Table 4, while Fig. 2 shows the differences in fits with various SN cuts lie in the α, β-plane (this is analogous to Fig. 1, which displays the numerous Cepheid fits in $b_{\text{W}}, Z_{\text{W}}$-space). We discuss the dependence of the fit results on the various cuts, and select cuts with results spanning the parameter space to carry forward to the global fit to assess the associated systematic uncertainty.

The notable outlier is the higher low-redshift cut ($z > 0.0233$), effecting a much lower value of β than the other cuts. This cut, along with the stricter colour and stricter goodness-of-fit cuts, results in lower α also. The lowest and highest values of α correspond to lower χ^2, and stricter σ_{X_1}, respectively. Fig. B4 in Appendix B5 shows normalized $X1$ and C distributions for the $z > 0.0233$ cut: there are marginally slower declining SNe compared to the default, but overall the distributions appear similar. It does not appear that the discrepant fit results from this cut are the result of a change in the colour or stretch distribution of the sample; indeed our tests with jackknifed samples (described below) indicate this is likely the result of removing a large portion of the sample (over 40 per cent relative to the default). Disregarding the $z > 0.0233$ cut, the variation in α and β with the different cuts we test appears only slightly larger than the typical statistical uncertainties in these parameters (Fig. 2).

We use jackknife resampling to assess the statistical significance of the dependence of results on the cuts in Table 4. For several cuts (the lower light curve $\chi^2/\text{d.o.f.}$, higher redshift cut, and stricter cuts on colour or uncertainties in stretch and colour), we draw subsamples of size N_{SN} (Table 4) of the 171 SNe selected by the default cut. For each cut, we compare the systematic change in fit results (parameters α, β, and $\mathcal{M}$) from the new cut to results from repeated jackknifed subsamples of size N_{SN} and their scatter. These reveal a systematic variation of 1σ–3σ from the default for almost

all combinations of parameters and cuts (where σ is the scatter within the numerous jackknifed subsamples). Thus, the differences between rows of Table 4 cannot be solely attributed to shot noise, and the variation due to different cuts must be propagated to the global fit (Section 6) and treated as a contribution to the total systematic uncertainty. However, we will find that the variation from the choice of SN cut is dwarfed by the analogous source of uncertainty from the choice of Cepheid fits.

6 GLOBAL FIT RESULTS

This section contains our final simultaneous fits to all Cepheid and SNe Ia data. We set out parameters and equations for this fit, and present fit results for all parameters, including the dependence of results on choices within the individual Cepheid and SN data sets. We summarize our uncertainties, and discuss their increase compared to other analyses of the same data. Finally, we break down the statistical and systematic contributions to the uncertainty budget.

6.1 Global fit

We fit all Cepheid and SN data simultaneously to equations (16)–(18) as described in Section 3.3. We minimize a global χ^2 function (a function of $\Theta = \{\alpha, \beta, M_\mathrm{B}, \mathcal{H}, b_\mathrm{W}, Z_\mathrm{W}, M_\mathrm{W}, \mu_{4258}, \{\Delta\mu_i\}\}$), which has contributions from the Cepheids and low-z SNe remaining after cuts (given in equations 20 and 22, respectively), and also an equivalent term to $\chi^2_{\mathrm{low}-z}$ for the eight nearby SNe:

$$\chi^2_{\mathrm{global}} = \chi^2_c + \chi^2_{\mathrm{SN}} + \chi^2_{\mathrm{nearby}} \tag{23}$$

$$\chi^2_{\mathrm{nearby}} = \left(\hat{\boldsymbol{m}}^\dagger_\mathrm{B} - \hat{\boldsymbol{m}}^\dagger_{\mathrm{B\,mod}}\right) \mathbf{C}_{m^\dagger_\mathrm{B}, n}^{-1} \left(\hat{\boldsymbol{m}}^\dagger_\mathrm{B} - \hat{\boldsymbol{m}}^\dagger_{\mathrm{B\,mod}}\right)^T . \tag{24}$$

The bolded quantities in equation (24) are vectors, over the eight nearby SNe Ia. The terms contributing to the nearby covariance matrix $\mathbf{C}_{m^\dagger_\mathrm{B}, n}$ are covariances between SALT2 quantities m_B, X_1, and C, and the diagonal intrinsic scatter $\sigma_{\mathrm{int, SN}}$.

The global simultaneous fit is 16- or 17-dimensional (without and with the LMC included as a distance anchor, respectively), and performed using MultiNest as described in Section 2.3.1. We are ultimately interested in $\mathcal{H}$, which contains the value of H_0. However to demonstrate degeneracies and correlations between parameters, we display in Figs 3 and 4 marginalized contour plots of the posterior distribution of an example fit (with $T = 2.25$, NGC 4258+LMC+MW anchor, $P < 60$ d cut Cepheid fit, and default SN cuts).[16] The former posterior distribution is marginalized over the eight $\Delta\mu_i$, while the latter is also marginalized over μ_{4258} and the SN and Cepheid parameters which are strongly constrained by initial fits: $\{\alpha, \beta, b_\mathrm{W}, Z_\mathrm{W}\}$. Fig. 3 shows a strong positive correlation between M_B and $\mathcal{H}$ as expected from their degeneracy in the low-z SN sample (equation 18), and less apparent correlations between the 'zero-point-like' parameters $\{\mathcal{H}, M_\mathrm{B}, M_\mathrm{W}, \mu_{4258}\}$. In contrast, the five other parameters $\{\alpha, \beta, b_\mathrm{W}, Z_\mathrm{W}, \mu_{4258}\}$ each are largely independent of the other parameters (Fig. 3).

We repeat the global fit for each of 18 Cepheid fits in Table 2 and six SN cuts determined in Section 5.5 from Fig. 2. Each Cepheid fit and SN cut corresponds to a subset of the total sample to use in the

global fit, and associated values of best-fitting parameters, as well as $\sigma_{\mathrm{int, C}}$ for the Cepheids. In total there are 108 fits; the analysis of these results and the variation therein follows.

6.2 Results of global fit

The best-fitting values and uncertainties of parameters in Θ are given in Table D3 for each of 108 fits. Fig. 5 displays these fits in various subspaces of the 16- or 17-dimensional space spanned by Θ, focusing on parameters $\{\alpha, \beta, b_\mathrm{W}, Z_\mathrm{W}, M_\mathrm{W}, M_\mathrm{B}, \mathcal{H}\}$. We discuss the dependencies that this figure shows (which motivate the averaged tables and figures later), then present results for the nuisance parameters and the parameters of interest: the SN Ia peak absolute magnitude M_B and (proxy for the) Hubble constant $\mathcal{H}$, which are degenerate with each other.

In the remainder of the section, we depart from the distinction we make between statistical and systematic uncertainties in Appendix C2: the uncertainties returned by MultiNest, reported in Table D3, simply the 1σ widths of the PDFs, do not distinguish between the statistical and systematic components of covariance matrices input into the fit in the likelihood. Henceforth, we refer to this uncertainty from the MultiNest fit as statistical, and the variation observed in, e.g. Fig. 5 between global fits with differing SN cuts or Cepheid fits as systematic.

6.2.1 Dependence of parameters

Fig. 5 highlights the following dependence of parameters on properties of the global fit:

(i) The Cepheid parameters $\{b_\mathrm{W}, Z_\mathrm{W}, M_\mathrm{W}\}$ depend only on the choice of Cepheid fit (carried forward from Section 4.4.2), reflecting the variation observed in Fig. 1. Thus, there is negligible scatter in values for these parameters between fits with the same Cepheid data, regardless of the SN cut (Figs 5 a and b).

(ii) Similarly, the SN parameters $\{\alpha, \beta\}$ depend most strongly on cuts, and minimally on Cepheid fit, although there is more scatter than in $\{b_\mathrm{W}, Z_\mathrm{W}\}$. On average fits without an upper period cut on the Cepheids result in slightly lower α by ~ 0.01, for each SN cut (Fig. 5c).

(iii) The Cepheid and SN zero-points M_W and M_B both depend predominantly on the Cepheid fit (Fig. 5b), reflecting the fact that the SNe Ia are calibrated on the Cepheids. While M_W depends directly on the Cepheid data (equation 16), the influence on M_B is through its interaction with M_W via the distance modulus offsets $\{\Delta\mu_i\}$ (equations 16 and 17). We note that M_W has negligible dependence on SN cut, whereas M_B varies slightly with the choice of SN cut (with a spread of ~ 0.01 within each choice of Cepheid fit).

(iv) As mentioned in Section 3.4, $\mathcal{H}$ is degenerate with M_B. Fig. 5(d) shows this degeneracy between the parameters, and that the difference $\mathcal{M} = M_\mathrm{B} - \mathcal{H}$ lies on a straight line. Within each choice of Cepheid fit, there is slight systematic dependence only on the choice of SN cut. There is no systematic difference between these parameters from fits with and without a cut on Cepheid period.

(v) $\{\Delta\mu_i\}$: the values of the distance modulus offsets from the global fit depend significantly on the Cepheid fit, as shown in Figs 6 and 7.

In summary, it is expected that the SN cuts determine parameters $\{\alpha, \beta\}$, and the Cepheid fits determine parameters $\{b_\mathrm{W}, Z_\mathrm{W}, M_\mathrm{W}\}$. However, the interaction of the 'zero-point-like' parameters is more subtle, and emerges from the simultaneous fit of the three data

---

[16] Figs 3, 4, and 9 were created with the CHAINCONSUMER package (Hinton 2016).
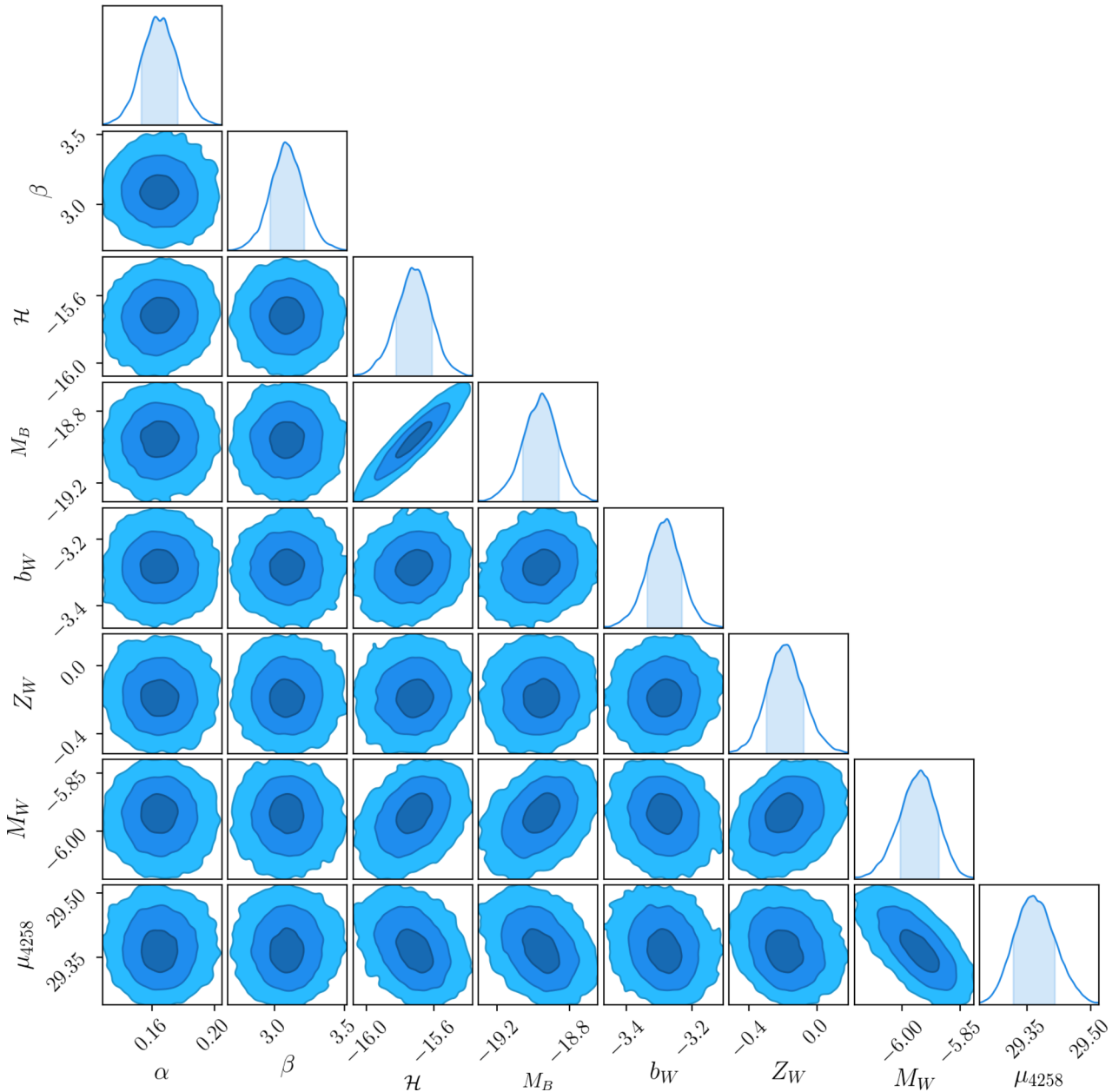
Figure 3. Constraints on parameters in Θ from an example global MultiNest fit (with $T = 2.25$, NGC 4258+LMC+MW anchor, $P < 60$ d cut Cepheid fit, and default SN cuts) marginalized over $\{\Delta\mu_i\}$. The shaded regions in the PDFs represent 1σ levels, and the 1σ, 2σ, and 3σ regions are shown in the contours. Note the strong degeneracy between $\mathcal{H}$ and M_B, and slightly weaker degeneracies between $\mathcal{H}$, M_B, μ_{4258}, and M_W. The other parameters appear uncorrelated.

samples, most obvious in Fig. 5(b). Even though the parameter M_B only appears in the SN apparent magnitudes (equations 17 and 18), it is most strongly influenced by the Cepheid data via M_W, as the two parameters are tied to their respective data sets through the distance modulus offsets $\{\Delta\mu_i\}$. Furthermore, M_B and $\mathcal{H}$ are degenerate with their difference determined by the low-z SNe. Thus, the resultant value of $\mathcal{H}$, hence H_0, is sensitive both to the choice of SN cut (via the $M_B - \mathcal{H}$ degeneracy) and to the choice of Cepheid fit (via the influence of M_W on M_B). Unsurprisingly, the most extreme values of M_B and $\mathcal{H}$ (both driven by M_W, as seen in Fig. 5b) arise from Cepheid fits anchored on only the LMC or MW (most and least negative, represented by dark purple and pink symbols, respectively). It is clear from Fig. 5(d) that the variation with Cepheid fits (anchor and rejection) is at least an order of

magnitude larger than the variation with SN cuts, even when the fits anchored on the LMC or MW only are excluded.

6.2.2 Nuisance parameter results

Tables 5 and 6 contain results for the SN and Cepheid nuisance parameters, averaged over the Cepheid fits and SN cuts, respectively. We choose to average over these aspects of the fit that have minimal effect on the parameters, as shown in Fig. 5: the SN parameters in (c) predominantly depend on shape (SN cut) and not on colour (Cepheid fit), while the Cepheid parameters in (a) depend entirely on colour and not on shape. We omit statistical uncertainties of parameters in these tables as they can be obtained from the full set
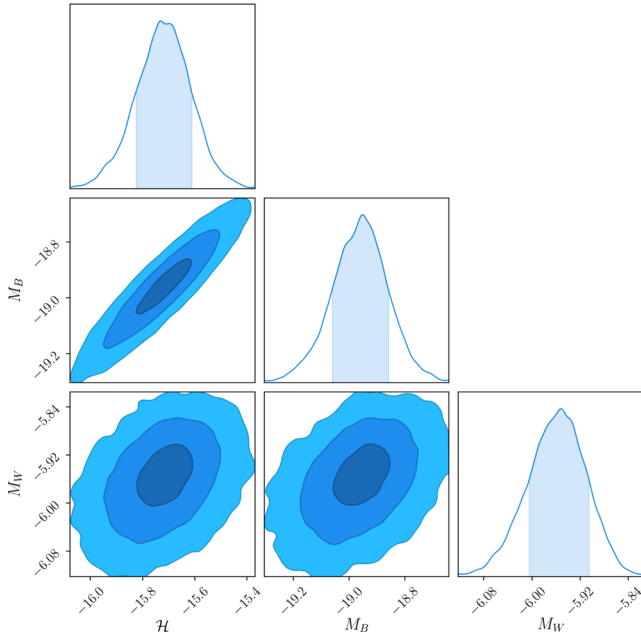
Figure 4. The same fit as Fig. 3, also marginalized over $\{\alpha, \beta, b_W, Z_W, \mu_{4258}\}$. This shows the three parameters that are the most highly correlated.

of results in Table D3. For the nuisance parameters, we select a single best fit (bolded in Table D3 and indicated in Fig. 5). This is preferable to averaging over results in Tables 5 and 6, which are asymmetric, based on different premises (e.g. different distance anchors), and include more questionable fits (e.g. those SN cuts that reject a larger fraction of the total). Thus, we use the maximal variation in these values to inform our systematic error budget, but not to influence the best fit.

Final values for the nuisance parameters are taken from the bolded reference fits, which have the default SN cut and the Cepheid fit with all three anchors, $T = 2.25$ rejection, and no cut on Cepheid period. We have chosen this fit because the results are representative and centred amongst the different choices. The Cepheid fit here also aligns with fits selected in E14 and R11. As in R11, we choose to not impose a cut on Cepheid period, and note the effects of including this cut on nuisance parameters described in Section 4.4: both b_W and Z_W are more negative with the $P < 60$ d cut, while there is no difference in M_W when all three distance anchors are used. The global SN results differ slightly from the initial results in Table 4, and we again note that the most deviant (lowest) values of α or β are where a large number of SNe have been rejected; the remaining cuts are in agreement with values derived from the default cut. In summary, the fit parameters and uncertainties from Tables 5 and 6 are:

$$\alpha = 0.165 \pm 0.010(\text{stat})^{+0.004}_{-0.005}(\text{sys})$$

$$\beta = 3.09 \pm 0.11(\text{stat})^{+0.04}_{-0.12}(\text{sys})$$

$$b_W = -3.17 \pm 0.04(\text{stat})^{+0.13}_{-0.11}(\text{sys})$$

$$Z_W = -0.11 \pm 0.09(\text{stat})^{+0.08}_{-0.10}(\text{sys})$$

$$M_W = -5.95 \pm 0.04(\text{stat})^{+0.06}_{-0.12}(\text{sys}). \qquad (25)$$

These statistical uncertainties are found from Table D3. We generally take the maximal variation measured from the reference fits in Tables 5 and 6 as the systematic uncertainty, with the following exceptions. We disregard the higher low-redshift cut (associated with a large fraction of the SNe being discarded) in estimating the

systematic uncertainty in β – see discussion in Section 5.5. For the uncertainty in Z_W, we only consider the variation over fits which include both the LMC and MW in the distance anchor: the constraints on the metallicity dependence provided by different distance anchors are inconsistent with each other, so we only consider these fits for estimating the uncertainty for the nuisance parameter Z_W alone (i.e. the other anchors are considered for estimating uncertainties on M_B and $\mathcal{H}$, in Section 6.2.3.) From Fig. 5(c), it is clear that the statistical uncertainties in the SN parameters are around double the systematic uncertainty if we disregard the higher low-redshift SN cut. The opposite is true for the Cepheid parameters, where the statistical uncertainties are dwarfed by systematic variation with differing fits. If we restrict our analysis to only Cepheid fits anchored on all three galaxies, the statistical and systematic uncertainties are comparable in size.

The systematic errors are asymmetric for most parameters, especially for β (due to the outlying $z > 0.0233$ cut) and Z_W. This can be observed in Figs 5(a)–(c), where it is evident that our reference fits do not lie centrally within the parameter subspaces. Fig. 5(b) shows that the MW as a distance anchor drives M_W up, while the LMC (and to a lesser extent NGC 4258) drives M_W down, an effect which propagates to M_B and $\mathcal{H}$ (Fig. 5d). Fits anchored on all three distance anchors lie centrally. Our Cepheid nuisance parameters remain consistent with R11 and E14 as initially found in Section 4.4.1.

We note that our best-fitting value for α is significantly higher than found in JLA (Betoule et al. (2014), table 10) and LOSS (Ganeshalingam et al. 2013), by $\sim$0.02 (around double the total uncertainty in α). This difference occurs consistently over a range of SN cuts. While the JLA analysis always determines α from the low-z sample in conjunction with a higher redshift sample, Ganeshalingam et al. (2013) find $\alpha = 0.146 \pm 0.007$ from the LOSS sample, which overlaps with ours considerably and is over a similar redshift range. Our results for β are consistent with the literature with the exception of the $z > 0.0233$ SN cut, which results in a value $\sim 1\sigma$ below the other cuts (the triangles in Fig. 5c). The impact of this cut on $\mathcal{H}$ can be seen in Fig. 5(d): the triangles (higher low-z cut) have higher $\mathcal{H}$ than the other shapes (cuts) for each colour/fill (Cepheid fit). This effect is much smaller than the differences from varying the Cepheid fit. Nevertheless, it is in agreement with the increase of H_0 with increasing low-z observed in R16, fig. 13.

The remaining nuisance parameters are the distance modulus offsets $\{\Delta\mu_i\}$, which, like all other nuisance parameters, are eventually marginalized over. Their values depend primarily on the Cepheid fits. The full table of fit values is left to Table D2 in Appendix D. The $\Delta\mu_i$ are visualized in Figs 6 and 7 with different colour/fill representing Cepheid fit. Fig. 6 gives some insight into the interplay and correlations between distance moduli of different galaxies, while Fig. 7 shows the scatter and relative values of the $\Delta\mu_i$ from different fits. The statistical uncertainties in $\Delta\mu_i$ from individual fits range from 0.05 to 0.1, and is comparable to the scatter over different fits.

6.2.3 Results for M_B and $\mathcal{H}$

We now consider the parameters M_B and $\mathcal{H}$ which, together, directly reveal H_0. The degeneracy between them is apparent in Fig. 5(d), which also shows that their primary dependence is on the Cepheid fits. Thus, in Table 7, we present the global fit results averaged over
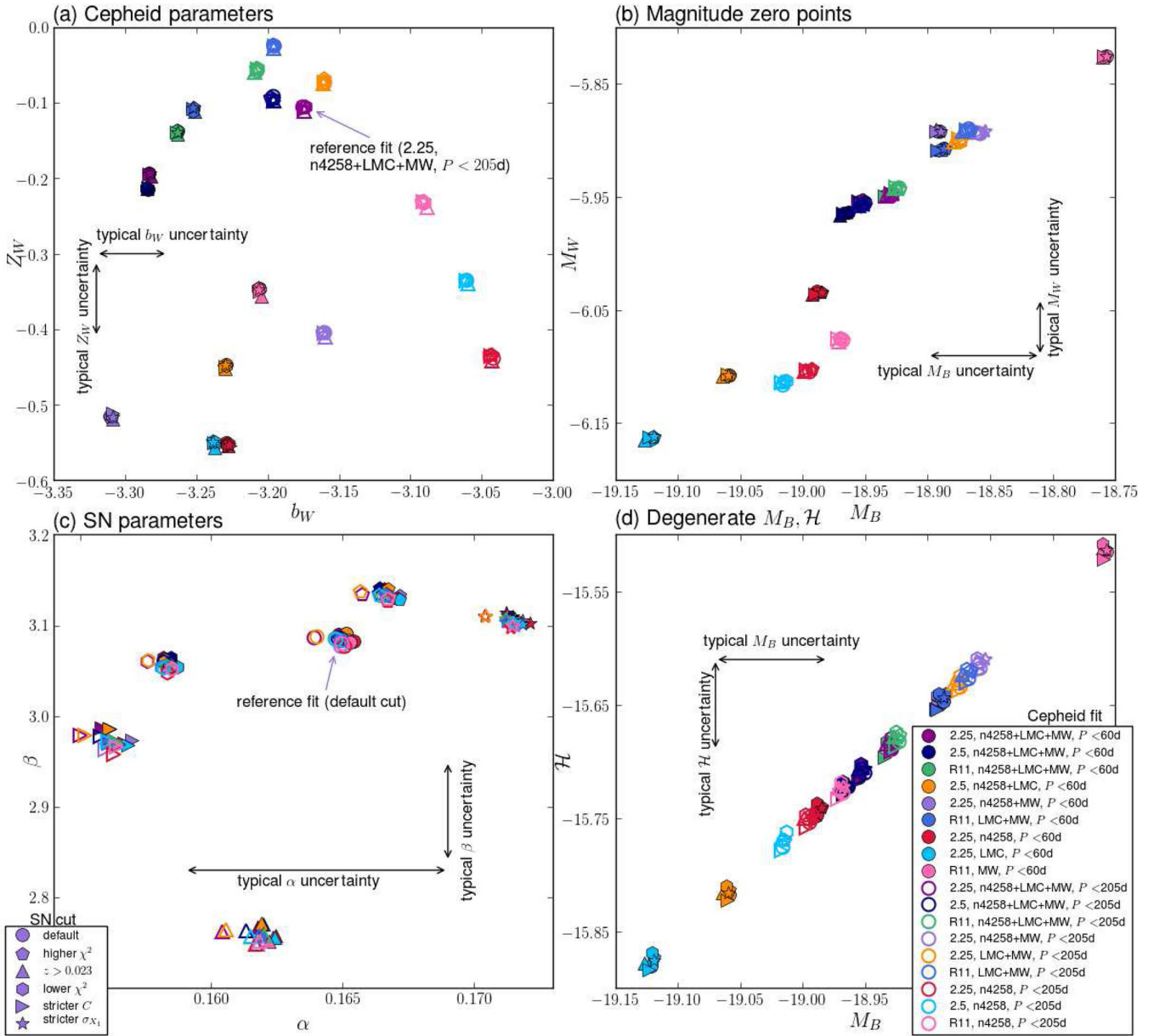
Figure 5. Results of all global fits to equations (16)–(18) simultaneously, in the (a) b_W, Z_W-, (b) M_B, M_W-, (c) α, β-, and (d) M_B, $\mathcal{H}$-planes, when assuming various choices of SN cut and Cepheid fit. As shown in the legends the different combinations of colour and fill encapsulate information on the choice of Cepheid fit as described in Section 4.4.2, while the different shapes represent difference cuts on the SNe from Section 5.5. The chosen reference fits (bolded in Tables 5 and 6) are indicated by the violet arrows in (a) and (c). The overlap of points with the same colour and fill in (a) demonstrate that the Cepheid parameters b_W, Z_W depend only on the Cepheid fit; similarly, the clusters of points with the same shape in (c) show that the SN Ia parameters α, β depend mostly on the SN cut. Subplot (b) shows that M_W and M_B both depend predominantly on the choice of Cepheid fit, with the effect more strong in M_W. A strong degeneracy between M_B and $\mathcal{H}$ is evident in (d), indicating that $\mathcal{H}$ depends primarily on the Cepheid fit, and secondarily on the SN cut. There is no systematic difference in M_W, M_B, and $\mathcal{H}$ between fits with and without an upper limit on Cepheid period.

the SN cuts.[17] Given that the fits in Table 7 anchored on all three galaxies are spread out, we average these fits rather than choose a best fit, and take the maximal variation in these fits as the systematic uncertainty. There is a slight systematic difference between fits in

---

[17] We report M_B and $\mathcal{H}$ to 3 decimal places, unlike most other parameters which have been truncated to 2 decimal places (but not rounded in the analysis). These two quantities are of particular interest, and it is desirable to retain precision in both their values and uncertainties throughout this section.
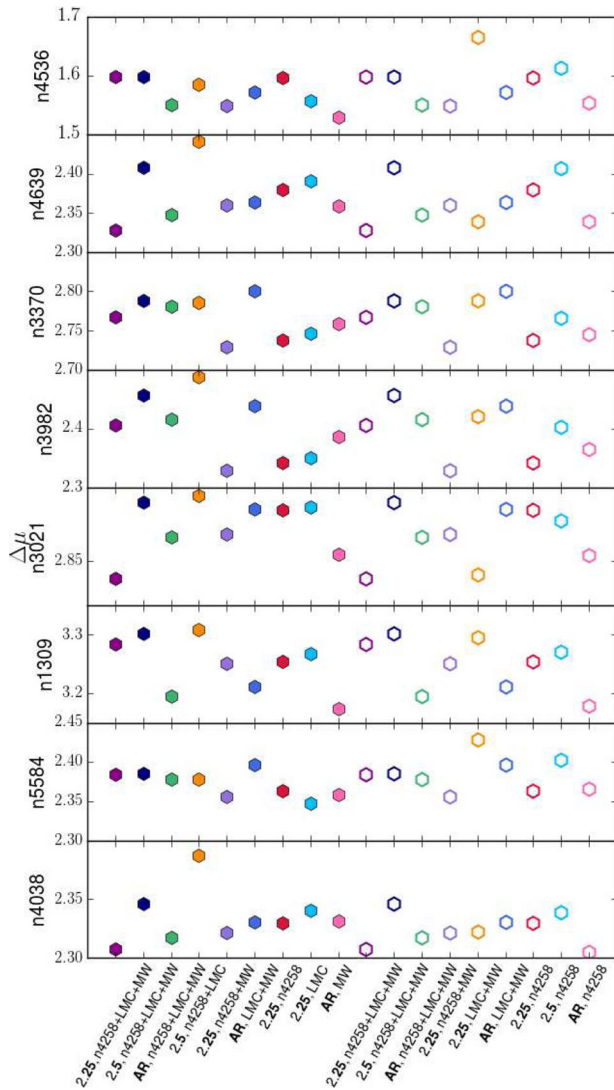
Table 7 with and without the upper period limit (on average, $\mathcal{H}$ is decreased by 0.015 mag where the $P < 60$ d cut is applied). From a theoretical standpoint, we have no reason to preference one cut over the other. Thus, our best estimates for M_B and $\mathcal{H}$ are averaged over all fits anchored on all three galaxies (including fits both with and without the upper period limit), represented by solid and empty navy, green, and dark purple markers in Figs 5–8.
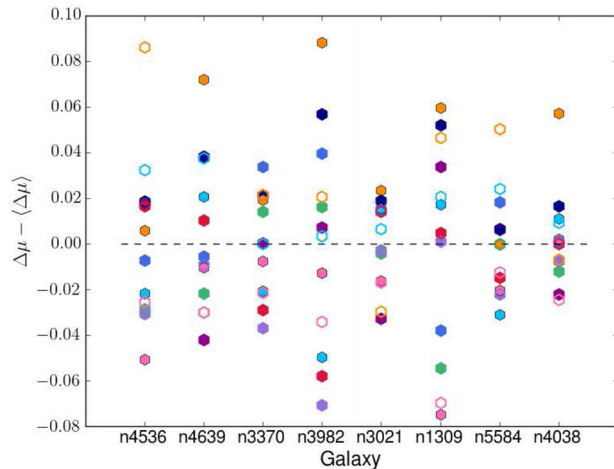
Our *best estimates* are

$$M_B = -18.943 \pm 0.088(\text{stat}) \pm 0.024(\text{sys})$$
$$\mathcal{H} = -15.698 \pm 0.093(\text{stat}) \pm 0.023(\text{sys}). \qquad (26)$$

Figure 6. Visualization of the best-fitting values for each $\Delta\mu_i$, which vary slightly with the different Cepheid fits in Section 4.4.2 (symbols shown in legends of Figs 5 and 8). Each horizontal subplot represents a different galaxy.

Figure 7. Visualization of the relative value of the $\Delta\mu_i$ with respect to the mean over all Cepheid fits for each galaxy, marked by the black dashed line. The legends in Figs 5 and 8 show the Cepheid fit (colour and fill).

Table 5. Global fit results for SN parameters α, β for each SN cut, averaged over Cepheid fits. The default rejection (bolded) detailed in Section 5.3 is chosen as our reference fit.

SN cut	α	β
Default	**0.165**	**3.09**
Higher χ^2	0.167	3.134
$z > 0.0233$	0.162	2.759
Lower χ^2	0.158	3.057
Stricter C	0.156	2.974
Stricter σ_{X_1}	0.171	3.106

Table 6. Global fit results for Cepheid parameters $\{b_W, Z_W, M_W\}$ for each Cepheid fit, averaged over SN cuts. The bolded fit ($T = 2.25$ rejection, all three anchors, and no upper cut on the period) is chosen as our reference fit.

| Rejection	Distance anchor	$P < 60d$	b_W	Z_W	M_W
2.25	All[a]	Y	−3.28	−0.19	−5.95
2.5	All	Y	−3.28	−0.21	−5.96
R11	All	Y	−3.26	−0.14	−5.95
2.5	n4258+LMC	Y	−3.23	−0.45	−6.11
2.25	n4258+MW	Y	−3.31	−0.52	−5.89
R11	LMC+MW	Y	−3.25	−0.11	−5.91
2.25	n4258	Y	−3.23	−0.55	−6.03
2.25	LMC	Y	−3.24	−0.55	−6.16
R11	MW	Y	−3.21	−0.35	−5.83
2.25	**All**	**N**	**−3.17**	**−0.11**	**−5.95**
2.5	All	N	−3.20	−0.10	−5.96
R11	All	N	−3.21	−0.06	−5.94
2.25	n4258+MW	N	−3.16	−0.41	−5.89
2.25	LMC+MW	N	−3.16	−0.07	−5.90
R11	LMC+MW	N	−3.20	−0.03	−5.89
2.25	n4258	N	−3.04	−0.44	−6.10
2.5	n4258	N	−3.06	−0.34	−6.11
R11	n4258	N	−3.09	−0.23	−6.08

Note. [a] That is n4258+LMC+MW.

Table 7. Global fit results for degenerate parameters M_B and $\mathcal{H}$, averaged over SN cuts. The bolded fit ($T = 2.25$ rejection, all three anchors, and no upper cut on the period) is chosen as our reference fit.

Rejection	Distance anchor	$P < 60d$	M_B	$\mathcal{H}$
2.25	All[a]	Y	−18.953	−15.709
2.5	All	Y	−18.967	−15.722
R11	All	Y	−18.932	−15.687
2.5	n4258+LMC	Y	−19.061	−15.816
2.25	n4258+MW	Y	−18.892	−15.647
R11	LMC+MW	Y	−18.889	−15.644
2.25	n4258	Y	−18.988	−15.743
2.25	LMC	Y	−19.122	−15.877
R11	MW	Y	−18.759	−15.514
2.25	All	N	−18.929	−15.685
2.5	All	N	−18.953	−15.708
R11	All	N	−18.924	−15.679
2.25	n4258+MW	N	−18.859	−15.614
2.25	LMC+MW	N	−18.875	−15.631
R11	LMC+MW	N	−18.868	−15.623
2.25	n4258	N	−18.996	−15.751
2.5	n4258	N	−19.015	−15.770
R11	n4258	N	−18.970	−15.725

Note. [a] That is n4258+LMC+MW.
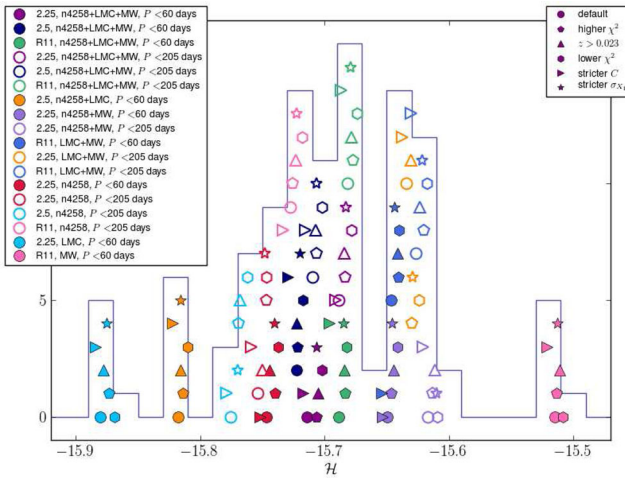
Figure 8. Histogram of best-fitting values for $\mathcal{H}$ from all global fits: essentially a histogram of Fig. 5(d) projected on to its *y*-axis. The blue line shows the binned histogram, while the individual points are plotted with their true $\mathcal{H}$ values and to reflect the distribution (i.e. they are stacked vertically for each bin). The frequency reflects the fits we chose to include in the global fit, i.e. we deliberately included more fits with all three anchors (and to a lesser extent, anchored on NGC 4258), rather than an inherent distribution. The legends are the same as in Fig. 5, and reflect the Cepheid fit (colour and fill, with solidity of markers reflecting the inclusion of a Cepheid period cut) and SN cut (shape). The fits anchored on NGC 4258 only have a much broader spread in $\mathcal{H}$, and are responsible for the lowest values. The range in values in the NGC 4258-anchored fits is much greater, extending from left-filled pink markers to top-filled navy and dark purple markers and spanning ~ 0.11 mag. In contrast, the fits anchored on all three galaxies extend from the solid navy markers to the empty green markers, spanning ~ 0.04 mag.

Here, the statistical uncertainties are found from relevant fits in Table D3, in which a representative fit is bolded (with default SN cut, $T = 2.25$ rejection, and no upper period limit). The above systematic uncertainties are given by the maximal variation in values with the combined NGC 4258+LMC+MW distance anchor. We impose this constraint on the anchor so that we can fairly assess the systematic uncertainty when all available distance information is used, and to allow better comparison with R11 and E14 who primarily report errors with all three anchors. In Section 6.3, we investigate and discuss uncertainties in $\mathcal{H}$, including converting from an absolute error in the logarithmic quantity $\mathcal{H}$ to a relative error in H_0.

We next consider fits anchored on NGC 4258 only, to estimate the uncertainty in this case, and for the sake of comparison with R11 and E14. These fits are represented by the empty turquoise and pink markers, and by all red markers in Figs 8 and 5. We average these results from Table 7 to find equation (27), as with equation (26). The systematic uncertainties are given by the maximal variation in values derived from these fits, and the statistical uncertainties are found from NGC 4258 anchored fits in Table D3, with one representative fit bolded.

$$M_{\rm B} = -18.993 \pm 0.104(\text{stat}) \pm 0.023(\text{sys})$$
$$\mathcal{H} = -15.748 \pm 0.107(\text{stat}) \pm 0.023(\text{sys}). \qquad (27)$$

The resultant value of $\mathcal{H}$ in equation (27) is 0.05 mag lower (corresponding to a 2.3 per cent decrease in H_0) compared to where all three anchors are used (equation 26). Moreover, $M_{\rm B}$ (which is largely degenerate with $\mathcal{H}$) is also 0.05 mag lower (brighter). The systematic uncertainty (i.e. the spread in values between different fits) is the same, while the statistical uncertainties are larger,

Table 8. Summary of uncertainties in $\mathcal{H}$ from Section 6.2.3 (equations 26 and 27), converted to relative errors in H_0 using equation (28), and added in quadrature in line with R11. The statistical error below are those reported by MultiNest (Table D3) and include terms (i) and (ii) described at the start of Section 6.3. The systematic error is from the variation between fit results with different choices of Cepheid fits, and secondarily SN cuts, i.e. term (iii).

Anchor	All	NGC 4258 only
$\mathcal{H}$	-15.698	-15.748
$\sigma_{\mathcal{H}}$		
Statistical	0.093	0.107
Systematic	0.023	0.023
Relative H_0 error (per cent)		
Statistical	4.3	4.9
Systematic	1.1	1.1
Total	**4.4**	**5.0**

reflective of the fact that a distance scale is anchored on a smaller set of data.

Our best estimate of the peak SN Ia brightness $M_{\rm B}$ [in equation (26), from the three-galaxy anchor] appears mildly higher (dimmer) than values reported in JLA (assuming $H_0 = 70$ km s^{-1} Mpc^{-1}), which are $M_{\rm B} = -19.05 \pm 0.02$ from all SN Ia data, or $M_{\rm B} = -19.02 \pm 0.03$ from a lower redshift subsample consisting of low-z and SDSS SNe (table 10 of Betoule et al. 2014). However, the SN-only fit in JLA cannot constrain both $M_{\rm B}$ and H_0, which are degenerate. As they have assumed a value for H_0 (while we have fitted separately using a distance ladder), our numerical values for $M_{\rm B}$ are not directly comparable, but merely reflect the influence of different values of H_0.

Returning to H_0, equation (26) corresponds to a value of $H_0 = 72.5 \pm 3.1(\text{stat}) \pm 0.77(\text{sys})$ km s^{-1} Mpc^{-1} (total uncertainty of 4.4 per cent) from the combined NGC 4258+LMC+MW anchors. If we assume the older distance $\mu_{4258} = 29.31$ in R11 (footnote 11), our best estimate increases to $H_0 = 73.8 \pm 3.2(\text{stat}) \pm 0.78(\text{sys})$. These central values agree with R11 ($H_0 = 73.8 \pm 2.4$) and E14 ($H_0 = 72.5 \pm 2.5$), which respectively assume $\mu_{4258} = 29.31$ and 29.404. Using only NGC 4258 as a distance anchor (and the new Humphreys et al. 2013 value of $\mu_{4258} = 29.404$) gives $H_0 = 70.9 \pm 3.5(\text{stat}) \pm 0.75(\text{sys})$ km s^{-1} Mpc^{-1}, which is 2.3 per cent lower than with the three anchors. The uncertainties in $\mathcal{H}$ are broken down in Section 6.3.1 and summarized in Table 8. We next discuss the uncertainties in H_0; their size informs the significance of the tension between values of the Hubble constant measured using different probes, so they are of equal interest to the values.

6.3 Uncertainties

We have emphasized the importance of quantifying and incorporating the scatter in parameters arising from varying aspects of the SN and Cepheid fits, and indeed we use this overall variation in results to gauge the systematic uncertainty in these parameters. However, we have also seen that the statistical uncertainty dominates for the SN parameters α and β (Figs 2 and 5c), as well as for $M_{\rm B}$ and $\mathcal{H}$ when only considering the systematic variation between fits with all three anchors (Fig. 5d). This dominance reflects the fact that the SN Ia samples, especially the nearby sample (i.e. in Cepheid hosts), are

Table 9. Relative contributions to the uncertainty in H_0 (i.e. the variance) from individual statistical and systematic sources uncertainties, calculated as described in Betoule et al. (2014, section 6.2).

Source of uncertainty	Relative contribution to $\sigma^2(H_0)$ (per cent)	Described in Appendix
Statistical		
Light curves	62.1	C2
SALT2 training	1.2	C2
Total statistical	**63.3**	
Systematic		
Malmquist bias	13.7	B2,C
Host galaxy	13.0	C5
Light-curve model	6.8	C
Calibration	3.1	C4
Peculiar velocities	0.04	C6
MW extinction	0.03	C3
Total systematic	**36.7**	

relatively small with large errors when compared to the Cepheids. Hence, the SNe are statistically limited, while the Cepheids are not.

For clarity, we divide the contributions to the total uncertainty in the parameters into three classes:

(i) The statistical (in the usual sense) portion of the uncertainty reported by MultiNest, which is dominated by noise in the nearby and low-z SNe.

(ii) The systematic elements of $\boldsymbol{C_\eta}$, which make up remainder of the uncertainty reported by MultiNest, listed in Table 9.

(iii) The systematic uncertainty associated with varying aspects of the fit between reasonable alternatives is dominated by the variation in the choice of Cepheid fit, as shown in Figs 5 and 8. For our final value and uncertainty of H_0, we focus on fits with all three anchors only (with some consideration of fits with only NGC 4258 as an anchor for the sake of comparison to R11 and E14). Then, in effect we are only considering the variation with the rejection algorithm and the cut on Cepheid period.

6.3.1 Uncertainties in H_0

We now address the uncertainty in the Hubble constant H_0 explicitly, using results in Section 6.2.3 (equations 26 and 27). As the quantity $\mathcal{H}$ is related to the logarithm of H_0, its absolute error informs the relative error in H_0, via

$$\frac{\sigma_{H_0}}{H_0} = \frac{\log(10)}{5}\sigma_{\mathcal{H}}. \tag{28}$$

Table 8 summarizes our calculations of the final uncertainty in H_0 from equations (26) and (27). We find using equation (28) relative errors in H_0 of 4.3 per cent statistical and 1.1 per cent systematic [corresponding to terms (i) and (ii) combined, and (iii) respectively as described at the start of Section 6.3] from all three distance anchors. From using only NGC 4258 as an anchor, these errors are 4.9 per cent statistical, 1.1 per cent systematic, and 5.0 per cent total. The final uncertainty in H_0 (the bottom row of Table 8) is the quadrature sum of the above statistical and systematic terms. Table 8 is comparable to the lower portion of table 5 of R11 (and subsequently table 7 of R16), which lists all systematic and statistical uncertainties contributing in quadrature to the uncertainty in H_0.

6.3.2 Increase in error compared to R11 and E14

Our final uncertainty in H_0 is 4.4 per cent total (4.3 per cent statistical and 1.1 per cent systematic, with the statistical term inclusive of contributions from SN Ia covariance matrices) for the NGC 4258+LMC+MW distance anchor, which is significantly larger than previously found for the same data set (by 1 per cent absolutely, or a ~20 per cent increase): R11 and E14[18] report total uncertainties of 3.3 per cent[19] and 3.4 per cent, respectively. If NGC 4258 alone is used as a distance anchor, the above errors increase to 5.0 per cent total (4.9 per cent statistical and 1.1 per cent systematic) for our fit, 4.1 per cent (4.0 per cent statistical and 1.0 per cent systematic) from R11, and 4.7 per cent total from E14. The difference between our errors and those found in E14 is smaller with the NGC 4258 anchor compared to when all three anchors are used – however, both are significantly larger than found in R11. For the remainder of Section 6.3.2, our discussion of errors pertains to fits with all three distance anchors.

Although it appears that the increase in our error lies in the statistical term (with the systematic term remaining the same), it is important to note the significant differences in how these terms are derived and defined in this work [given in points (i)–(iii) at the start of Section 6.3], compared to R11. Explicitly, the covariance matrices which quantify our SN Ia systematic terms directly contribute to the statistical errors in our global fits (i.e. increase the widths of PDFs) via the likelihood, while our systematic term contains the variation in parameters resulting from changing features of the fits. In comparison, the errors in each part of the calibration chain from the distance calibrators to the SNe Ia are separately given in R11, table 5. The total uncertainty is a quadrature sum of these individual terms, and the systematic variation described in R11, section 4.

The two major differences in our analysis which potentially contribute to the increased error are the inclusion of the SN covariance matrices, detailed in Appendix C1, and the simultaneous fit to all parameters, described in Section 3.3. As outlined above, it is not possible to make a direct comparison between contributions to our error and errors given in R11, with the aim of isolating the source of the discrepancy. However, we attempt to separate the influences of the covariance matrices and simultaneous fit, replicating the quadrature sum in R11 as closely as we can below.

First, we isolate the effect of the SN covariance matrices alone on the size of uncertainties, by considering the error in the intercept of the SN Ia m–z relation: this is $\mathcal{M}$ determined from our SN-only fit (Table 4 in Section 5.4), and is equivalent to $5a_V = 3.485 \pm 0.010$ in R11. Our error in $\mathcal{M}$ is ~0.036, over three times larger than in R11. This error is roughly halved to 0.019 if we only consider the strictly statistical covariance matrix, i.e. $\mathbf{C_{stat}}$ in equation (40).[20] For the same SN data, our statistical-only error exceeds the total error in R11. Including the SN Ia systematic covariance matrices doubles the error again. We infer that the increase in error in this analysis compared to R11 is attributable to both the covariance matrix method of accounting for correlated SN Ia uncertainties,

---

[18] E14 adopts the error in R11 for the SN Ia-side of the analysis.

[19] The errors reported in table 5 of R11 are: 2.9 per cent statistical, 1.0 per cent systematic, and 3.1 per cent total. However, the final error given with all three distance anchors conservatively includes the larger statistical error associated with using two distance anchors instead of three, resulting in a total of 3.3 per cent.

[20] Neglecting the uncertainty from the finiteness of the SALT2 training sample reduces the error slightly to 0.017, which reflects the statistical error in the observed SNe Ia only (i.e. the tridiagonal matrix $\mathbf{C_{stat,diag}}$).

and to the individual systematic covariance matrices this method comprises.

Next, we attempt to replicate the quadrature summation of terms in R11, table 5 (most of which unfortunately do not have equivalent terms in our analysis) using projected uncertainties from our global fit. It is important to note that this comparison is not directly equivalent, because we are marginalizing simultaneously over all nuisance parameters. With this caveat, we break down the uncertainty in the overall value of H_0 into three components: the uncertainties in the distance anchor, in the calibration of the SN Ia absolute magnitude M_B via Cepheids, and in the measurement of the local expansion rate via SNe Ia (given in the intercept $\mathcal{M}$).[21] These can be determined separately from three disjoint data sets, as follows. The anchor distance is constrained by external data: the megamaser distance to NGC 4258 has a 0.066 mag uncertainty, corresponding to 3.0 per cent in H_0. Only the low-z SNe Ia are used to constrain $\mathcal{M}$ (or $5a_V$), with a 0.036 mag or 1.7 per cent uncertainty. The calibration transfer from the Cepheids to the SNe Ia occurs in the simultaneous fit of the nearby SN and Cepheid data[22] to equations (16) and (17). The resultant uncertainty in M_B is 0.103 mag (with only the NGC 4258 anchor) and incorporates both the uncertainty in the SN Ia-Cepheid calibration and the uncertainty in the distance anchor; thus the former is 0.079 mag or 3.6 per cent in H_0.[23] In quadrature, these three terms sum to 5.0 per cent in H_0 using the NGC 4258 anchor, and 4.3 per cent with all three anchors. This decomposition, whilst approximate, indicates that a quadrature sum of uncertainties in independent components results in similar uncertainties to our simultaneous fit. Thus, the simultaneous fit does not by itself result in the increase in statistical error.

6.3.3 Relative size of SN Ia uncertainties

We now examine the breakdown of uncertainties contributing to the statistical error, which include the multiple statistical and systematic uncertainties in SN Ia parameters making up $\mathbf{C}_\eta$ as constructed in Appendix C.

To visually assess the impact on confidence contours, we compare results from MultiNest with different covariance matrix inputs. For an example global fit (with Cepheid fit $T = 2.5$, NGC 4258 anchor, no priors, and default SN cuts), we test each systematic, and compare their results from MultiNest. The full expression for the covariance matrix $\mathbf{C}_\eta$ for observed SN Ia quantities is described in Appendix C1. As entries of $\mathbf{C}_\eta$ in MultiNest, we try the following: only the statistical contribution $\mathbf{C}_{\mathbf{stat}}$ (described in Appendix C2), each single systematic term added to $\mathbf{C}_{\mathbf{stat}}$, and all systematics added, i.e. $\mathbf{C}_{\mathbf{stat}} + \mathbf{C}_{\mathbf{sys}}$ (the default for all global fits). The confidence contours with statistical uncertainties only and with all systematics are easily distinguishable in Fig. 9, but the contours with individual systematics are not. Thus, for clarity, we only show in Fig. 9, the systematic term from the uncertainty in host mass correction corrections [$\mathbf{C}_{\mathbf{host}}$ in equation (40), described in Appendix C5], in addition to $\mathbf{C}_{\mathbf{stat}}$ and $\mathbf{C}_{\mathbf{stat}} + \mathbf{C}_{\mathbf{sys}}$. The difference between the contours is slight, indicating that the uncertainties in the parameters only increase slightly
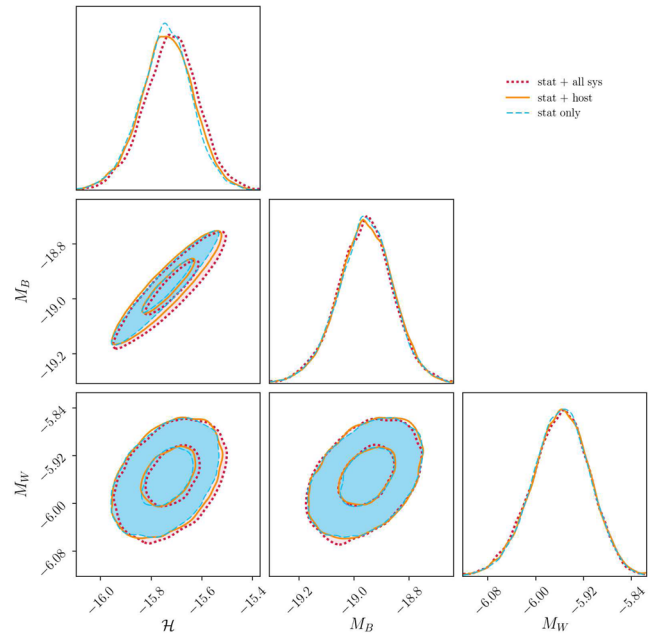
Figure 9. Constraints on parameters $\mathcal{H}$, M_B, and M_W from an example global MultiNest fit (with Cepheid fit $T = 2.5$, NGC 4258 anchor, no priors, and default SN cuts) with partial and full contributions to the full SN Ia covariance matrix. Confidence contours are shown with the statistical contribution $\mathbf{C}_{\mathbf{stat}}$ only (turquoise filled), with one systematic term (the host mass correction) added i.e. $\mathbf{C}_{\mathbf{stat}} + \mathbf{C}_{\mathbf{host}}$ (orange solid line), and with all SN Ia systematics, i.e. $\mathbf{C}_{\mathbf{stat}} + \mathbf{C}_{\mathbf{sys}}$ (red dashed). The inclusion of systematic terms only increases the widths of contours marginally relative to the $\mathbf{C}_{\mathbf{stat}}$-only (turquoise) contours, reflecting that the statistical contribution dominates the uncertainty in the parameters.

when covariance matrices for different systematics are added to the statistical term $\mathbf{C}_{\mathbf{stat}}$.

Following the method in JLA (Betoule et al. 2014, section 6.2), we quantify the relative contributions, replacing the parameters $\{\Omega_M, w, \alpha, \beta, M_B, \Delta M\}$ with our parameters $\{H_0, M_B, \alpha, \beta\}$ (the only parameters in Θ which can be influenced by the low-z SN Ia covariance matrices). The breakdown of relative contributions to the variance in H_0 from each term (the purely statistical term $\mathbf{C}_{\mathbf{stat}}$, and each systematic) are reported in Table 9. We emphasize that each of these numbers represents a proportion of the uncertainty [terms (i) and (ii) in Section 6.3 combined] from the systematic or statistical term in question alone, rather than reflecting an uncertainty in H_0.

From Table 9 and Fig. 9, it is clear that $\mathbf{C}_{\mathbf{stat}}$ is the largest component of $\mathbf{C}_\eta$. Even though the contributions to $\mathbf{C}_\eta$ from SN systematics are included in the statistical uncertainty, all of these systematics together are smaller than the SN statistical uncertainties: the relative contributions to the variance in H_0 are dominated by $\mathbf{C}_{\mathbf{stat,diag}}$ (Table 9), and the contours with and without systematic covariance matrices added to $\mathbf{C}_{\mathbf{stat}}$ in Fig. 9 are similar to each other. Of the systematic terms (Appendices C3–C6), the most significant in their impact on H_0 are from uncertainties in the Malmquist bias correction (including the selection function) and the host mass correction (Appendices B2 and C5), followed by the uncertainty in light-curve model. While JLA had found the photometric calibration (Appendix C4), especially from low-z SNe, to be the dominant uncertainty for Ω_M and w, its effect on H_0 is decidedly smaller. It is interesting to note that despite conservative estimates of both the uncertainties in MW extinction and peculiar velocity

---

[21] This decomposition essentially follows equation (4) of R11.

[22] For the uncertainty in M_B to be independent of the error in $\mathcal{M}$, only these data can be included.

[23] The same calculation with all three anchors results in the same number. In the setup of R11, equation (4), this SN Ia-Cepheid calibration uncertainty is the error in $m_{v,4258}^0$, which is equivalent to $M_B + \mu_{4258}$.

correction (Appendices C3 and C6), their effects on the error in H_0 are negligible.

7 CONCLUSIONS AND FUTURE WORK

Our independent analysis of the Riess et al. (2011) data complements the R11 and E14 analyses in understanding the local measurement of the Hubble constant from SNe Ia. This work occupies the unique position of combining the precise Cepheid calibration of nearby SNe Ia (R11) with the sophisticated, thorough treatment of SN light curves and systematics within a SALT2 framework (Betoule et al. 2014). In the context of the present tension in H_0, we present the first blinded SN Ia-based determination of H_0, eliminating confirmation and other biases. This work is intentionally applied to the well understood historical work of R11 and E14, as a proof of concept. It is our intent to extend this analysis to the sample of Riess et al. (2016).

Our best estimate from R11 data is $H_0 = 72.5 \pm 3.1$(stat) ± 0.77(sys) km s^{-1} Mpc^{-1} using a three-galaxy (NGC 4258+LMC+MW) anchor. The central value is in excellent agreement with both R11 (after correcting for the lower value of μ_{4258} adopted – see footnote 11) and the E14 re-analysis. Our above value and uncertainty imply tension with the *Planck* value at $\sim 1.5\sigma$ significance, which is smaller than found in previous analyses of the R11 data, due to our increased uncertainties. However, our blinded affirmation of the central value in R11 signifies that the discrepancy between SN Ia- and CMB-derived values of the Hubble constant continues to exist. While this discrepancy is less significant in our analysis than in the original analysis of R11 data, it has potential to be magnified by the improved data set in R16 (which has smaller statistical uncertainties compared to R11), and hence remains of interest. It is thus necessary to apply the techniques in this paper to the R16 data, in order to make a contemporary assessment of the significance of the tension in the Hubble constant.

Incidentally, we find a higher stretch coefficient $\alpha = 0.165 \pm 0.010$ for our low-z SNe compared to LOSS (which find $\alpha = 0.147 \pm 0.007$ over a similar redshift range) and JLA. This discrepancy at $\sim 2\sigma$ is surprising, and prompts further investigation. While our SN Ia zero-point $M_B = -18.94 \pm 0.09$ appears higher than in JLA, this difference arises because the parameters are degenerate using SNe only: the JLA analysis assumes $H_0 = 70$ km s^{-1} Mpc^{-1}, whereas we have used a distance ladder to constrain both H_0 and M_B.

We find a larger relative uncertainty in H_0 (4.4 per cent total) compared to R11 and E14 analyses of the same data (3.3 per cent and 3.4 per cent total, respectively), based on the NGC 4258+LMC+MW distance scale. The difference appears in the statistical error; our systematic term is similar to that in R11 (1.1 per cent and 1.0 per cent, respectively), with the caveat that the separation of our total uncertainty into statistical and systematic components is not directly comparable to R11, as described in Section 6.3.2. Our larger error primarily arises from our use of covariance matrices to estimate SN Ia systematic uncertainties. Other significant differences in our analysis, which potentially contribute to the increased uncertainty, are our simultaneous fit of all three sets of data, allowing all parameters to interact, and our use of variation in results to quantify systematic error. These distinctions are in our view justified and desirable. Given the increase in uncertainty they produce compared to previous works, they are important to consider in future analyses.

As found in R11, our results are limited by statistics in the SN samples. Steps to reduce this statistical uncertainty have been implemented in R16, namely increasing the number of nearby galaxies to 18 and improving the SN Ia photometry, to reduce the total uncertainty to 2.4 per cent. We envisage a similar relative increase in precision when the techniques in this work are applied to the same data set. R16 also includes important changes to data analysis of the Cepheids. Other contributions to our error budget are the systematic uncertainty, which is dominated by the variation in the different Cepheid fits, and the SN Ia systematic terms in $\mathbf{C}_\eta$, the largest of which are $\mathbf{C}_{\text{bias}}$ and $\mathbf{C}_{\text{host}}$.

Foremost, we find that both the use of covariance matrices and the simultaneous fit of data from different rungs of a distance ladder will be important in future analyses in order to wholly account for uncertainties. Furthermore, our findings recommend more sophisticated techniques for quantifying host galaxy dependence of SN Ia magnitudes, and modelling of Malmquist bias – both of which have the potential to diminish the systematic error in H_0. These techniques are continually improved in SN analyses, particularly in the pursuit of more precise measurements of dark energy, for example in the Dark Energy Survey (Dark Energy Survey Collaboration et al. 2016). Meanwhile a uniform, non-targeted low-z sample (e.g. the SkyMapper Transient Survey; Scalzo et al. 2017, or the Pan-STARRS1 Survey; Rest et al. 2014) will simplify photometric calibration and the selection function, reducing associated uncertainties, and will avoid peculiar velocity biases from coherent flows. Adopting these changes will benefit future SN Ia-based H_0 measurements.

REFERENCES

Bennett C. L., Larson D., Weiland J. L., Hinshaw G., 2014, ApJ, 794, 135
Bernal J. L., Verde L., Riess A. G., 2016, J. Cosmol. Astropart. Phys., 10, 019
Bessell M. S., 1990, PASP, 102, 1181
Betoule M. et al., 2013, A&A, 552, A124
Betoule M. et al., 2014, A&A, 568, A22
Bird J. C., Stanek K. Z., Prieto J. L., 2009, ApJ, 695, 874

Bonvin V. et al., 2017, MNRAS, 465, 4914
Branchini E. et al., 1999, MNRAS, 308, 1
Buchner J. et al., 2014, A&A, 564, A125
Buta R. J., Turner A., 1983, PASP, 95, 72
Calcino J., Davis T., 2017, J. Cosmol. Astropart. Phys., 1, 038
Cardona W., Kunz M., Pettorino V., 2017, J. Cosmol. Astropart. Phys., 3, 056
Carrick J., Turnbull S. J., Lavaux G., Hudson M. J., 2015, MNRAS, 450, 317
Carroll S. M., Press W. H., Turner E. L., 1992, ARA&A, 30, 499
Childress M. et al., 2013, ApJ, 770, 108
Conley A. et al., 2011, ApJS, 192, 1
Contreras C. et al., 2010, AJ, 139, 519
Croft R. A. C., Dailey M., 2011, preprint (arXiv:1112.3108)
Dark Energy Survey Collaboration et al., 2016, MNRAS, 460, 1270
Davis T. M., Parkinson D., 2016, preprint (arXiv:1610.09452)
Davis T. M. et al., 2011, ApJ, 741, 67
Di Valentino E., Melchiorri A., Silk J., 2016, Phys. Lett. B, 761, 242
Dvorkin C., Wyman M., Rudd D. H., Hu W., 2014, Phys. Rev. D, 90, 083503
Efstathiou G., 2014, MNRAS, 440, 1138 (E14)
Eisenstein D. J. et al., 2005, ApJ, 633, 560
Feroz F., Hobson M. P., 2008, MNRAS, 384, 449
Feroz F., Hobson M. P., Bridges M., 2009, MNRAS, 398, 1601
Feroz F., Hobson M. P., Cameron E., Pettitt A. N., 2013, preprint (arXiv:1306.2144)
Foreman-Mackey D., Hogg D. W., Lang D., Goodman J., 2013, PASP, 125, 306
Freedman W. L., Madore B. F., 2010, ARA&A, 48, 673
Freedman W. L., Madore B. F., 2011, ApJ, 734, 46
Freedman W. L. et al., 2011, AJ, 142, 192
Friedmann A., 1922, Z. Phys., 10, 377
Ganeshalingam M. et al., 2010, ApJS, 190, 418
Ganeshalingam M., Li W., Filippenko A. V., 2013, MNRAS, 433, 2240
Guy J., Astier P., Nobili S., Regnault N., Pain R., 2005, A&A, 443, 781
Guy J. et al., 2007, A&A, 466, 11
Guy J. et al., 2010, A&A, 523, A7
Hamuy M., Phillips M. M., Suntzeff N. B., Schommer R. A., Maza J., Aviles R., 1996, AJ, 112, 2391
Hicken M. et al., 2009a, ApJ, 700, 331
Hicken M., Wood-Vasey W. M., Blondin S., Challis P., Jha S., Kelly P. L., Rest A., Kirshner R. P., 2009b, ApJ, 700, 1097
Hicken M. et al., 2012, ApJS, 200, 12
Hinton S., 2016, JOSS, 1, 4
Hubble E., 1929, Proc. Natl. Acad. Sci., 15, 168
Hudson M. J., Smith R. J., Lucey J. R., Branchini E., 2004, MNRAS, 352, 61
Hui L., Greene P. B., 2006, Phys. Rev. D, 73, 123526
Humphreys E. M. L., Reid M. J., Moran J. M., Greenhill L. J., Argon A. L., 2013, ApJ, 775, 13
Jennings E., Wolf R., Sako M., 2016, preprint (arXiv:1611.03087)
Jha S. et al., 2006, AJ, 131, 527
Jha S., Riess A. G., Kirshner R. P., 2007, ApJ, 659, 122
Jones D. O., Riess A. G., Scolnic D. M., 2015, ApJ, 812, 31
Kelly P. L., Hicken M., Burke D. L., Mandel K. S., Kirshner R. P., 2010, ApJ, 715, 743
Kennicutt R. C., Jr, et al., 1998, ApJ, 498, 181
Kessler R. et al., 2009, PASP, 121, 1028
Lampeitl H. et al., 2010, ApJ, 722, 566
Law N. M. et al., 2009, PASP, 121, 1395
Le Borgne D., Rocca-Volmerange B., 2002, A&A, 386, 446
Le Borgne D., Rocca-Volmerange B., 2010, Astrophysics Source Code Library, record ascl:1011.003
Leavitt H. S., 1908, Ann. Harvard Coll. Observ., 60, 87
Leavitt H. S., Pickering E. C., 1912, Harvard Coll. Observ. Circ., 173, 1

Leistedt B., Peiris H. V., Verde L., 2014, Phys. Rev. Lett., 113, 041301
Lemaître G., 1927, Ann. Soc. Sci. Brux., 47, 49
Lira P. et al., 1998, AJ, 115, 234
Maccoun R., Perlmutter S., 2015, Nature, 526, 187
Macri L. M., Stanek K. Z., Bersier D., Greenhill L. J., Reid M. J., 2006, ApJ, 652, 1133
Madore B. F., 1982, ApJ, 253, 575
March M. C., Trotta R., Berkes P., Starkman G. D., Vaudrevange P. M., 2011, MNRAS, 418, 2308
Mosher J. et al., 2014, ApJ, 793, 16
Neill J. D. et al., 2009, ApJ, 707, 1449
Peebles P. J. E., 1993, Principles of Physical Cosmology. Princeton Univ. Press, Princeton, NJ
Perlmutter S. et al., 1999, ApJ, 517, 565
Persson S. E., Madore B. F., Krzemiński W., Freedman W. L., Roth M., Murphy D. C., 2004, AJ, 128, 2239
Phillips M. M., 1993, ApJ, 413, L105
Pietrzyński G. et al., 2013, Nature, 495, 76
Pike R. W., Hudson M. J., 2005, ApJ, 635, 11
Planck Collaboration XVI, 2014, A&A, 571, A16
Planck Collaboration XIII, 2016, A&A, 594, A13
Rest A. et al., 2014, ApJ, 795, 44
Riess A. G., Press W. H., Kirshner R. P., 1996, ApJ, 473, 88
Riess A. G. et al., 1998, AJ, 116, 1009
Riess A. G. et al., 2005, ApJ, 627, 579
Riess A. G. et al., 2009a, ApJS, 183, 109
Riess A. G. et al., 2009b, ApJ, 699, 539
Riess A. G. et al., 2011, ApJ, 730, 119 (R11)
Riess A. G. et al., 2012, ApJ, 752, 76
Riess A. G. et al., 2016, ApJ, 826, 56 (R16)
Rigault M. et al., 2013, A&A, 560, A66
Rigault M. et al., 2015, ApJ, 802, 20
Rubin D. et al., 2015, ApJ, 813, 137
Sakai S., Ferrarese L., Kennicutt Jr R. C., Saha A., 2004, ApJ, 608, 42
Sako M. et al., 2014, ApJS, preprint (arXiv:1401.3317)
Scalzo R. et al., 2017, PASA, 34, 30
Schlegel D. J., Finkbeiner D. P., Davis M., 1998, ApJ, 500, 525
Schmidt B. P. et al., 1998, ApJ, 507, 46
Scolnic D., Kessler R., 2016, ApJ, 822, L35
Scowcroft V., Bersier D., Mould J. R., Wood P. R., 2009, MNRAS, 396, 1287
Scowcroft V., Freedman W. L., Madore B. F., Monson A. J., Persson S. E., Seibert M., Rigby J. R., Sturch L., 2011, ApJ, 743, 76
Scrimgeour M. I. et al., 2016, MNRAS, 455, 386
Sebo K. M. et al., 2002, ApJS, 142, 71
Shariff H., Jiao X., Trotta R., van Dyk D. A., 2016, ApJ, 827, 1
Silverman J. M. et al., 2012, MNRAS, 425, 1789
Skilling J., 2004, in Fischer R., Preuss R., Toussaint U. V., eds, AIP Conf. Ser. Vol. 735, Bayesian Inference and Maximum Entropy Methods in Science and Engineering. Am. Inst. Phys., Melville, NY, p. 395
Smith M. et al., 2012, ApJ, 755, 61
Spergel D. N., Flauger R., Hložek R., 2015, Phys. Rev. D, 91, 023518
Springob C. M. et al., 2014, MNRAS, 445, 2677
Sullivan M. et al., 2006, ApJ, 648, 868
Sullivan M. et al., 2010, MNRAS, 406, 782
Sullivan M. et al., 2011, ApJ, 737, 102
Suyu S. H. et al., 2017, MNRAS, 468, 2590
van den Bergh S., 1975, Phys. Bull., 9, 509
van Leeuwen F., Feast M. W., Whitelock P. A., Laney C. D., 2007, MNRAS, 379, 723
Walker E. S. et al., 2015, ApJS, 219, 13
Wang L., Steinhardt P. J., 1998, ApJ, 508, 483
Weinberg D. H., Mortonson M. J., Eisenstein D. J., Hirata C., Riess A. G., Rozo E., 2013, Phys. Rep., 530, 87
Wyman M., Rudd D. H., Vanderveld R. A., Hu W., 2014, Phys. Rev. Lett., 112, 051302

APPENDIX A: DEPENDENCE OF CEPHEID-ONLY FIT

A1 Outlier rejection

We perform fits in two ways: either assuming the outlier rejection in Riess et al. (2011), or following the rejection method in Efstathiou (2014). The R11 algorithm rejects Cepheids from each galaxy (rather than from the global fit), based on their deviation from the best Leavitt law fit. This rejection does not take into account the size of the Cepheid uncertainties, so that points with small residuals but large uncertainties are selectively accepted (E14, section 3.1). Consequently, a large fraction of the total number of Cepheids is rejected, including a set of subluminous low-metallicity Cepheids (later corrected in R16, as discussed in Appendix A4). Moreover, the intrinsic scatter is overestimated, resulting in a low reduced χ^2.

These limitations in the R11 rejection are addressed in the upgraded algorithm in E14, which rejects a Cepheid from the global fit if its magnitude deviates from the global fit by more than the quantity $T\sqrt{m_{\mathrm{W,err}}^2 + \sigma_{\mathrm{int,C}}^2}$ for a threshold T (set to 2.25 or 2.5), where $m_{\mathrm{W,err}}$ and $\sigma_{\mathrm{int,C}}$ are the uncertainty in the individual Cepheid's measurement and the intrinsic scatter $\sigma_{\mathrm{int,C}}$, respectively. This process is iterative, with $\sigma_{\mathrm{int,C}}$ recalculated at each step (such that χ_c^2/d.o.f. $\sim$1) with increments of 0.1, where the sum in χ_c^2 is always over only the Cepheids in NGC 4258 and SN hosts (i.e. not the LMC or MW). The rejection at each iteration is based on the best fit determined in the previous iteration, i.e. the mean and 1σ uncertainty of the posterior distribution.

Initially $\sigma_{\mathrm{int,C}}$ is set to 0.3. Then in each iteration we perform the following steps:

(i) perform a MultiNest fit to all remaining Cepheids, to find marginalized posterior distributions;
(ii) find and remove outliers based on these parameters;
(iii) compute the new $\sigma_{\mathrm{int,C}}$ for these parameters and the updated Cepheid sample.

These steps are repeated until convergence, i.e. until no Cepheids are rejected in the second step.

The variation in fit results from different outlier rejection is presented in Fig. 1 and Section 4.4. In general, the R11 rejection results in less negative values of both b_{W} and Z_{W}, attributable to the aforementioned subluminous and low-metallicity subsample that it rejects.

The fit is forced to be good for all three rejection algorithms: $\sigma_{\mathrm{int,C}}$ is engineered to result in χ^2/d.o.f.$\sim$1. Thus, the algorithms cannot be compared statistically; the outlier rejection method has the drawback of not allowing the uncertainty on $\sigma_{\mathrm{int,C}}$ to be estimated, and the related consequence that we (by construction) cannot assess goodness of fit. Alternative statistical methods used in recent SN Ia analysis can surpass these limitations, including Bayesian hierarchical models (March et al. 2011; Shariff et al. 2016), the alternate Bayesian framework in Rubin et al. (2015), and Approximate Bayesian Computation (Jennings, Wolf & Sako 2016). Notably, these have been applied to determining H_0 from the R11 and R16 data sets in Cardona et al. (2017).

A2 Distance anchors

Our equations in Section 3 assume NGC 4258 is the only distance calibrator. We can generalize these equations to allow for combinations of the three anchor galaxies in R11, adding Cepheids in the LMC and MW (data described in Section 4.1). As these additional Cepheids do not have metallicity measurements, we adopt the mean values from E14 of $12 + \log_{10}[\mathrm{O/H}]$ of 8.5 and 8.9 for LMC and MW Cepheids, respectively. Here, we test the dependence of the Cepheid parameters on the distance anchor. For Cepheids in the LMC and MW, the Leavitt law (equation 13) takes the forms:

$$m_{\mathrm{W,LMC}j} = b_{\mathrm{W}}(\log_{10} P_j - 1) - 0.4Z_{\mathrm{W}} + M_{\mathrm{W}} + \mu_{\mathrm{LMC}} \qquad (A1)$$

$$m_{\mathrm{W,MW}j} = b_{\mathrm{W}}(\log_{10} P_j - 1) + M_{\mathrm{W}}. \qquad (A2)$$

We consider combinations of NGC 4258, LMC, and MW (seven in total) as distance calibrators. If NGC 4258 is not included, then no prior for μ_{4258} is imposed in MultiNest. However, the likelihood $\mathcal{L}$ in equation (10) still depends on μ_{4258}, which is indirectly constrained through the other anchors and M_{W}, and hence remains a fit parameter in Θ. If the LMC is used as an anchor then it is necessary to include μ_{LMC} as a parameter in Θ; this always has a (Gaussian) prior set to reflect the Pietrzyński et al. (2013) measurement from eclipsing binaries of $\mu_{\mathrm{LMC}} = 18.494 \pm 0.049$. The likelihood $\mathcal{L}$ is affected as a term χ_{LMC}^2 (equation A3) is added to equation (20); similarly if the MW is used as an anchor then χ_{MW}^2 (equation A4) is added. We assume $\sigma_{\mathrm{int,C}} = 0.113$ and 0.1 for the LMC and MW, respectively, following E14.

$$\chi_{\mathrm{LMC}}^2 = \sum_j \frac{(\hat{m}_{\mathrm{W,LMC}j} - m_{\mathrm{W,LMC}j,\mathrm{mod}})^2}{\hat{m}_{\mathrm{LMC,err}j}^2 + \sigma_{\mathrm{int,C}}^2} \qquad (A3)$$

$$\chi_{\mathrm{MW}}^2 = \sum_j \frac{(\hat{m}_{\mathrm{W,MW}j} - m_{\mathrm{W,MW}j,\mathrm{mod}})^2}{\hat{m}_{\mathrm{MW,err}j}^2 + \sigma_{\mathrm{int,C}}^2}. \qquad (A4)$$

A modification to the above is necessary if both the LMC and MW are used as distance anchors, to account for the calibration uncertainty between ground-based and *HST* photometries. We do this using the covariance matrix $\mathbf{C}_{\mathrm{LMC+MW}ij} = (\hat{m}_{\mathrm{W}i}^2 + \sigma_{\mathrm{int,C}}^2)\delta_{ij} + \sigma_{\mathrm{cal}}^2$ with $\sigma_{\mathrm{cal}} = 0.04$ (R11). Instead of $\chi_{\mathrm{LMC}}^2 + \chi_{\mathrm{MW}}^2$, we add the term

$$\chi_{\mathrm{LMC+MW}}^2 = (\hat{\boldsymbol{m}}_{\mathbf{W,MW}} - \boldsymbol{m}_{\mathbf{W,MW,mod}})\mathbf{C}_{\boldsymbol{LMC+MW}}^{-1}$$
$$(\hat{\boldsymbol{m}}_{\mathbf{W,MW}} - \boldsymbol{m}_{\mathbf{W,MW,mod}})^T \qquad (A5)$$

to the χ_c^2 term going into $\mathcal{L}$. Here, bolded quantities represent vectors over all LMC and MW Cepheids.

The results of varying the distance anchor are discussed in Section 4.4. Briefly, the inclusion of both the LMC and MW anchors constrains both b_{W} and Z_{W} more tightly.

A3 Longer period Cepheids

The data include Cepheids with period ranging from $\sim$10 d, to over 200 d, and Cepheids of all periods are included in Leavitt law fits in R11 (except for those Cepheids marked 'low P' in R11, table 2). Bird, Stanek & Prieto (2009) examine longer period ($P > 80$ d) Cepheids and find that these Cepheids obey a flatter Leavitt law, with a less negative period dependence b_{W}. Accordingly, recent studies of the Leavitt law (e.g. Freedman et al. 2011; Scowcroft et al. 2011) have excluded Cepheids with period greater than 60 d. Similarly, E14 in their re-analysis of the R11 data have imposed the same upper limit on Cepheid period because of the observed change in slope. It is pragmatic to follow these examples in only using Cepheids over a period range where the slope remains constant; however, it is also useful the full range of periods to accommodate the change in slope

and for the sake of comparison with R11. Rather than making an argument to include the $P < 60$ d cut or not, we perform fits with and without an upper limit on the period.

E14 reasons that while including longer period Cepheids decreases the magnitude of the Leavitt law slope b_W, there is little impact on H_0 (Efstathiou 2014, appendix A), so they only include $P < 60$ d Cepheids in their fits. Our priors on b_W differ slightly from E14 (discussed in Appendix A4), and we are interested in the variation of Cepheid parameters with the choice of period cut (as with distance anchor and rejection algorithm in previous sections), so we test the dependence of fit results on the inclusion of an upper limit on period. Results of including longer period Cepheids are lesser dependence on Cepheid slope and metallicity dependence (less negative b_W and Z_W), as described in Section 4.4.

A4 Slope and metallicity priors

We test and discuss the Gaussian priors on b_W and Z_W described in E14 (but not mentioned in R11), and explain our choices for our fits. E14 performs Cepheid fits with and without Gaussian priors centred at $b_W = -3.23$ and $Z_W = 0$, motivated by expectations of what the slope and metallicity dependence should be. We test the same priors in our fits but ultimately decide to not include these different priors as one of the variables in our fit, for reasons which follow.

Out of all the Cepheid data, the LMC Cepheids constrain the slope b_W most tightly. Given the relative paucity of data on the Leavitt law, we always include this information on the Leavitt law in all our fits, independent of whether the LMC is used as a distance anchor. For the fits where the LMC is not included as an anchor, we impose the same Gaussian prior on the slope as in E14: $\langle b_W \rangle = -3.23$ and $\sigma_{b_W} = 0.10$. If the LMC is used as an anchor, there is already a contribution to the likelihood from these Cepheids, so it is inappropriate to re-use this information as a prior. Then, the inclusion of the prior on b_W is prescribed by the distance anchor.

The metallicity priors in E14 are motivated by the observed strong dependence of the Cepheids' period on metallicity, in contrast with expectations that $Z_W \sim 0$, based on theoretical considerations and measurements in the LMC (Freedman & Madore 2011; Efstathiou 2014, section 3.2, and references therein). However, the R11 sample of Cepheids demonstrates a strong metallicity dependence, with values of Z_W around -0.3 or -0.5 for the R11 and E14 rejection algorithms, respectively. The difference between values for Z_W from the two approaches to outlier rejection (detailed in Appendix A1) can be traced to a sample of low-metallicity Cepheids that are rejected by cuts in R11 but not E14. This systematic difference (discussed in E14, section 3.2) arose from the erroneous extrapolation of metallicity gradients to large radii, and was later corrected in R16. Including both the LMC and MW as distance anchors reduces the magnitude of the metallicity dependence Z_W. As we have observed that the R11 Cepheid data do not support the $Z_W \sim 0$ priors (weak or strong) in E14, it is most appropriate to exclude these Gaussian priors in our analysis.

APPENDIX B: SUPERNOVA LIGHT CURVES AND DATA

B1 SALT2 light-curve fits

For each SN, we use SALT2 to fit SN Ia light curves (i.e. determine parameters m_B, X_1, and C in equation 14). The SALT2 model, based on its precursor SALT (Guy et al. 2005), is described in

Guy et al. (2007) along with details of its training. Two newer versions, SALT2.2 and SALT2.4, with additional training samples, have been released with the SNLS and JLA analyses, respectively in Guy et al. (2010) and Betoule et al. (2014, hereafter B14). Notably these include SNe from the SDSS-II survey (Sako et al. 2014) and high-z SNe which have constrained the model better in the rest-frame ultraviolet region, eliminating the need to exclude U-band data as in R11.

Primary inputs for the SALT2 light-curve-fitting routine `snfit` are photometry in each filter, heliocentric redshifts, and MW extinction [obtained from Schlegel, Finkbeiner & Davis (1998) dust maps] for each SN. In addition, zero-points and filter transmissions for each passband of each instrument are necessary. As CfA3 SNe are included in the JLA analysis and the SALT2.4 release, we only need to create LOSS instruments KAIT1–4 and NICKEL. Adding these instruments involves including the filter transmissions[24], and determining zero-points for BD+17°4708[25] using colour transformations in Ganeshalingam et al. (2010, table 4). Our photometry and the instruments used are briefly mentioned in Section 5.1 and Appendix C4; for more details see the survey papers (Hicken et al. 2009a; Ganeshalingam et al. 2010).

B1.1 Photometry consistency checks

We are able to compare our SALT2 fit results to published values for a subsample of our SNe Ia, namely some of the CfA3 SNe which appear in SNLS (Conley et al. 2011, hereafter C11) and JLA (B14). Hicken et al. (2009b) and Ganeshalingam et al. (2013) also report SALT2 fits of their samples, albeit with an older version of SALT2. We thoroughly check for consistency between these results and find agreement within quoted uncertainties, with no systematic differences.

Furthermore, we examine both the photometry and light-curve fits for the 69 SNe in the CfA3–LOSS overlap, taking into account the different magnitude systems. For the directly comparable passbands (the Bessell-like $BVRI$ filters), the photometry is consistent, while differences from the SDSS ri filters in Keplercam are in line with expectations. We also compare results of light-curve fits using only CfA3 photometry, only LOSS photometry, and both combined in a single light curve. We find that SALT2 parameters $\{\alpha, \beta\}$, determined from each survey separately, generally average to the parameters determined from the combined fit (which lie well within reported uncertainties of from either CfA3 or LOSS). Occasionally one survey dominates in its influence over the SALT2 parameters; this occurs equally often with each survey and only when the light-curve quality is discernibly superior in terms of number of points, sampling frequency, and size of uncertainties. Furthermore, we test for systematic offsets in the three SALT2 fit parameters m_B, X_1, C, and find none. The comparison of combined lightcurves and their SALT2 fits supports the consistency of CfA3 and LOSS and favours neither over the other; thus we concatenate photometry from CfA3 and LOSS instruments to obtain the highest quality light curves available for these SNe.

---

[24] These filters can be found in the UC Berkeley Filippenko Group's Supernova Database (SNDB; Silverman et al. 2012) at http://heracles.astro.berkeley.edu/sndb/info, maintained by Isaac Shivvers.

[25] This is the fundamental SDSS standard star that the Vega-based magnitude system @VEGA2 in SALT2.4 is calibrated on.

B2 Malmquist bias correction

In magnitude-limited surveys, intrinsically brighter objects are preferentially detected, leading to Malmquist bias: a skewed estimate of the absolute magnitude distribution. The Malmquist bias can be estimated by modelling the selection efficiency (i.e. the rate of successful detection as a function of magnitude) to match observed distributions (in redshift, stretch, and colour), then simulating the survey with SNANA (Kessler et al. 2009) to obtain the bias $\delta\mu$ in distance modulus. This procedure, described in e.g. Scolnic & Kessler (2016), is outside the scope of this work. Thus, we adopt the estimate of the bias (for low-z SNe) in Betoule et al. (2014, section 5.3), which adopts a magnitude-limited selection function, and uses the difference between the resultant bias and an unbiased regime as the uncertainty in the correction (the covariance matrix $\mathbf{C_{bias}}$ in Appendix C1). The targeted discovery of SNe in CfA3 and LOSS means they should not be magnitude limited; however, as observed in the JLA low-z sample, the colour distribution grows more blue with redshift, suggesting that some selection effect is at play. Using the JLA approximation is justified as our SN sample is similarly distributed to the low-z sample in JLA, and the bias correction is inherently approximate and has a miniscule impact on H_0.[26]

B3 Host galaxy dependence

The dependence of the intrinsic SN Ia brightness on properties of their host galaxies is well established, with numerous studies finding that more massive galaxies (correlated with higher metallicity and lower specific star formation rates) host SNe which are on average ~0.08 mag brighter (e.g. Sullivan et al. 2010; Lampeitl et al. 2010; Kelly et al. 2010). To mitigate the systematic error that this effect introduces to the cosmological analysis, we follow Sullivan et al. (2011) and subsequent analyses (C11, B14) in adopting two discrete values for the SN Ia absolute magnitude, using the variable

$$M_B^* := \begin{cases} M_B, & \text{host galaxy mass} < 10^{10} M_\odot \\ M_B + \Delta M_B, & \text{host galaxy mass} > 10^{10} M_\odot. \end{cases} \quad \text{(B1)}$$

We fit for the parameter M_B as indicated in Section 3, and fix the offset ΔM_B based on analyses in C11, B14, Sullivan et al. (2010), and Childress et al. (2013), which determine $\Delta M_B = -0.08$ from SN Ia samples greater in size and redshift range than ours. We consider fitting for the magnitude offset using our data, and find a larger absolute difference $\Delta M_B = -0.15 \pm 0.07$ (with some degeneracy with $\mathcal{M}$), which is still consistent with the established value in the literature. Given the large uncertainty on our value, we adopt the more reliable reference value.

The host galaxy masses for our SNe are obtained from the literature where available, with 77 from JLA and 71 from a combination of Sako et al. (2014), Childress et al. (2013), Neill et al. (2009), and Kelly et al. (2010). The stellar masses of nearby galaxies are all given in Neill et al. (2009). We were able to derive mass estimates for 72 of the remaining galaxies using SDSS photometry, following standard methods in Sullivan et al. (2006) and Smith et al. (2012). We refer the reader to descriptions therein of the method, which relies on the ZPEG photometric redshift code (Le Borgne & Rocca-Volmerange 2002, 2010) based on spectral energy densities from the PEGASE.2 spectral synthesis code. Where possible, we check for
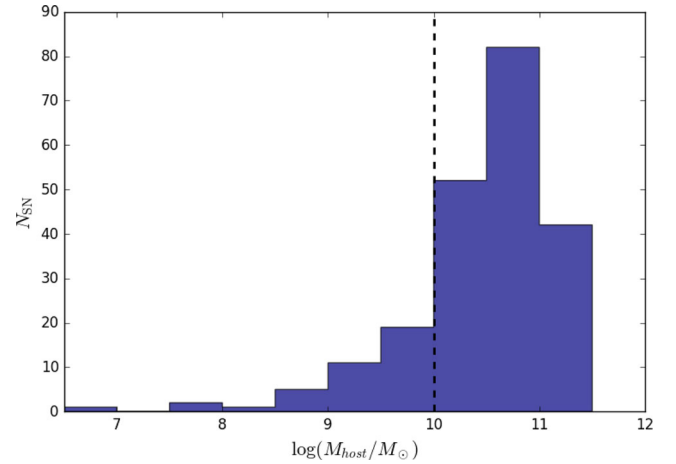
Figure B1. Histogram of host galaxy masses of low-z SNe Ia where available (total off 220 SNe). The dashed line indicates the boundary $10^{10} M_\odot$ which splits the absolute SN Ia magnitude (equation B1).

consistency between multiple sources and our estimates. The distribution of the host masses of the CfA3 and LOSS SNe Ia (Fig. B1) clearly shows that they predominantly exist in more massive galaxies, with 241 out of 280 SNe lying in the high-mass bin. This is a consequence of the targeted nature of these surveys, in contrast to the magnitude-limited surveys SNLS and SDSS in JLA. Thus, we assign the remaining 60 SNe with unknown masses to the high-mass bin with a large associated uncertainty, even though unknown hosts in JLA are assigned to the low-mass bin (B14, section 5.2). The propagation of uncertainties in this correction through to SN parameters is later described in Appendix C5.

B4 Peculiar velocity corrections

Peculiar velocities arise from motion other than from cosmological expansion, such as dipole or bulk flows, local galaxy infall, and higher order coherent flows. These perturb the observed redshifts via the Doppler effect,[27] and can impact cosmological analyses. Hui & Greene (2006) show that neglecting correlations between peculiar velocity uncertainties at low redshift results in a greatly underestimated zero-point uncertainty, and degrades the precision of the dark energy equation of state parameter w. Moreover, correlated SN peculiar velocities can bias cosmological results: Davis et al. (2011) show that neglecting coherent flows result in a shift of $\Delta w = 0.02$.

Thus, an effort to quantify the uncertainty induced by correlated motions is an essential part of any modern SN Ia cosmological analysis. Approaches to this include the addition of large (300–400 km s^{-1}) uncertainties in redshifts to account for peculiar velocities (Ganeshalingam et al. 2013; Hicken et al. 2009b), and attempts to correct for peculiar velocities. The latter first appeared in SNLS (C11), which corrects redshifts on an SN-by-SN basis for the (line-of-sight) peculiar velocity at the location of the SN, as determined from a velocity field.

---

[26] The difference between correcting for Malmquist bias and no correction is less than 0.01 in $\mathcal{H}$, or ~0.4 per cent in H_0.

[27] An SN's peculiar motion changes not only its redshift but also its observed luminosity (Hui & Greene 2006; Davis et al. 2011) as it experiences relativistic beaming. This in turn induces a deviation in the supernova's peak magnitude; however this is approximately an order of magnitude smaller than the change in redshift.

C11 uses the velocity field in Hudson et al. (2004), derived from the galaxy density field from the *IRAS* PSCz redshift survey (Branchini et al. 1999). While B14 adopt the same correction, we apply the same method using updated density and velocity fields from the 2M++ redshift compilation.[28] In each case, the velocity field is derived from the respective density fields under a linear biasing approximation.[29]

In correcting SN redshifts for peculiar velocities, the aim is to isolate the redshift due purely to expansion. The several redshifts of interest are: the heliocentric redshift z_h, the CMB frame redshift z_{cmb}, and the cosmological redshift $\bar{z}$. The latter two differ in that $\bar{z}$ is corrected for peculiar velocities from coherent flows; it is intended to reflect a velocity derived only from the expansion of space and therefore this is the redshift that should be used in $v(z)$ in Hubble's law. The peculiar motions to consider in converting z_h to $\bar{z}$ are the motions of the Solar system ($\boldsymbol{v}_\odot^{pec}$), and of the SN ($\boldsymbol{v}_{SN}^{pec}$), both relative to the CMB. Many SNe at low redshifts share some of the Local Group's motion; by converting to a heliocentric frame (i.e. correcting for the Sun's motion relative to the CMB) we are also overcorrecting for the motion of nearby SNe, necessitating the second correction. For an SN at position $\boldsymbol{n}$ from the Sun, these redshifts and velocity are related by[30] (Davis et al. 2011)

$$1 + z_h = (1 + \bar{z})(1 + z_\odot^{pec})(1 + z_{SN}^{pec})$$
$$\approx (1 + \bar{z})(1 - \boldsymbol{v}_\odot^{pec} \cdot \boldsymbol{n}/c + \boldsymbol{v}_{SN}^{pec} \cdot \boldsymbol{n}/c). \quad (B3)$$

For our analysis of the low-z SNe Ia, we use $\bar{z}$ derived in this way as the CMB-frame redshift. Unless otherwise specified, this is the redshift meant by z.

The exact form of the luminosity distance introduced in equation (2) actually requires both the heliocentric and cosmological redshifts:

$$D_L(z_h, \bar{z}) = (1 + z_h)D(\bar{z}). \quad (B4)$$

This is because the factors affecting the $(1 + z_h)$ pre-factor (redshifting and beaming) depend on the total relative velocities, whereas the cosmological distance only depends on $\bar{z}$, the redshift due to expansion (Calcino & Davis 2017, appendix A). The difference resulting from using $\bar{z}$ for both is negligible so we do not differentiate in our analysis. Calcino & Davis (2017, sections 4.2 and 4.3) quantify the effect of possible redshift systematic errors on the derivation of H_0 and find that a systematic redshift error as small as $\sim 2.6 \times 10^{-4}$ can result in a ~ 0.3 per cent bias in H_0.

The peculiar velocity corrections we make here are reliant on predicted velocity fields, which are intrinsically approximate. We discuss and quantify these uncertainties in Appendix C6, and propagate them to the SN fit parameters. Moreover, we ensure that our corrections do not bias our results: if the results of our SN-only fit

---

[28] Carrick et al. (2015); data available at http://cosmicflows.iap.fr/.

[29] That is, the mass density and galaxy number density are proportional via the linear bias factor b, i.e. $\delta_g = b\delta$. In this regime, peculiar velocities are proportional to gravitational attraction:

$$\boldsymbol{v} = \frac{\beta^*}{4\pi} \int_0^{R_{max}} \delta_g(\boldsymbol{r}') \frac{(\boldsymbol{r}' - \boldsymbol{r})}{|\boldsymbol{r}' - \boldsymbol{r}|^3} \, d^3\boldsymbol{r}' + \boldsymbol{U}, \quad (B2)$$

where $\boldsymbol{U}$ represents a residual dipole (in 2M++ this is the dipole of the Local Group), with $\beta^* = \frac{f(\Omega_M)}{b} = 0.43$ (Carrick et al. 2015) where $f(\Omega_M) = \Omega_M^{0.55}$ for ΛCDM (Wang & Steinhardt 1998).

[30] The minus sign in front of $\boldsymbol{v}_\odot^{pec}$ arises because we have defined it is the motion of the Sun relative to the CMB, rather than the other way around.
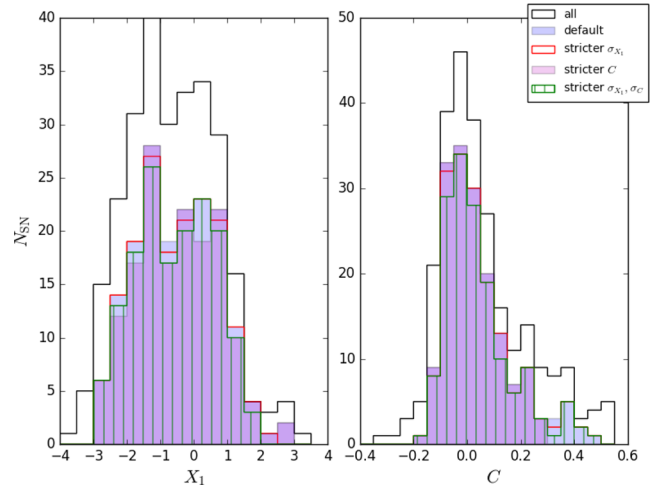
Figure B2. Histograms of the X_1, C distributions with alternate cuts on their values and uncertainties (Section 5.3). These show that constraints on uncertainties in X_1 and C remove the slowest declining SNe, and that imposing a stricter cut on the colour affects the C distribution asymmetrically.
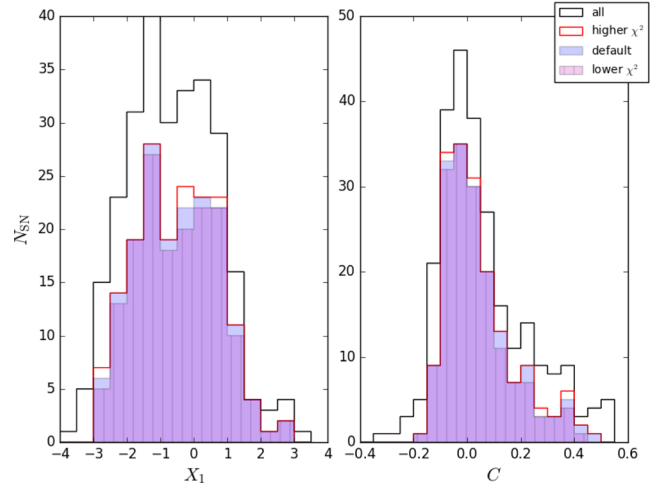
Figure B3. Histograms of the X_1, C distributions with alternate cuts on the light-curve goodness of fit χ^2/d.o.f. (Section 5.3). The SN Ia distributions with these cuts and the default cut appear similar.

(Section 5.4) varied significantly with the introduction of the correction, then this effect would need to be explored and quantified. In this scenario, the impact of performing a velocity correction would greater than the uncertainty contribution in C_{pecvel} (Appendix C6). However, we find a negligible effect on the zero-point $\mathcal{M}$ (less than 10 per cent of the statistical uncertainty) in the SN-only fit when peculiar velocity corrections are omitted. Consequently, the velocity correction cannot bias H_0 (as $\mathcal{H} = M_B - \mathcal{M}$).

B5 Histograms for SN cuts

We include in Figs B2–B4, the stretch and colour distributions of our low-z SNe Ia with various alternate cuts relative to the default, all described in Section 5.3. We observe that the X_1 distribution changes marginally with stricter cuts on σ_{X_1} and a higher low-redshift cut. Naturally, the C distribution is affected by a stricter cut on C. Otherwise, there is no significant impact on the stretch and colour distributions from alternate cuts, and in particular no
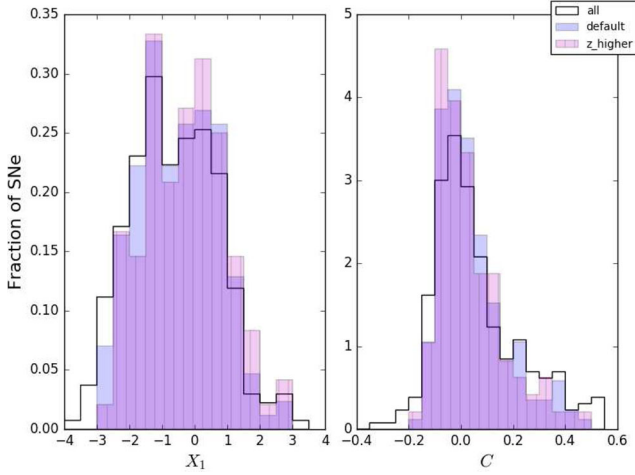
Figure B4. Normalized histograms of the X_1, C distributions with a higher low-redshift cut of $z > 0.0233$. The proportion of higher X_1 (slower declining) SNe is marginally higher with the $z > 0.0233$ cut, but otherwise the relative distributions appear very similar.

evidence that the variation observed in Fig. 2 in Section 5.5 arises from such biases.

APPENDIX C: COMPUTING SUPERNOVA SYSTEMATICS

This section is devoted to the construction of the SN Ia covariance matrices. We break down systematic and statistical terms that contribute to the error budget, and describe their propagation to the SN magnitudes.

C1 Overview of covariance matrices

Each covariance matrix tracks uncertainties in the vector $\eta = \{m_{Bi}, X_{1i}, C_i\}_{1 \le i \le N}$, which contain the SALT2 quantities for all $N = 280$ low-z SNe. These matrices sum to the $3N \times 3N$ matrix $\mathbf{C}_\eta$ which encompasses all covariances in η, and are independent of α and β. For fitting the low-z SN data, we require covariances in SN magnitudes in the form of $\mathbf{C}_{m_B^\dagger}$ (equation 22), which is derived from $\mathbf{C}_\eta$ by conjugation with the $N \times 3N$ matrix $\mathbf{A}$ (with $\mathbf{A_{ij}} = \delta_{3i,j} + \alpha\delta_{3i+1,j} + \beta\delta_{3i+2,j}$):

$$\mathbf{C}_{m_B^\dagger} = \mathbf{A}\mathbf{C}_\eta\mathbf{A}^T + \mathrm{diag}\left(\frac{5\sigma_z}{z\log 10}\right)^2 \tag{C1}$$

$$+\mathrm{diag}(\sigma_{\mathrm{lens}}^2) + \mathrm{diag}(\sigma_{\mathrm{int,SN}}^2). \tag{C2}$$

The remaining terms are diagonal uncertainties, which affect each SN individually, ascribed to uncorrelated uncertainties in redshift due to peculiar velocity uncertainties (distinct from the uncertainty in their corrections, described in Appendix C6), and perturbances in SN Ia magnitudes caused by gravitational lensing and intrinsic scatter. We adopt the values for these used in C11 and B14, of $c\sigma_z = 150$ km s^{-1}, $\sigma_{\mathrm{lens}} = 0.055z$, and $\sigma_{\mathrm{int, SN}} = 0.12$.

To understand $\mathbf{C}_\eta$, we first separate it into statistical and systematic components, and later explain the distinction in Appendix C2. The contributions to $\mathbf{C_{sys}}$, we consider are from uncertainties in the following sources: peculiar velocity corrections, MW extinction, host galaxy mass dependence, photometric calibration, Malmquist

bias correction, and light-curve model.[31] For the nearby SNe (i.e. those in galaxies containing Cepheids), we only include $\mathbf{C_{diag}}$ and $\mathbf{C_{host}}$. The host mass correction has the potential to shift the magnitude scale by up to $\sim$0.08 mag, and is important in the context of the dependence of SN Ia magnitude on host galaxy properties (Appendix C5). The other correction terms, for Malmquist bias and peculiar velocities, are redshift-dependent effects hence irrelevant for this sample. The remaining covariance matrices are not tied to the corrections in Appendices B2–B4, and are more precise than warranted, given the inhomogeneity and larger uncertainties in these data, so we neglect them .

$$\mathbf{C}_\eta = \mathbf{C_{stat}} + \mathbf{C_{sys}};$$
$$\mathbf{C_{sys}} = \mathbf{C_{bias}} + \mathbf{C_{cal}} + \mathbf{C_{dust}} + \mathbf{C_{host}} + \mathbf{C_{model}} + \mathbf{C_{pecvel}}. \tag{C3}$$

We follow standard techniques to compute each covariance matrix, which is to enfold partial derivatives of SN parameters with respect to each systematic, with the typical size of systematics:

$$\mathbf{C_{sys}}_{ij} = \sum_k \left(\frac{\partial\eta_i}{\partial k}\right)\left(\frac{\partial\eta_j}{\partial k}\right)(\Delta k)^2. \tag{C4}$$

Here, the sum is over all systematics k, each of size Δk. Equation (41) is applied directly to compute $\mathbf{C_{dust}}$ and $\mathbf{C_{cal}}$. These calculations are intrinsically approximate, yet even as estimates they are invaluable for gauging the contribution of each systematic term affecting SNe Ia, and affirming that we sufficiently account for each effect. Section 6.3.3 presents our assessment of these uncertainties.

We first digress to discuss the statistical term $\mathbf{C_{stat}}$, then address the construction of each systematic in turn. We describe our calculations of the first four systematics from first principles. Computations of the bias and model uncertainties, as well as the non-diagonal part of $\mathbf{C_{stat}}$ require estimates of the sample's selection function (as discussed in Appendix B2), thorough end-to-end simulations with several light-curve models, and in-depth deconstruction and analysis of the SALT2 model. These have been performed in section 5.3 of B14, Mosher et al. (2014), and Guy et al. (2010, Appendix A3), respectively. We obtain our best estimate of these matrices for our low-z SN Ia sample, and refer the reader to the aforementioned references for details.

C2 Statistical uncertainties

The distinction between statistical and systematic errors blurs, as many uncertainties have sources for which both descriptors are appropriate. We adopt the separation used in C11, which defines statistical uncertainties as those that can be reduced by increasing the size of some data set. In this case the data sets are the measured low-z SNe, and the training set used to define the SALT2 parameters (Guy et al. 2010, updated in B14). We separate these two terms into matrices $\mathbf{C_{stat,diag}}$ and $\mathbf{C_{stat,model}}$ respectively.[32]

The matrix $\mathbf{C_{stat,diag}}$ arises from uncertainties in the measurement of light curves, constructed directly from correlated uncertainties in m_B, X_1, C (a 3×3 covariance matrix for each SN) reported in SALT2 outputs. These terms are uncorrelated between different SNe, so $\mathbf{C_{stat,diag}}$ is tridiagonal (i.e. only a diagonal strip of width 3 is non-zero).

---

[31] This is equation (11) of B14 without the contamination term $\mathbf{C_{nonIa}}$, which only concerns higher redshift SNe.

[32] In B14, these two terms are combined as $\mathbf{C_{stat}}$, while C11 sums $\mathbf{C_{stat,diag}}$ and the three diagonal terms in our equation (C1) to their $\mathbf{D_{stat}}$.

Table C1. Systematics in κ.

Instrument	Filters	ZP index	λ_{eff} index
MegaCam	*griz*	0–3	50–53
Standard	*UBVRI*	4–8	54–58
KeplerCam	*UsBVri*[a]	9–13	59–63
4Shooter2	*UsBVRI*	14–18	64–68
Swope	*ugriBV*	19–24	69–74
SDSS	*ugriz*	25–29	75–79
KAIT1-4	*BVRI*	30–45	80–95
NICKEL	*BVRI*	46–49	96–99

Note. [a]*Us* indicates the standard Landolt *U* passband, derived from Bessell (1990) (see Section 5.1).

The latter matrix $\mathbf{C_{stat,model}}$ contains the uncertainty in the SALT2 model from the finiteness of the training sample, which could theoretically be decreased by training SALT2 on more SNe. Its calculation requires propagating statistical uncertainties in the light-curve model through to SN fit parameters η, as described in Guy et al. (2010, Appendix A3) and implemented in the snpca package.[33] We use the code salt2_stat from this package to directly compute $\mathbf{C_{stat,model}}$.

C3 Milky Way extinction

The calculation of our first systematic covariance matrix directly follows equation (41). This contains the uncertainty in η due to the uncertainty in the MW extinction. The sole systematic k is the uncertainty in the $E(B - V)$ value from dust maps (Schlegel et al. 1998); we follow the conservative estimate in B14 of a 20 per cent relative uncertainty. Perturbing the value of the extinction (encoded in the dust keyword @MWEBV in SALT2 inputs) and refitting light curves give the partial derivatives in equation (C3):

$$\mathbf{C_{dust}}_{ij} = \left(\frac{\partial \eta_i}{\partial E(B - V)} \right) \left(\frac{\partial \eta_j}{\partial E(B - V)} \right) (0.2 \times E(B - V))^2. \tag{C5}$$

We verify that the partial derivatives of SN parameters η with respect to MW extinction are independent of the size of perturbation over a satisfactory range, and that our resultant $\mathbf{C_{dust}}$ is identical to the same matrix reported in B14 for the 60 SNe Ia in common.

C4 Calibration

B14 and C11 emphasize the significant contribution of uncertainties in the calibration of individual surveys to the total error budget. We follow the methods therein and in Betoule et al. (2013) to reproduce the calibration covariance matrix relevant to our SN sample and the instruments used to observe them. Computing the calibration matrix $\mathbf{C_{cal}}$ relies on the same principle as in Appendix C3, but over multiple systematics. Calibration uncertainties are grouped into two types of systematics: uncertainties in the magnitude zero-point (shifting the overall flux scale) and in the effective wavelength (shifting the transmission function in wavelength space), for each filter. These are contained in the vector κ and enumerated in Table C1.

The instruments and passbands to consider in κ are those used for observing the low-*z* SNe: 4Shooter2 and Keplercam for CfA3, and KAIT1–4 and NICKEL for LOSS, and those involved in the

[33] Private SNLS communication.

training of SALT2 (i.e. used to observe the SNe in the training sample). The latter, and sizes of systematics in these passbands, are given in B14, table 5. It is necessary to include these training instruments and passbands as they influence measured magnitudes of training SNe hence the SALT2 model.

We directly consider the covariance matrix of calibration systematics $\mathbf{C_{\kappa ij}} = \langle \sigma_{\kappa_i} \sigma_{\kappa_j} \rangle$, which captures the correlations between systematics in different instruments and passbands. Then, equation (41) is equivalent to $\mathbf{C_{cal}} = \mathbf{J} \mathbf{C_{\kappa}} \mathbf{J}^T$ where $\mathbf{J}_{ij} = \frac{\partial \eta_i}{\partial \kappa_j}$ is the Jacobian matrix, encoding partial derivatives of SN parameters. Then finding $\mathbf{C_{cal}}$ amounts to constructing $\mathbf{C_{\kappa}}$, and calculating $\mathbf{J}$ from first principles. For the LOSS instruments, we achieve the latter by either perturbing an element of κ (i.e. shift the zero-point of effective wavelength). For the other instruments, which were involved in training SALT2, we change to a different SALT2 model altogether i.e. one that was trained with the systematic shift in question applied. Each SN light curve is fitted again to find the difference, and the resultant Jacobian is smoothed in accordance with footnote 9 of B14.

To find $\mathbf{C_{\kappa}}$, we start with the same matrix from JLA and re-index it according to Table C1, appending the LOSS instruments and removing *HST* instruments NICMOS and ACSWF (which do not contribute to the SALT2 training sample). We approximate the elements of $\mathbf{C_{\kappa}}$ for LOSS instruments as diagonal: this is exact for the λ_{eff} elements, and a good approximation for the zero-point. Using Ganeshalingam et al. (2010) as a guide, we take the zero-point and λ_{eff} uncertainties to be 0.03 mag and 10 Å, respectively. As LOSS observations (with KAIT1–4 and NICKEL) of SNe Ia were not used for SALT2 training, only SNe in the sample with LOSS measurements have non-zero partial derivatives with respect to these instruments.

C5 Host galaxy mass

The SN Ia magnitude zero-point M_B is corrected for the magnitude offset Δ_M between high and low host galaxy (stellar) mass bins, as described in Appendix B3. The uncertainty in this correction is propagated to SN parameters in $\mathbf{C_{host}}$. As in B14, we treat the systematic associated with this correction as having two components: from potentially having attributed an individual SN to the wrong host mass bin, and from the arbitrariness of the $10^{10} M_{\odot}$ cut. Both effects are discrete, so the computation of $\mathbf{C_{host}}$ differs from those of $\mathbf{C_{dust}}$ and $\mathbf{C_{cal}}$ which take partial derivatives with respect to continuous quantities.

Our calculation follows identically the method in B14. As discussed in Appendix B3, our data do not justify fitting for Δ_M, and instead we adopt a fixed value from literature. Only SN magnitudes are affected: the only indices of non-zero components of $\mathbf{C_{host}}$ correspond to the m_B components of η, but for compatibility for the other matrices we make $\mathbf{C_{host}}$ the same size ($3N \times 3N$). The vectors $\mathbf{H}_h$ and $\mathbf{H}_l$ are indicator functions of (the magnitudes of) the SNe with masses within an order of magnitude higher and lower, respectively, than the mass boundary $10^{10} M_{\odot}$, while $\mathbf{B}$ is an indicator function for the SNe whose host mass estimates and uncertainties in combination imply that they could be assigned to either bin. Then, the covariance matrix for the host mass correction is:

$$\mathbf{C_{host}} = \Delta_M^2 (\mathbf{H}_h \mathbf{H}_h^T + \mathbf{H}_l \mathbf{H}_l^T + \mathrm{diag}(\mathbf{B})). \tag{C6}$$

For the overlap of our SNe with B14, results are very similar, with differences arising only from SNe with masses newly obtained or updated (Appendix B3).

C6 Peculiar velocities

As described in Appendix B4, we have corrected individual SN redshifts for peculiar motion, using the 2M++ velocity field corrections. However, there is intrinsic uncertainty in these models, with variation between velocity fields generated from different galaxy density fields, and in some cases limited agreement between predicted and measured velocities (Springob et al. 2014; Scrimgeour et al. 2016).

Thus, the significant contribution in the correction model itself must be taken into account. Below, we adopt the approach in C11 and B14, which is to use the uncertainty in the velocity field to inform $\mathbf{C}_{\text{pecvel}}$, the contribution to $\mathbf{C}_\eta$ from peculiar velocities. We emphasize that this is distinct from the diagonal term σ_z in equation (C1).

For a given density field δ_g, the velocity field derived through equation (B2) can be parametrized by β^*, the ratio of the growth rate of density perturbations to the linear bias factor. In C11, β^* is the systematic which encompasses the uncertainty in the peculiar velocity model; that is, $\mathbf{C}_{\text{pecvel}}$ is derived through equation (41) with $k = \beta^*$. As this treatment of uncertainty lies within only one density field and model (that is, it does not account fully for velocities derived from different realizations/measurements of galaxy densities) we are conservative in using it; like C11 we perturb β^* by five times its uncertainty.[34] Likewise, we adopt $\beta^* = 0.43 \pm 0.02$ (Carrick

---

[34] Pike & Hudson (2005) find $\beta^* = 0.49 \pm 0.04$ so C11 vary β^* between 0.3 and 0.7.

et al. 2015) in the correction. To compute $\mathbf{C}_{\text{pecvel}}$, we measure the shift in z_{cmb} when β^* is set to 0.33 or 0.53 instead. The resultant difference in z_{cmb} is propagated to m_B using the derivative of equation (15):

$$\sigma_{m_B} = \frac{5}{\log 10} \left(\frac{1}{z} + \frac{f'(z)}{f(z)} \right) \sigma_{z_{\text{cmb}}}. \tag{C7}$$

This has no impact on the stretch and colour of SNe, so only the m_B elements of $\mathbf{C}_\eta$ have non-zero entries from $\mathbf{C}_{\text{pecvel}}$.

APPENDIX D: FULL TABLES OF FIT RESULTS

This appendix supplements Sections 4 and 6 with full tables of the Cepheid and global fits, and the averaged results for $\{\Delta\mu_i\}$ from the global fit.

D1 Results of Cepheid-only fit

D2 Full results for $\{\Delta\mu_i\}$

D3 Full results of global fit

Table D1. Results of the Cepheid-only fits described in Section 4.3 from each combination of distance anchor, rejection, and period cut for each Cepheid fit. The best-fitting Cepheid parameters $\{b_W, Z_W, M_W\}$ are given, as well as the number of Cepheids remaining after rejection and intrinsic scatter.

Rejection	Distance anchor	$P < 60d$	N_{Cepheids}	$\sigma_{\text{int, C}}$	b_W	Z_W	M_W
$T = 2.25$	n4258	Y	439	0.17	$-3.23\ (0.07)$	$-0.54\ (0.13)$	$-6.03\ (0.07)$
$T = 2.5$	n4258	Y	463	0.27	$-3.22\ (0.08)$	$-0.49\ (0.14)$	$-6.06\ (0.07)$
R11	n4258	Y	379	0.21	$-3.18\ (0.07)$	$-0.32\ (0.14)$	$-6.05\ (0.08)$
$T = 2.25$	LMC	Y	439	0.17	$-3.24\ (0.05)$	$-0.54\ (0.13)$	$-6.16\ (0.07)$
$T = 2.5$	LMC	Y	464	0.27	$-3.24\ (0.05)$	$-0.50\ (0.14)$	$-6.14\ (0.08)$
R11	LMC	Y	379	0.21	$-3.22\ (0.05)$	$-0.32\ (0.14)$	$-6.07\ (0.07)$
$T = 2.25$	MW	Y	439	0.17	$-3.24\ (0.07)$	$-0.54\ (0.13)$	$-5.83\ (0.05)$
$T = 2.5$	MW	Y	463	0.27	$-3.24\ (0.07)$	$-0.49\ (0.15)$	$-5.83\ (0.05)$
R11	MW	Y	379	0.21	$-3.20\ (0.07)$	$-0.32\ (0.15)$	$-5.82\ (0.05)$
$T = 2.25$	n4258+LMC	Y	439	0.18	$-3.23\ (0.05)$	$-0.46\ (0.11)$	$-6.10\ (0.05)$
$T = 2.5$	n4258+LMC	Y	466	0.28	$-3.23\ (0.05)$	$-0.42\ (0.12)$	$-6.10\ (0.05)$
R11	n4258+LMC	Y	379	0.21	$-3.22\ (0.05)$	$-0.29\ (0.12)$	$-6.05\ (0.05)$
$T = 2.25$	n4258+MW	Y	437	0.17	$-3.31\ (0.06)$	$-0.50\ (0.12)$	$-5.89\ (0.04)$
$T = 2.5$	n4258+MW	Y	464	0.27	$-3.30\ (0.07)$	$-0.46\ (0.14)$	$-5.90\ (0.04)$
R11	n4258+MW	Y	379	0.21	$-3.26\ (0.06)$	$-0.30\ (0.14)$	$-5.89\ (0.04)$
$T = 2.25$	LMC+MW	Y	435	0.16	$-3.27\ (0.05)$	$-0.12\ (0.10)$	$-5.91\ (0.05)$
$T = 2.5$	LMC+MW	Y	464	0.28	$-3.27\ (0.05)$	$-0.15\ (0.11)$	$-5.92\ (0.06)$
R11	LMC+MW	Y	379	0.21	$-3.25\ (0.05)$	$-0.08\ (0.11)$	$-5.90\ (0.06)$
$T = 2.25$	n4258+LMC+MW	Y	434	0.16	$-3.28\ (0.05)$	$-0.17\ (0.10)$	$-5.95\ (0.04)$
$T = 2.5$	n4258+LMC+MW	Y	463	0.27	$-3.28\ (0.05)$	$-0.19\ (0.10)$	$-5.96\ (0.04)$
R11	n4258+LMC+MW	Y	379	0.21	$-3.26\ (0.05)$	$-0.12\ (0.11)$	$-5.94\ (0.04)$
$T = 2.25$	n4258	N	521	0.2	$-3.04\ (0.05)$	$-0.42\ (0.12)$	$-6.10\ (0.07)$
$T = 2.5$	n4258	N	540	0.26	$-3.06\ (0.06)$	$-0.32\ (0.13)$	$-6.11\ (0.07)$
R11	n4258	N	444	0.21	$-3.09\ (0.06)$	$-0.21\ (0.13)$	$-6.08\ (0.07)$
$T = 2.25$	LMC	N	523	0.21	$-3.11\ (0.04)$	$-0.39\ (0.12)$	$-6.12\ (0.07)$
$T = 2.5$	LMC	N	544	0.28	$-3.12\ (0.04)$	$-0.26\ (0.13)$	$-6.06\ (0.07)$
R11	LMC	N	444	0.21	$-3.13\ (0.04)$	$-0.20\ (0.13)$	$-6.04\ (0.07)$
$T = 2.25$	MW	N	521	0.2	$-3.07\ (0.05)$	$-0.42\ (0.12)$	$-5.80\ (0.05)$
$T = 2.5$	MW	N	539	0.26	$-3.09\ (0.05)$	$-0.30\ (0.13)$	$-5.81\ (0.05)$
R11	MW	N	444	0.21	$-3.12\ (0.06)$	$-0.20\ (0.13)$	$-5.81\ (0.05)$
$T = 2.25$	n4258+LMC	N	523	0.21	$-3.11\ (0.04)$	$-0.37\ (0.11)$	$-6.09\ (0.05)$
$T = 2.5$	n4258+LMC	N	539	0.26	$-3.12\ (0.04)$	$-0.30\ (0.11)$	$-6.08\ (0.05)$
R11	n4258+LMC	N	444	0.21	$-3.13\ (0.04)$	$-0.21\ (0.12)$	$-6.05\ (0.05)$
$T = 2.25$	n4258+MW	N	520	0.2	$-3.16\ (0.05)$	$-0.40\ (0.12)$	$-5.89\ (0.04)$
$T = 2.5$	n4258+MW	N	538	0.26	$-3.16\ (0.05)$	$-0.29\ (0.13)$	$-5.90\ (0.04)$
R11	n4258+MW	N	444	0.21	$-3.17\ (0.06)$	$-0.17\ (0.13)$	$-5.89\ (0.04)$
$T = 2.25$	LMC+MW	N	519	0.2	$-3.14\ (0.04)$	$-0.05\ (0.10)$	$-5.89\ (0.05)$
$T = 2.5$	LMC+MW	N	546	0.29	$-3.14\ (0.04)$	$-0.01\ (0.10)$	$-5.89\ (0.06)$
R11	LMC+MW	N	444	0.21	$-3.16\ (0.04)$	$-0.01\ (0.10)$	$-5.88\ (0.05)$
$T = 2.25$	n4258+LMC+MW	N	517	0.19	$-3.15\ (0.04)$	$-0.09\ (0.09)$	$-5.95\ (0.04)$
$T = 2.5$	n4258+LMC+MW	N	544	0.28	$-3.16\ (0.04)$	$-0.08\ (0.10)$	$-5.96\ (0.04)$
R11	n4258+LMC+MW	N	444	0.21	$-3.17\ (0.04)$	$-0.04\ (0.10)$	$-5.94\ (0.04)$

Table D2. Global fit results for distance modulus offsets $\{\Delta\mu_i\}$ for the eight galaxies.

Cepheid rejection	Distance anchor	$P < 60$d	$\Delta\mu_{4536}$	$\Delta\mu_{4639}$	$\Delta\mu_{3370}$	$\Delta\mu_{3982}$	$\Delta\mu_{3021}$	$\Delta\mu_{1309}$	$\Delta\mu_{5584}$	$\Delta\mu_{4038}$
2.25	n4258+LMC+MW	Y	1.56 (0.05)	2.34 (0.07)	2.77 (0.06)	2.43 (0.07)	2.86 (0.09)	3.30 (0.07)	2.37 (0.05)	2.31 (0.09)
2.5	n4258+LMC+MW	Y	1.58 (0.06)	2.41 (0.08)	2.79 (0.06)	2.47 (0.09)	2.89 (0.09)	3.30 (0.08)	2.36 (0.06)	2.35 (0.10)
R11	n4258+LMC+MW	Y	1.54 (0.06)	2.35 (0.08)	2.78 (0.06)	2.43 (0.08)	2.86 (0.09)	3.18 (0.08)	2.37 (0.06)	2.32 (0.10)
2.5	n4258+LMC	Y	1.59 (0.06)	2.44 (0.08)	2.79 (0.07)	2.49 (0.09)	2.89 (0.09)	3.31 (0.08)	2.38 (0.06)	2.39 (0.10)
2.25	n4258+MW	Y	1.52 (0.05)	2.37 (0.07)	2.73 (0.06)	2.34 (0.08)	2.87 (0.09)	3.26 (0.07)	2.33 (0.06)	2.32 (0.09)
R11	LMC+MW	Y	1.56 (0.06)	2.37 (0.08)	2.80 (0.06)	2.45 (0.08)	2.88 (0.09)	3.20 (0.08)	2.38 (0.06)	2.33 (0.10)
2.25	n4258	Y	1.56 (0.06)	2.39 (0.07)	2.74 (0.06)	2.35 (0.08)	2.88 (0.09)	3.26 (0.07)	2.35 (0.06)	2.34 (0.09)
2.25	LMC	Y	1.56 (0.06)	2.39 (0.07)	2.75 (0.06)	2.35 (0.08)	2.89 (0.09)	3.27 (0.07)	2.35 (0.06)	2.34 (0.09)
R11	MW	Y	1.53 (0.06)	2.36 (0.08)	2.76 (0.07)	2.39 (0.09)	2.85 (0.10)	3.17 (0.08)	2.36 (0.06)	2.33 (0.10)
2.25	n4258+LMC+MW	N	1.64 (0.05)	2.31 (0.07)	2.76 (0.05)	2.39 (0.07)	2.81 (0.08)	3.27 (0.06)	2.40 (0.05)	2.30 (0.07)
2.5	n4258+LMC+MW	N	1.62 (0.06)	2.41 (0.08)	2.79 (0.06)	2.44 (0.08)	2.89 (0.09)	3.30 (0.07)	2.41 (0.05)	2.35 (0.08)
R11	n4258+LMC+MW	N	1.57 (0.06)	2.34 (0.08)	2.78 (0.06)	2.41 (0.08)	2.87 (0.09)	3.21 (0.07)	2.39 (0.05)	2.32 (0.08)
2.25	n4258+MW	N	1.58 (0.05)	2.35 (0.07)	2.72 (0.05)	2.32 (0.08)	2.87 (0.08)	3.24 (0.07)	2.38 (0.05)	2.32 (0.07)
2.25	LMC+MW	N	1.67 (0.05)	2.34 (0.07)	2.79 (0.05)	2.42 (0.07)	2.84 (0.08)	3.30 (0.07)	2.43 (0.05)	2.32 (0.07)
R11	LMC+MW	N	1.59 (0.06)	2.36 (0.08)	2.80 (0.06)	2.43 (0.08)	2.89 (0.09)	3.22 (0.07)	2.41 (0.05)	2.33 (0.08)
2.25	n4258	N	1.64 (0.05)	2.37 (0.07)	2.73 (0.05)	2.34 (0.08)	2.89 (0.08)	3.25 (0.07)	2.38 (0.05)	2.32 (0.07)
2.5	n4258	N	1.61 (0.06)	2.41 (0.08)	2.77 (0.06)	2.40 (0.08)	2.88 (0.09)	3.27 (0.07)	2.40 (0.06)	2.34 (0.08)
R11	n4258	N	1.55 (0.06)	2.34 (0.08)	2.75 (0.06)	2.37 (0.08)	2.85 (0.09)	3.18 (0.07)	2.37 (0.06)	2.31 (0.08)

Table D3. Results of all global fits described in Section 6.1, from each combination of Cepheid fit and SN cut. The SN parameters $\{\alpha, \beta\}$, the Cepheid parameters $\{b_W, Z_W, M_W\}$, and the zero-points $\{\mathcal{H}, M_B, \text{and } \mu_{4258}\}$ are displayed. The indicative fits from which statistical uncertainties for parameters are retrieved are bolded.

Cepheid rejection	Distance anchor	$P < 60d$	SN cut	α	β	$\mathcal{H}$	M_B	b_W	Z_W	M_W	μ_{4258}
2.25	All	Y	Default	0.165 (0.010)	3.09 (0.11)	−15.714 (0.094)	−18.955 (0.089)	−3.28 (0.05)	−0.19 (0.10)	−5.95 (0.04)	29.36 (0.04)
2.25	All	Y	Higher χ^2	0.167 (0.010)	3.14 (0.11)	−15.706 (0.092)	−18.952 (0.087)	−3.28 (0.05)	−0.19 (0.10)	−5.95 (0.04)	29.36 (0.04)
2.25	All	Y	$z > 0.0233$	0.162 (0.012)	2.77 (0.13)	−15.705 (0.093)	−18.954 (0.087)	−3.28 (0.05)	−0.20 (0.10)	−5.95 (0.04)	29.36 (0.04)
2.25	All	Y	Lower χ^2	0.158 (0.010)	3.06 (0.12)	−15.702 (0.092)	−18.953 (0.087)	−3.28 (0.05)	−0.19 (0.09)	−5.95 (0.04)	29.36 (0.04)
2.25	All	Y	Stricter C	0.156 (0.011)	2.99 (0.14)	−15.717 (0.092)	−18.956 (0.087)	−3.28 (0.05)	−0.20 (0.10)	−5.95 (0.04)	29.36 (0.05)
2.25	All	Y	Stricter σ_{X_1}	0.171 (0.010)	3.11 (0.11)	−15.706 (0.093)	−18.950 (0.088)	−3.28 (0.05)	−0.19 (0.09)	−5.95 (0.04)	29.36 (0.04)
2.5	All	Y	Default	0.165 (0.010)	3.09 (0.10)	−15.722 (0.095)	−18.964 (0.090)	−3.28 (0.05)	−0.22 (0.10)	−5.96 (0.04)	29.35 (0.05)
2.5	All	Y	Higher χ^2	0.166 (0.010)	3.14 (0.11)	−15.722 (0.094)	−18.967 (0.089)	−3.28 (0.05)	−0.21 (0.10)	−5.96 (0.04)	29.35 (0.05)
2.5	All	Y	$z > 0.0233$	0.162 (0.012)	2.77 (0.13)	−15.722 (0.096)	−18.971 (0.091)	−3.28 (0.05)	−0.21 (0.10)	−5.97 (0.04)	29.35 (0.05)
2.5	All	Y	Lower χ^2	0.158 (0.010)	3.06 (0.12)	−15.717 (0.094)	−18.968 (0.089)	−3.29 (0.05)	−0.21 (0.10)	−5.96 (0.04)	29.35 (0.05)
2.5	All	Y	Stricter C	0.156 (0.011)	2.99 (0.14)	−15.729 (0.095)	−18.968 (0.090)	−3.28 (0.05)	−0.21 (0.10)	−5.96 (0.04)	29.35 (0.05)
2.5	All	Y	Stricter σ_{X_1}	0.171 (0.010)	3.11 (0.11)	−15.720 (0.094)	−18.964 (0.090)	−3.28 (0.05)	−0.21 (0.10)	−5.96 (0.04)	29.35 (0.04)
R11	All	Y	Default	0.165 (0.010)	3.08 (0.11)	−15.688 (0.096)	−18.930 (0.091)	−3.26 (0.05)	−0.14 (0.10)	−5.95 (0.05)	29.35 (0.05)
R11	All	Y	Higher χ^2	0.167 (0.010)	3.13 (0.10)	−15.684 (0.095)	−18.929 (0.090)	−3.26 (0.05)	−0.14 (0.11)	−5.95 (0.04)	29.35 (0.05)
R11	All	Y	$z > 0.0233$	0.162 (0.013)	2.76 (0.13)	−15.684 (0.094)	−18.933 (0.089)	−3.26 (0.05)	−0.14 (0.11)	−5.95 (0.05)	29.35 (0.04)
R11	All	Y	Lower χ^2	0.158 (0.010)	3.06 (0.12)	−15.682 (0.093)	−18.934 (0.088)	−3.26 (0.05)	−0.14 (0.10)	−5.95 (0.05)	29.35 (0.05)
R11	All	Y	Stricter C	0.156 (0.011)	2.97 (0.14)	−15.696 (0.094)	−18.935 (0.089)	−3.26 (0.05)	−0.14 (0.10)	−5.95 (0.04)	29.35 (0.04)
R11	All	Y	Stricter σ_{X_1}	0.172 (0.011)	3.11 (0.11)	−15.685 (0.094)	−18.929 (0.090)	−3.26 (0.05)	−0.14 (0.11)	−5.95 (0.04)	29.35 (0.04)
2.25	**All**	**N**	**Default**	**0.164 (0.010)**	**3.09 (0.11)**	**-15.689 (0.093)**	**-18.929 (0.088)**	**-3.18 (0.04)**	**-0.11 (0.09)**	**-5.95 (0.04)**	**29.34 (0.04)**
2.25	All	N	Higher χ^2	0.166 (0.010)	3.13 (0.10)	−15.683 (0.092)	−18.928 (0.088)	−3.17 (0.04)	−0.11 (0.09)	−5.95 (0.04)	29.34 (0.04)
2.25	All	N	$z > 0.0233$	0.160 (0.012)	2.76 (0.13)	−15.684 (0.091)	−18.933 (0.086)	−3.17 (0.04)	−0.11 (0.09)	−5.95 (0.04)	29.34 (0.04)
2.25	All	N	Lower χ^2	0.158 (0.010)	3.06 (0.12)	−15.678 (0.092)	−18.929 (0.088)	−3.17 (0.04)	−0.11 (0.09)	−5.95 (0.04)	29.34 (0.04)
2.25	All	N	Stricter C	0.155 (0.011)	2.98 (0.15)	−15.691 (0.093)	−18.929 (0.088)	−3.17 (0.04)	−0.11 (0.09)	−5.95 (0.04)	29.34 (0.04)
2.25	All	N	Stricter σ_{X_1}	0.170 (0.010)	3.11 (0.11)	−15.683 (0.093)	−18.926 (0.088)	−3.17 (0.04)	−0.11 (0.09)	−5.95 (0.04)	29.34 (0.04)
2.5	All	N	Default	0.165 (0.010)	3.09 (0.11)	−15.710 (0.093)	−18.951 (0.089)	−3.20 (0.04)	−0.09 (0.10)	−5.96 (0.04)	29.33 (0.04)
2.5	All	N	Higher χ^2	0.166 (0.010)	3.14 (0.11)	−15.707 (0.093)	−18.952 (0.089)	−3.20 (0.04)	−0.09 (0.10)	−5.96 (0.04)	29.33 (0.04)
2.5	All	N	$z > 0.0233$	0.161 (0.012)	2.76 (0.13)	−15.707 (0.094)	−18.955 (0.089)	−3.20 (0.04)	−0.10 (0.10)	−5.96 (0.04)	29.33 (0.04)
2.5	All	N	Lower χ^2	0.158 (0.010)	3.06 (0.12)	−15.702 (0.093)	−18.953 (0.089)	−3.20 (0.04)	−0.09 (0.10)	−5.96 (0.04)	29.33 (0.04)
2.5	All	N	Stricter C	0.156 (0.011)	2.98 (0.14)	−15.715 (0.095)	−18.953 (0.090)	−3.20 (0.04)	−0.10 (0.10)	−5.96 (0.04)	29.33 (0.04)
2.5	All	N	Stricter σ_{X_1}	0.171 (0.010)	3.11 (0.11)	−15.706 (0.092)	−18.950 (0.088)	−3.20 (0.04)	−0.10 (0.10)	−5.96 (0.04)	29.33 (0.04)
R11	All	N	Default	0.165 (0.010)	3.09 (0.11)	−15.682 (0.095)	−18.923 (0.090)	−3.21 (0.04)	−0.06 (0.10)	−5.94 (0.04)	29.34 (0.04)
R11	All	N	Higher χ^2	0.167 (0.010)	3.13 (0.11)	−15.677 (0.095)	−18.923 (0.090)	−3.21 (0.04)	−0.05 (0.10)	−5.94 (0.04)	29.34 (0.04)
R11	All	N	$z > 0.0233$	0.162 (0.013)	2.76 (0.13)	−15.678 (0.094)	−18.927 (0.089)	−3.21 (0.04)	−0.06 (0.10)	−5.94 (0.04)	29.34 (0.05)
R11	All	N	Lower χ^2	0.158 (0.010)	3.06 (0.12)	−15.674 (0.092)	−18.926 (0.087)	−3.21 (0.04)	−0.05 (0.10)	−5.94 (0.04)	29.34 (0.04)
R11	All	N	Stricter C	0.156 (0.011)	2.97 (0.15)	−15.687 (0.094)	−18.925 (0.089)	−3.21 (0.04)	−0.06 (0.10)	−5.94 (0.04)	29.34 (0.04)
R11	All	N	Stricter σ_{X_1}	0.171 (0.011)	3.11 (0.11)	−15.679 (0.095)	−18.923 (0.090)	−3.21 (0.04)	−0.06 (0.10)	−5.94 (0.04)	29.34 (0.04)
2.5	n4258+LMC	Y	Default	0.165 (0.010)	3.09 (0.11)	−15.818 (0.097)	−19.059 (0.093)	−3.23 (0.05)	−0.45 (0.12)	−6.11 (0.06)	29.43 (0.05)
2.5	n4258+LMC	Y	Higher χ^2	0.167 (0.010)	3.14 (0.11)	−15.814 (0.097)	−19.059 (0.092)	−3.23 (0.05)	−0.45 (0.12)	−6.11 (0.06)	29.43 (0.05)
2.5	n4258+LMC	Y	$z > 0.0233$	0.162 (0.013)	2.77 (0.13)	−15.816 (0.096)	−19.065 (0.091)	−3.23 (0.05)	−0.45 (0.12)	−6.11 (0.05)	29.43 (0.05)
2.5	n4258+LMC	Y	Lower χ^2	0.158 (0.010)	3.06 (0.12)	−15.810 (0.096)	−19.061 (0.091)	−3.23 (0.05)	−0.45 (0.12)	−6.11 (0.05)	29.43 (0.05)
2.5	n4258+LMC	Y	Stricter C	0.156 (0.011)	2.99 (0.15)	−15.822 (0.098)	−19.060 (0.092)	−3.23 (0.05)	−0.45 (0.12)	−6.11 (0.05)	29.43 (0.05)
2.5	n4258+LMC	Y	Stricter σ_{X_1}	0.171 (0.011)	3.11 (0.11)	−15.816 (0.098)	−19.060 (0.093)	−3.23 (0.05)	−0.45 (0.12)	−6.11 (0.05)	29.43 (0.05)
2.25	n4258+MW	Y	Default	0.165 (0.010)	3.08 (0.11)	−15.650 (0.097)	−18.891 (0.092)	−3.31 (0.06)	−0.52 (0.12)	−5.89 (0.04)	29.32 (0.04)
2.25	n4258+MW	Y	Higher χ^2	0.167 (0.010)	3.13 (0.10)	−15.646 (0.097)	−18.892 (0.092)	−3.31 (0.06)	−0.52 (0.12)	−5.89 (0.04)	29.32 (0.04)
2.25	n4258+MW	Y	$z > 0.0233$	0.162 (0.013)	2.76 (0.13)	−15.645 (0.098)	−18.893 (0.093)	−3.31 (0.06)	−0.52 (0.12)	−5.89 (0.04)	29.32 (0.04)
2.25	n4258+MW	Y	Lower χ^2	0.159 (0.010)	3.06 (0.12)	−15.642 (0.095)	−18.893 (0.091)	−3.31 (0.06)	−0.52 (0.12)	−5.89 (0.04)	29.32 (0.04)
2.25	n4258+MW	Y	Stricter C	0.157 (0.011)	2.97 (0.15)	−15.654 (0.098)	−18.893 (0.094)	−3.31 (0.06)	−0.51 (0.12)	−5.89 (0.04)	29.32 (0.04)
2.25	n4258+MW	Y	Stricter σ_{X_1}	0.172 (0.010)	3.11 (0.11)	−15.646 (0.097)	−18.890 (0.092)	−3.31 (0.06)	−0.52 (0.12)	−5.89 (0.04)	29.32 (0.04)
2.25	n4258+MW	N	Default	0.165 (0.010)	3.08 (0.11)	−15.617 (0.093)	−18.858 (0.089)	−3.16 (0.05)	−0.40 (0.11)	−5.89 (0.04)	29.29 (0.04)
2.25	n4258+MW	N	Higher χ^2	0.167 (0.010)	3.13 (0.10)	−15.613 (0.093)	−18.859 (0.089)	−3.16 (0.05)	−0.41 (0.12)	−5.89 (0.04)	29.29 (0.04)
2.25	n4258+MW	N	$z > 0.0233$	0.162 (0.012)	2.75 (0.13)	−15.612 (0.094)	−18.861 (0.089)	−3.16 (0.05)	−0.41 (0.11)	−5.89 (0.04)	29.29 (0.04)
2.25	n4258+MW	N	Lower χ^2	0.158 (0.010)	3.05 (0.12)	−15.609 (0.095)	−18.861 (0.090)	−3.16 (0.05)	−0.40 (0.11)	−5.89 (0.04)	29.29 (0.04)
2.25	n4258+MW	N	Stricter C	0.156 (0.011)	2.96 (0.14)	−15.621 (0.095)	−18.859 (0.090)	−3.16 (0.05)	−0.41 (0.11)	−5.89 (0.04)	29.28 (0.04)
2.25	n4258+MW	N	Stricter σ_{X_1}	0.172 (0.010)	3.10 (0.11)	−15.610 (0.096)	−18.854 (0.091)	−3.16 (0.05)	−0.41 (0.11)	−5.89 (0.04)	29.28 (0.04)
R11	LMC+MW	Y	Default	0.165 (0.010)	3.09 (0.11)	−15.646 (0.102)	−18.887 (0.098)	−3.25 (0.05)	−0.11 (0.11)	−5.91 (0.06)	29.29 (0.07)
R11	LMC+MW	Y	Higher χ^2	0.167 (0.010)	3.14 (0.11)	−15.640 (0.101)	−18.886 (0.097)	−3.25 (0.05)	−0.11 (0.11)	−5.91 (0.06)	29.29 (0.07)
R11	LMC+MW	Y	$z > 0.0233$	0.162 (0.012)	2.76 (0.13)	−15.641 (0.102)	−18.890 (0.097)	−3.25 (0.05)	−0.11 (0.11)	−5.91 (0.06)	29.29 (0.07)
R11	LMC+MW	Y	Lower χ^2	0.158 (0.010)	3.06 (0.12)	−15.640 (0.102)	−18.891 (0.098)	−3.25 (0.05)	−0.11 (0.11)	−5.91 (0.06)	29.29 (0.07)
R11	LMC+MW	Y	Stricter C	0.156 (0.011)	2.97 (0.14)	−15.654 (0.101)	−18.893 (0.097)	−3.25 (0.05)	−0.11 (0.11)	−5.91 (0.06)	29.29 (0.07)
R11	LMC+MW	Y	Stricter σ_{X_1}	0.171 (0.011)	3.11 (0.11)	−15.644 (0.102)	−18.888 (0.098)	−3.25 (0.05)	−0.11 (0.11)	−5.91 (0.06)	29.29 (0.07)

Table D3 – *continued*

Cepheid rejection	Distance anchor	$P < 60$d	SN cut	α	β	$\mathcal{H}$	$M_{\rm B}$	$b_{\rm W}$	$Z_{\rm W}$	$M_{\rm W}$	μ_{4258}
2.25	LMC+MW	N	Default	0.164 (0.010)	3.09 (0.10)	−15.634 (0.098)	−18.875 (0.094)	−3.16 (0.04)	−0.07 (0.09)	−5.90 (0.05)	29.26 (0.06)
2.25	LMC+MW	N	Higher χ^2	0.166 (0.010)	3.14 (0.10)	−15.630 (0.099)	−18.874 (0.095)	−3.16 (0.04)	−0.07 (0.10)	−5.90 (0.05)	29.26 (0.06)
2.25	LMC+MW	N	$z > 0.0233$	0.161 (0.012)	2.76 (0.13)	−15.631 (0.098)	−18.879 (0.093)	−3.16 (0.04)	−0.07 (0.09)	−5.90 (0.05)	29.26 (0.06)
2.25	LMC+MW	N	Lower χ^2	0.158 (0.010)	3.06 (0.12)	−15.624 (0.101)	−18.875 (0.097)	−3.16 (0.04)	−0.07 (0.10)	−5.90 (0.06)	29.26 (0.07)
2.25	LMC+MW	N	Stricter C	0.155 (0.011)	2.98 (0.14)	−15.637 (0.099)	−18.875 (0.095)	−3.16 (0.04)	−0.07 (0.10)	−5.90 (0.06)	29.26 (0.07)
2.25	LMC+MW	N	Stricter $\sigma_{\rm X_1}$	0.170 (0.010)	3.11 (0.11)	−15.629 (0.100)	−18.873 (0.096)	−3.16 (0.04)	−0.07 (0.10)	−5.90 (0.06)	29.26 (0.07)
R11	LMC+MW	N	Default	0.165 (0.010)	3.08 (0.11)	−15.626 (0.102)	−18.867 (0.097)	−3.20 (0.04)	−0.02 (0.10)	−5.89 (0.06)	29.26 (0.07)
R11	LMC+MW	N	Higher χ^2	0.167 (0.010)	3.13 (0.10)	−15.620 (0.101)	−18.866 (0.097)	−3.20 (0.04)	−0.03 (0.10)	−5.89 (0.06)	29.26 (0.07)
R11	LMC+MW	N	$z > 0.0233$	0.162 (0.012)	2.76 (0.13)	−15.623 (0.102)	−18.872 (0.098)	−3.20 (0.04)	−0.03 (0.10)	−5.89 (0.06)	29.26 (0.07)
R11	LMC+MW	N	Lower χ^2	0.158 (0.010)	3.05 (0.12)	−15.618 (0.100)	−18.869 (0.095)	−3.20 (0.05)	−0.02 (0.10)	−5.89 (0.06)	29.26 (0.07)
R11	LMC+MW	N	Stricter C	0.156 (0.011)	2.97 (0.15)	−15.630 (0.103)	−18.869 (0.098)	−3.20 (0.04)	−0.03 (0.10)	−5.89 (0.06)	29.26 (0.07)
R11	LMC+MW	N	Stricter $\sigma_{\rm X_1}$	0.171 (0.010)	3.10 (0.11)	−15.621 (0.103)	−18.865 (0.098)	−3.20 (0.04)	−0.02 (0.10)	−5.89 (0.06)	29.26 (0.07)
2.25	n4258	Y	Default	0.165 (0.010)	3.08 (0.11)	−15.747 (0.109)	−18.989 (0.104)	−3.23 (0.07)	−0.55 (0.12)	−6.03 (0.07)	29.40 (0.06)
2.25	n4258	Y	Higher χ^2	0.167 (0.010)	3.13 (0.11)	−15.740 (0.108)	−18.985 (0.104)	−3.23 (0.07)	−0.55 (0.12)	−6.03 (0.07)	29.40 (0.06)
2.25	n4258	Y	$z > 0.0233$	0.162 (0.013)	2.76 (0.13)	−15.744 (0.107)	−18.993 (0.102)	−3.23 (0.07)	−0.55 (0.12)	−6.04 (0.07)	29.41 (0.06)
2.25	n4258	Y	Lower χ^2	0.158 (0.010)	3.05 (0.12)	−15.737 (0.110)	−18.989 (0.105)	−3.23 (0.07)	−0.55 (0.12)	−6.03 (0.07)	29.40 (0.06)
2.25	n4258	Y	Stricter C	0.157 (0.011)	2.97 (0.15)	−15.752 (0.109)	−18.990 (0.105)	−3.23 (0.07)	−0.55 (0.12)	−6.04 (0.07)	29.41 (0.06)
2.25	n4258	Y	Stricter $\sigma_{\rm X_1}$	0.172 (0.011)	3.10 (0.11)	−15.741 (0.108)	−18.985 (0.104)	−3.23 (0.07)	−0.55 (0.12)	−6.03 (0.07)	29.40 (0.06)
2.25	n4258	N	Default	0.165 (0.010)	3.08 (0.11)	−15.754 (0.107)	−18.995 (0.104)	−3.04 (0.05)	−0.44 (0.11)	−6.10 (0.07)	29.40 (0.06)
2.25	n4258	N	Higher χ^2	0.167 (0.010)	3.13 (0.11)	−15.747 (0.107)	−18.992 (0.103)	−3.04 (0.05)	−0.43 (0.11)	−6.10 (0.07)	29.40 (0.06)
2.25	n4258	N	$z > 0.0233$	0.162 (0.013)	2.75 (0.13)	−15.750 (0.106)	−18.999 (0.102)	−3.04 (0.05)	−0.44 (0.11)	−6.10 (0.07)	29.40 (0.06)
2.25	n4258	N	Lower χ^2	0.158 (0.010)	3.05 (0.12)	−15.747 (0.105)	−18.998 (0.102)	−3.04 (0.05)	−0.43 (0.11)	−6.10 (0.07)	29.41 (0.06)
2.25	n4258	N	Stricter C	0.156 (0.011)	2.96 (0.15)	−15.759 (0.107)	−18.998 (0.103)	−3.04 (0.05)	−0.44 (0.11)	−6.10 (0.07)	29.40 (0.06)
2.25	n4258	N	Stricter $\sigma_{\rm X_1}$	0.171 (0.010)	3.10 (0.11)	−15.748 (0.106)	−18.992 (0.102)	−3.04 (0.05)	−0.44 (0.11)	−6.10 (0.07)	29.40 (0.06)
2.5	n4258	N	Default	0.165 (0.010)	3.08 (0.11)	−15.775 (0.107)	−19.017 (0.103)	−3.06 (0.06)	−0.33 (0.13)	−6.12 (0.07)	29.41 (0.06)
2.5	n4258	N	Higher χ^2	0.166 (0.010)	3.13 (0.10)	−15.769 (0.108)	−19.015 (0.104)	−3.06 (0.06)	−0.34 (0.13)	−6.11 (0.07)	29.40 (0.06)
2.5	n4258	N	$z > 0.0233$	0.162 (0.012)	2.76 (0.13)	−15.768 (0.108)	−19.017 (0.104)	−3.06 (0.06)	−0.34 (0.13)	−6.11 (0.07)	29.40 (0.06)
2.5	n4258	N	Lower χ^2	0.158 (0.010)	3.05 (0.12)	−15.762 (0.108)	−19.013 (0.104)	−3.06 (0.06)	−0.33 (0.13)	−6.11 (0.07)	29.40 (0.06)
2.5	n4258	N	Stricter C	0.156 (0.011)	2.97 (0.15)	−15.779 (0.110)	−19.017 (0.106)	−3.06 (0.06)	−0.34 (0.13)	−6.11 (0.07)	29.40 (0.06)
2.5	n4258	N	Stricter $\sigma_{\rm X_1}$	0.172 (0.010)	3.10 (0.11)	−15.770 (0.107)	−19.014 (0.103)	−3.06 (0.06)	−0.34 (0.13)	−6.11 (0.07)	29.40 (0.06)
R11	n4258	N	Default	0.165 (0.010)	3.08 (0.11)	−15.728 (0.109)	−18.969 (0.105)	−3.09 (0.06)	−0.23 (0.13)	−6.08 (0.07)	29.40 (0.06)
R11	n4258	N	Higher χ^2	0.167 (0.010)	3.13 (0.10)	−15.725 (0.107)	−18.971 (0.103)	−3.09 (0.06)	−0.23 (0.13)	−6.08 (0.07)	29.40 (0.06)
R11	n4258	N	$z > 0.0233$	0.162 (0.013)	2.75 (0.13)	−15.723 (0.109)	−18.971 (0.104)	−3.09 (0.06)	−0.24 (0.13)	−6.08 (0.07)	29.40 (0.06)
R11	n4258	N	Lower χ^2	0.159 (0.010)	3.05 (0.12)	−15.718 (0.110)	−18.970 (0.106)	−3.09 (0.06)	−0.23 (0.13)	−6.07 (0.07)	29.40 (0.06)
R11	n4258	N	Stricter C	0.156 (0.011)	2.97 (0.14)	−15.733 (0.110)	−18.972 (0.106)	−3.09 (0.06)	−0.23 (0.13)	−6.08 (0.07)	29.40 (0.06)
R11	n4258	N	Stricter $\sigma_{\rm X_1}$	0.171 (0.011)	3.10 (0.11)	−15.723 (0.109)	−18.967 (0.105)	−3.09 (0.06)	−0.23 (0.13)	−6.08 (0.07)	29.41 (0.06)
2.25	LMC	Y	Default	0.165 (0.010)	3.08 (0.11)	−15.880 (0.104)	−19.122 (0.100)	−3.24 (0.05)	−0.55 (0.12)	−6.16 (0.07)	29.54 (0.07)
2.25	LMC	Y	Higher χ^2	0.167 (0.010)	3.13 (0.11)	−15.873 (0.102)	−19.119 (0.098)	−3.24 (0.05)	−0.55 (0.12)	−6.16 (0.07)	29.54 (0.07)
2.25	LMC	Y	$z > 0.0233$	0.162 (0.013)	2.76 (0.13)	−15.878 (0.104)	−19.127 (0.098)	−3.24 (0.05)	−0.56 (0.12)	−6.16 (0.07)	29.54 (0.07)
2.25	LMC	Y	Lower χ^2	0.159 (0.010)	3.05 (0.12)	−15.869 (0.105)	−19.121 (0.101)	−3.24 (0.05)	−0.55 (0.12)	−6.16 (0.07)	29.54 (0.07)
2.25	LMC	Y	Stricter C	0.157 (0.011)	2.97 (0.15)	−15.884 (0.103)	−19.123 (0.099)	−3.24 (0.05)	−0.55 (0.12)	−6.16 (0.07)	29.53 (0.07)
2.25	LMC	Y	Stricter $\sigma_{\rm X_1}$	0.172 (0.011)	3.10 (0.11)	−15.876 (0.103)	−19.119 (0.099)	−3.24 (0.05)	−0.55 (0.12)	−6.16 (0.07)	29.53 (0.07)
R11	MW	Y	Default	0.165 (0.010)	3.08 (0.11)	−15.515 (0.111)	−18.757 (0.106)	−3.21 (0.07)	−0.35 (0.14)	−5.83 (0.05)	29.19 (0.07)
R11	MW	Y	Higher χ^2	0.167 (0.010)	3.13 (0.11)	−15.513 (0.112)	−18.758 (0.108)	−3.21 (0.07)	−0.35 (0.14)	−5.83 (0.05)	29.19 (0.07)
R11	MW	Y	$z > 0.0233$	0.162 (0.013)	2.75 (0.14)	−15.511 (0.111)	−18.760 (0.106)	−3.20 (0.07)	−0.36 (0.14)	−5.83 (0.05)	29.19 (0.07)
R11	MW	Y	Lower χ^2	0.158 (0.010)	3.06 (0.12)	−15.508 (0.111)	−18.760 (0.107)	−3.21 (0.07)	−0.35 (0.14)	−5.83 (0.05)	29.19 (0.07)
R11	MW	Y	Stricter C	0.156 (0.011)	2.97 (0.15)	−15.521 (0.112)	−18.759 (0.107)	−3.21 (0.07)	−0.35 (0.14)	−5.83 (0.05)	29.19 (0.07)
R11	MW	Y	Stricter $\sigma_{\rm X_1}$	0.171 (0.011)	3.10 (0.11)	−15.513 (0.110)	−18.757 (0.106)	−3.21 (0.07)	−0.35 (0.14)	−5.83 (0.05)	29.19 (0.07)

This paper has been typeset from a TEX/LATEX file prepared by the author.